2017

Light Sheet Microscopy and Image Analysis of Neural Development and Programmed Cell Death in C. Elegans Embryos

Peter Insley

LIGHT SHEET MICROSCOPY AND IMAGE ANALYSIS OF NEURAL DEVELOPMENT AND PROGRAMMED CELL DEATH IN *C. ELEGANS* EMBRYOS

A Thesis Presented to the Faculty of

The Rockefeller University

in Partial Fulfillment of the Requirements for

the degree of Doctor of Philosophy

by

Peter Insley

June 2017

LIGHT SHEET MICROSCOPY AND IMAGE ANALYSIS OF NEURAL DEVELOPMENT AND PROGRAMMED CELL DEATH IN *C. ELEGANS* EMBRYOS

Peter J. Insley, Ph.D.
The Rockefeller University 2017

The positioning of neuronal cell bodies and neurites is critical for intact functioning of the nervous system. Mapping the positions of the soma and neurites in the brains of developing embryos as important central nervous system structures are being created may yield novel insight into the role of distinct cell groups in creating these structures.

New developments in microscopy have made this an excellent time to study neural development in the *C. elegans* embryo. In the past decade, implementations of highly light efficient methods such as single plane illumination microscopy have rendered it possible to follow development of embryonic structures in 3D with excellent temporal resolution (Huisken et al., 2004) and low phototoxicity. Recent work has resulted in quantitative characterization of the outgrowth of a single neurite in the late, rapidly moving three-fold stage of the *C. elegans* embryo for the first time (Christensen et al., 2015).

In this thesis, I first describe the construction and programming of a single plane illumination microscope (SPIM) based on a design from Hari Shroff's lab (Wu et al., 2011). The microscope is developed especially for use with *C. elegans* embryos and permits fast image acquisition without excessive photodamage, compared to other forms of microscopy.

Second, I describe the use of the SPIM microscope to image the development of a subset of sublateral neurons, the earliest known entrants to the nerve ring (Rapti et al, in preparation), into which they grow in the 1.5-fold stage. I describe an algorithm for automatically aligning developing embryos onto one another until the beginning of the rapid embryonic movements known as twitching, which begin at the start of the twofold stage. I employ my algorithm to align a group of identically imaged embryos onto one another and deduce information about the positioning of the nerve ring in an approximately uniform coordinate system. I determine that nerve rings are precisely positioned in the embryo to within about a micrometer while the cell bodies that grow into the nerve ring are positioned over a much wider distance. My work suggests that the nerve ring grows out towards the ALA neuron as an anchor, and that twitching may begin when the developing nerve ring reaches the ALA. I additionally describe observation of new phenotypes related to the *cam-1* mutation, which was previously identified as a regulator of anterior-posterior placement of the nerve ring (Kennerdell et al., 2009).

Third, I describe an application of the SPIM microscope for imaging the death of the tail spike cell, a complex, multi-compartment differentiated cell which dies over a period of hours during the three-fold stage, when the animal is rapidly moving in its shell, and cannot be imaged otherwise than with a rapid, light efficient microscope such as the one described here. I determined the time course and confirmed the sequence of events of wild type tail spike cell death. Additionally, I report stronger phenotypes for some known tail spike cell death genes when imaged in the embryo, suggesting that *eff-1* plays a stronger role than previously known in clearance of the distal part of the tail spike cell

process, and additionally that *ced-5* has a strong role in clearance of the same compartment (in addition to its known role in soma clearance).

In an appendix I describe work beginning on an extension of the microscope, which will hopefully see the microscope used as a tool for selectively inducing fluorescence in individual cells and following the development of those cells in time.

My results demonstrate the utility of single plane illumination microscopy for study of *C. elegans* embryogenesis and establish fundamental facts about the variability of the *C. elegans* central nervous system by making direct comparisons between animals. This work contributes to our understanding of the *C. elegans* nervous system by establishing fundamental bounds on the range of nerve ring positioning between individuals.

ACKNOWLEDGMENTS

First, I want to thank my advisor Shai Shaham for his continued support, for innumerable helpful conversations, and for his thoughtful guidance during my graduate studies. I especially thank him for suggesting that I build the SPIM microscope, which has born such interesting fruit. I thank my thesis committee members, Sanford Simon, Gaby Maimon, and Zhirong Bao, for helpful conversations and guidance, as well as Eric Siggia who served on my committee before my work diverged too much from his area of expertise. Eric very strongly influenced how I think about science, particularly biophysics, and I am grateful to him for that. I also want to thank Hari Shroff and Yicong Wu for their kind assistance at the start of the SPIM project.

Within my Rockefeller lab many people have helped me out. I am especially grateful to Piya Ghose, with whom I collaborated directly on the tail spike cell work and without whose endless dedication and thoughtful work the tail spike cell project would not exist. I also thank Georgia Rapti, who has been extremely helpful with reagents and generous with discussions about the nerve ring, and Anu Singhal with whom I often worked directly. I always looked forward to those days and I expect we'll get back to it soon. I thank Aakanksha Singhvi and Menachem Katz for the biological advice that I received from them and for the constant help they've provided over these years, as well as all the other members of the lab. I also want to thank Margherita Peliti, a former member of our lab, for her friendship and support during my graduate school years and afterwards.

Elsewhere at Rockefeller, I want to thank Zak Frentz in the Leibler lab and Alex Katsov in the Bargmann lab for helpful discussions on SPIM microscopy. Both were very generous with their time and advice.

I want to thank my family for their tireless love and support. I couldn't do it without you.

Finally, thank you to my girlfriend, Heather, for many interesting conversations past and future, some of which gave me ideas for my work, and for her unbelievable patience and love over the last year of thesising and pre-thesising.

Table of Contents

List of Figures

List of Tables

Chapter 1: Introduction

Summary

To study development in ever increasing detail, microscopes of increasing sophistication will be required. In my graduate work I built a single plane illumination microscope which I used to study aspects of *C. elegans* development, specifically the development of the nerve ring (Chapter 3), and the programmed cell death of the tail spike cell (Chapter 4). In this introduction I present background material on the recent developments in light microscopy which have led to the rise of single plane illumination microscopy, as well as examples of the use of single plane illumination microscopy in developmental biology. Secondly, I describe various cell lineaging efforts in *C. elegans* which have many parallels with my own work, including the use of some of the same software in both cases. As part of my thesis work, I developed an algorithm for aligning developing *C. elegans* embryos in space and time; so, third, I discuss general aspects of image registration, as well as specific results in point set registration which relate to the thesis. Finally, I describe existing data available on the development of the nerve ring. Background material for the tail spike cell and cell death is contained in Chapter 4.

Fluorescence microscopy primer

A typical widefield fluorescent microscope consists of an objective / tube lens pair (Figure 1.1), which reimages planes of the sample onto a sensor (i.e. a camera, or a human eye). Tracking the microscope objective in Z results in a Z shift of the sample plane which is in focus at the sensor; these planes, the plane of the sample (also known as the object plane), and the image plane onto which it is reproduced, are referred to as conjugate planes. A single sample plane is also referred to as a slice. Light is provided to the sample usually from a white light bulb which is filtered to provide specific colors; these colors are matched by the filter to the specific excitation spectrum of the fluorophore that is being used. Light is not specifically shone on any sample plane, instead running all the way through the sample while only a single plane is imaged; the resulting phototoxicity (Hoebe et al., 2007; Tinevez et al., 2012) can rapidly lead to the degradation and death of biological samples.

Figure 1.1: Widefield fluorescence microscope diagram

The setup of a typical widefield fluorescence microscope is described.

A: A white light source sends light out at a wide range of angles, from a wide range of positions (shown here as a discrete set of rays for simplicity). The light is filtered for a specific color, here cyan (for use with GFP), by an excitation filter. The light passes through a microscope objective on its way to a sample. The light is not focused to a point at the sample because it comes into the objective at a range of angles and positions, such that it remains spread out after passage through the objective. The sample emits fluorescent light (green) which is collected by a microscope objective and reimaged by a tube lens. The ratio of focal lengths of these two lenses determines the magnification of the system. **B:** In order to acquire different slices, the microscope lens itself typically moves, changing the plane of focus of the system. The sample is illuminated all the way through to acquire one plane's worth of information.

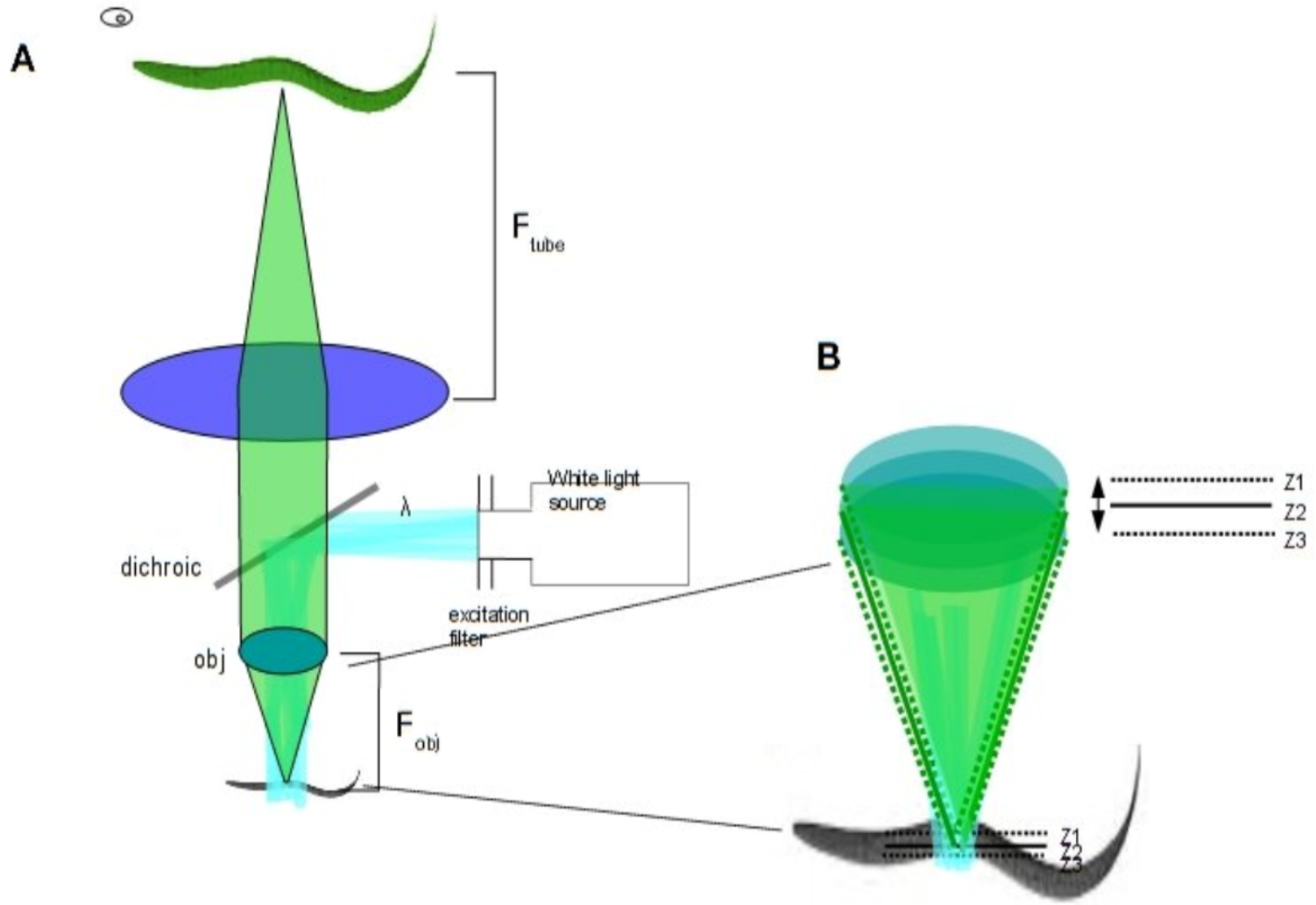
A
B
F tube
White light source
λ
dichroic
excitation filter
obj
F obj
Z1
Z2
Z3
Z1
Z2
Z3

The operation of a typical microscope is defined by a point spread function (PSF), which describes the range in space over which a point source in a sample can be localized after imaging. (The same term and function is often used to describe imaging or focusing under a single lens, for example, under a microscope main objective lens.) The PSF is a function F(x,y,z; x',y',z') which describes the three dimensional image made by the microscope of a sample point x,y,z in the imaging region of the microscope, a space defined by coordinates x',y',z'. For the given sample point, the PSF of a microscope will describe a brightest point in the imaging coordinate system (the focus) as well as the spread of light into other planes and points of the imaging plane. The full image of a sample under the microscope can be thought of as the weighted integral over all fluorescent point sources. In practice, fluorophores such as GFP function as point sources; the total intensity in the image space, then, recorded perhaps as electronic counts on a camera sensor, is proportional to the density of fluorophores in the sample. The image intensity will also be approximately proportional to the intensity of excitation light for small intensities, as well as being proportional to imaging duration under the same assumption.

The important Abbe diffraction limit is a theoretical limit on microscope resolution derived from analyzing the PSFs of point source samples imaged by lenses (Born and Wolf, 1999; Abbe, 1882). It arises because of the inability of a microscope to collect all light coming from a sample, which limits the information available to reconstruct the sample exactly. Diffraction limit resolution criteria (such as Rayleigh,

Sparrow) state that imaging resolution in the plane of the sample is approximately limited to λ/2NA, where λ is the wavelength of fluorescent emitted light and NA is the numerical aperture, a measure of the range of opening angles captured by a microscope objective; imaging resolution in the Z axis is approximately given by λ*n/NA^2. Numerical aperture is given as n*sin(theta), where n is the index of refraction of the sample medium. **(**When collimated light shines through an objective, the numerical aperture is also used to describe the size of the focused beam after imaging.) The best imaging resolution achievable with a high end widefield microscope is about 200nm laterally and about 500nm axially.

Although the Abbe limit was interpreted for much of the twentieth century to be a hard limit on imaging resolution, by the latter decades of the century it was beginning to be realized that the limit only held true under a carefully tailored set of circumstances and could be overcome using a variety of methods.

Indeed, the past few decades have seen a revolution in fluorescence microscopy, with renewed interest in basic research and a recent Nobel Prize in Chemistry devoted to the subject. This revolution has transpired on several fronts, of which I want to emphasize two here: the first is a set of novel technologies providing fluorescent imaging resolution far beyond the diffraction limit; while the second is an improvement in the light efficiency of microscopes far beyond that possible in traditional widefield fluorescence microscopy and its comparatively simple extensions, in which the whole sample is illuminated to image just one plane (Webb and Brown, 2013; Swedlow and

Platani, 2002). As it turns out, the history of the two avenues of investigation described above is intimately linked.

I will describe in the next section the variety of diffraction limit breaking methods which function by spatially patterning the excitation light sent to the sample / emission light collected from the sample; the multiple objective configurations that grew out of these methods; and the link between these methods and the development of single plane illumination microscopy. Other resolution enhancement methods – such as the fluorophore counting, centroid averaging methods of STORM and PALM microscopy (Rust et al., 2006; Betzig et al., 2006); near-field approaches such as Near Field Scanning Optical Microscopy (Betzig et al, 1986) and Total Internal Reflection Fluorescence Microscopy (Axelrod, 1981); Maxwell fisheye-based imaging (Leonhardt, 2009); and even more exotic methods such as negative index of refraction metamaterial lens microscopy (Zhang and Liu, 2008), while highly interesting in their own right, have no real bearing on single plane illumination microscopy, and none of these will be mentioned here again except STORM and PALM, by way of comparison. STED microscopy (Hell and Wichmann, 1994); (Klar et al., 2000), while it operates using a form of excitation patterning, and so in a way relates to SPIM, must be nearly useless for embryological imaging because of the enormously high excitation intensities it requires, and it also won't be discussed further here. Although multiphoton microscopy improves resolution at depth and is in theory a diffraction-limit surpassing technique for a fixed wavelength -- two IR photons used in a two-photon approach will improve resolution

over a single IR photon used in a single photon approach -- the longer wavelengths of light required for multiphoton imaging mean that it worsens resolution for thin samples (Gustafsson, 1999) when compared with normal fluorescent imaging. Multiphoton microscopy will be mentioned in passing in the section on Bessel beam imaging.

Resolution past the diffraction limit: confocal microscopy

The confocal microscope (Figure 1.2) is to my knowledge the first successful effort to push spatial resolution beyond the Abbe limit (Abbe, 1882), as well as the first such effort to use patterned excitation light. The principle behind confocal microscopy was propounded and patented by the artificial intelligence researcher Marvin Minsky in the late 1950's (Minsky, 1961); (Minsky, 1988), although microscopes based on his design only started becoming available a decade or two later ((Davidovits, 1969); (Davidovits and Egger, 1971). In its basic form, a confocal microscope operates by focusing an excitation laser onto a sample at a defined X, Y, Z position through a standard high NA microscope objective. Unlike in widefield microscopy, where no great effort is made to control the shape of the excitation light at the sample, here the spread of excitation light at the focus is diffraction-limited by the objective's numerical aperture. This diffraction-limited excitation spot is then scanned across the X-Y plane of the sample, with the resulting fluorescence truncated by a pinhole conjugate to the sample plane and counted in a photo-multiplier tube. Various slice depths are acquired as in a

widefield configuration by simply moving the microscope objective in Z, which changes the Z position of the object plane while leaving the imaging plane fixed.

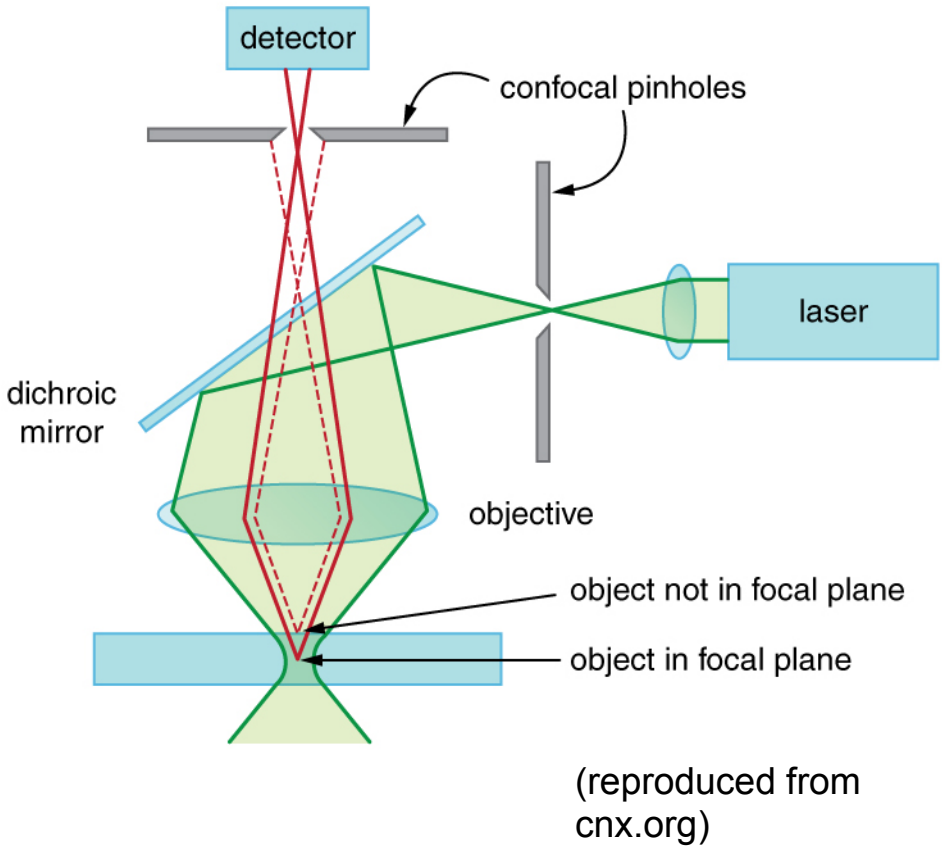

Figure 1.2: Laser-scanning confocal microscope diagram

In a laser-scanning confocal microscope, a laser is used to excite points in a sample in sequence. Light from each point illuminated by the laser is sent to a pinhole which partially blocks out of focus light, thus sectioning the sample. Confocal microscopes also can improve resolution laterally and axially, if one severely tightens the pinhole to block light coming from outside the center of the laser spot.

The use of a focused laser reduces the magnitude of out of focus excitation at a given sample point over widefield in a nonlinear way, according to the PSF of the excitation objective and the profile of the incoming laser. A typical Gaussian beam (Alda, n.d.; Hecht, 2016) will exhibit Gaussian intensity decay in the X-Y plane of the focus and quadratic decay in Z, past a distance called the Rayleigh length, over the extent of which the focus is relatively uniform in Z. The Rayleigh length is proportional to the square of the beam width at the focus; on either side of the length the laser diverges in a linear way according to the angle of the excitation focus. The pinhole blocks most of the out of focus light above and below the sample plane; out of focus planes produce a bigger disc at the plane containing the pinhole than the in focus range. The result is that the pinhole blocks a (quadratically) higher percentage of out of focus excitation coming from above and below the sample plane, thus "sectioning" the image. Resolution can be improved over widefield in a confocal microscope by shrinking the size of the pinhole so that it permits only very little light from outside the focus of the laser; the side effect of this is that very little light is collected at all. The best resolution achievable from a confocal is a$\sqrt{2}$ improvement both axially and laterally over widefield, perhaps 150nm laterally and 350nm axially, although this resolution is rarely achieved in practice because the loss of light required is so severe (Alison North, personal communication).

Extensions of confocal microscopy

The most common extension of the basic laser scanning confocal microscope is the spinning disk confocal microscope (Toomre and Pawley, 2006). Spinning disk confocal microscopy (SDCM) has seen and continues to see heavy use, including in developmental biology, and especially in situations where a low excitation light intensity is critical for sample viability, and where a high speed of imaging is required for capturing developmental changes. SDCM operates by multiplexing a number of lasers (i.e., by splitting a single laser with a microlens array) and confocal pinholes on a spinning disc. Fluorescence is thus excited by multiple lasers exciting multiple spots on the sample. Emissions are truncated by the spinning perforations, which are kept well-separated so that the whole system acts like multiple laser-scanning confocal microscopes at once. Instead of perhaps a second for an old laser-scanning confocal to capture a frame (although much faster models have more recently come into existence), with the speed declining with the linear dimension to be scanned, a spinning disk (rotating at a rate of perhaps 5000-10,000 RPM) can capture an entire slice in milliseconds independent of the size of the area to be captured. SDCM imaging is far gentler than laser-scanning confocal microscopy, perhaps because peak laser intensity per sample voxel is dramatically reduced, permitting longer acquisition time per sample position (e.g. Gao et al., 2012). The spinning disk confocal microscope remains a common microscope of choice for imaging light sensitive samples at fairly high imaging rates, although it is

rapidly being rendered obsolete by single plane illumination microscopy (discussed below).

Another variant on confocal microscopy is the "4-pi confocal microscope" developed by Stefan Hell, Ernst Stelzer and collaborators (Hell and Stelzer, 1992); (Hell et al., 1994). 4-pi microscopes work by opposing two high numerical aperture objectives on opposite sides of a sample to collect the full 4 pi solid angle worth of emitted light, and thus the full range of (non-evanescent) frequencies (Axelrod, 2013). The imaging pathway additionally uses a pinhole to cut out of focus light from both paths. The "type B" implementation works by opposing high numerical aperture lenses on opposite sides of a sample to collect the total 4-pi solid angle worth of emission. Light from top and bottom objectives are subsequently recombined at the detector, with optical path lengths kept as close as possible to identical for the two imaging trajectories. This results in coherent superposition of emitted light at the detector, with sharpening of the central peak. This can be used to provide a near-isotropic point spread function improving resolution in the Z-axis by a factor of 3-4, with a later implementation ("type C") operating by adding a superposition of coherent excitation light, with optionally a two photon approach to damp sidelobes in the PSF; type C can improve axial resolution by 7 times. 4-pi confocal microscopy is closely related to the set of techniques known as InM (Gustafsson et al., 1999), developed by Mats Gustafsson and collaborators.

The final implementation of confocal microscopy to be discussed here is the "confocal theta microscope," also developed in the Stelzer group (Lindek and Stelzer,

1994). While to my knowledge the theta microscope was rarely used, it is important historically because the objective geometry used is identical to that employed in single plane illumination microscopy and it is a clear predecessor to SPIM, developed by some of the same people. The theta microscope operates by impacting two objectives on the sample, mounted at 90 degrees to one another. The full aperture of the first objective is used to generate a light spot which is then imaged using the second objective. Emission light collected with the second objective is truncated with a pinhole as in a normal laser-scanning confocal microscope. Because of the tilted geometry, the Z direction of the detection objective is now in the X-Y plane of the laser focus, meaning effectively that the low-resolution direction of the second objective corresponds to the high resolution direction of the laser focus. The excitation and emission PSFs taper rapidly to zero in orthogonal directions; this has the result that the total PSF of a confocal theta microscope is substantially smaller than in a typical confocal microscope of the same detection NA, with a stated improvement of 3.5 axially. However, this is not the correct comparison to make; in practice the axial resolution gains tend to be minor, because of the requirements of lower numerical aperture objectives forced by the need to accommodate two objectives at 90 degrees (Gustafsson, 1999). Lateral resolution is decreased by around 50%. The "theta" of the microscope name refers to the progressively improved axial resolution as the second objective tilts towards 90 degrees away from the excitation objective.

Structured illumination microscopy

An alternative approach to resolution enhancement called structured illumination microscopy (SIM) was developed separately from Hell and Stelzer and collaborators, by Gustafsson and collaborators (Gustafsson, 2000). SIM operates by encoding high frequency information (using a narrow-spaced grating) into the excitation light, which is subsequently processed out by adding several such images out of phase. The highest frequencies (corresponding to large "angle" or "aperture") in the resulting, processed emission light are doubled, producing a factor of two resolution enhancement over widefield in X, Y, and/or Z, with 15 exposures required per slice for 3D resolution doubling (Shao et al., 2011). This style of imaging is extremely useful because it is relatively cheap to implement and does not require specialized fluorophores, and relatively simple hardware is required to implement it. A more recently developed version of this imaging approach called nonlinear structured illumination microscopy (Gustafsson, 2005); (Rego et al., 2012) takes advantage of a nonlinearity in response of fluorophores to excitation light in order to encode higher frequency of information and in theory can produce an arbitrary resolution improvement, at the expense of either greatly increased intensity of exposure or a new requirement for specialized photo-convertible fluorophores, as in STORM, PALM, and STED. Nonlinear SIM has achieved 50nm lateral resolution (Rego et al., 2012). An "instant" version of SIM, in which the processing of the image series is conducted optically rather than computationally, has become available (York et al., 2013).

Fast imaging: single plane illumination microscopy

Paralleling the development of higher resolution microscopes has been the development of more light efficient, faster microscopes. These terms are frequently synonymous, with, in my experience, the limiting factor governing the speed of imaging usually being phototoxicity rather than any mechanical limitation. The single plane illumination microscope (SPIM) (Figure 1.3) and its close relatives are currently the most useful kind of high light efficiency microscope. Other techniques for improving light efficiency over widefield exist, for example the light field microscope (Levoy et al., 2006); the light field microscope is in some sense a maximally light efficient microscope, using nearly all collected light from a sample to generate multiple synthetic views and / or slices. However, the extreme loss of resolution inherent in light field microscopy relative to widefield microscopy, even under elaborate deconvolution and processing (Broxton et al., 2013); (Prevedel et al., 2014), will probably slow its adoption.

Figure 1.3: Single plane illumination microscope diagram

A single plane illumination microscope in its simplest form is a widefield microscope (det obj, or detection objective, and associated optics) with the excitation function given over to another lens situated at 90 degrees (ex obj, or excitation objective). The excitation objective is set up to produce a focal spot with a long Rayleigh length (an elongated tube, cyan); scanning the beam perpendicularly to the beam axis and to the detection objective will make a sheet, while scanning in both directions will make a volume. The detection objective images just the plane of the sheet, thus dramatically increasing light efficiency over a regular widefield microscope.

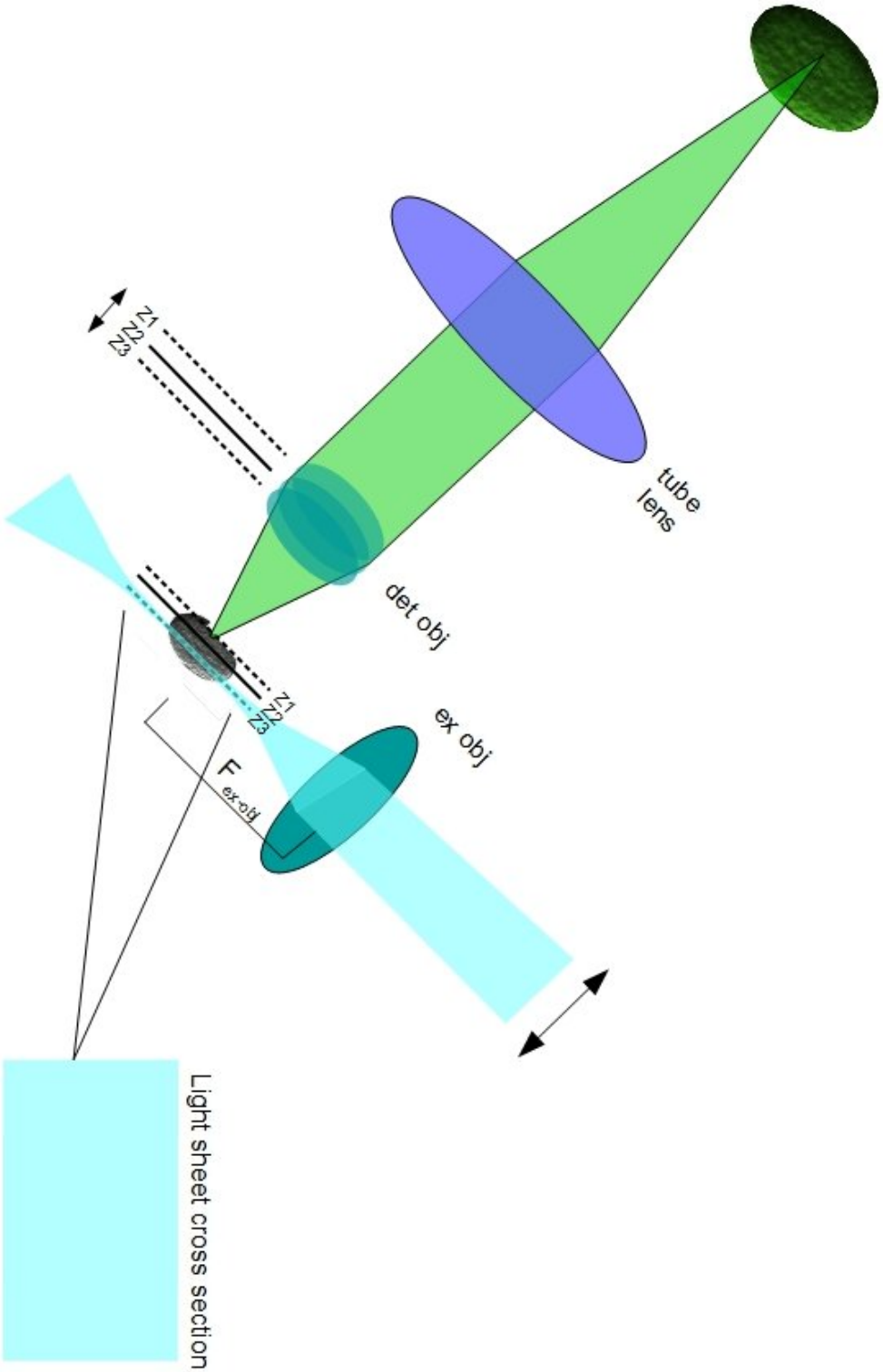
z1
z2
z3
tube
lens
det obj
z1
z2
z3
ex obj
F ex-obj
Light sheet cross section

Ernst Stelzer and collaborators developed the first modern SPIM microscope (Huisken et al., 2004), shortly after developing the confocal theta microscope (although related light sheet microscopes used for imaging small particles have existed since 1902 (Siedentopf and Zsigmondy, 1902, reviewed in Huisken and Stainier, 2009)). Like the (optimally configured) theta microscope, the single plane illumination microscope has a second excitation objective situated at 90 degrees to the emission or detection objective. Unlike the theta microscope, the single plane illumination microscope uses a low numerical aperture on the excitation side in order to produce a drawn out laser, wide at the point of focus, but of substantial Rayleigh length. At the focus, a SPIM laser might be micrometers in width (as opposed to the several hundred nanometers expected from a laser focused through a high NA objective); a thinner beam would be better, but the width of the beam is determined by the requirement that twice the Rayleigh length be at least as long as the axis which the sample presents to the laser, with the Rayleigh length going as the beam width squared as described above. The Rayleigh length is chosen in this way so that the laser will not diverge appreciably over the sample, providing an approximately uniform illumination in the beam direction. The beam is either swept (one or more times) across the sample using a galvanometer (a device which converts applied voltage to angle),or a cylindrical lens is used to flatten and broaden the original axially symmetric beam. Either of these methods generates a "light sheet" for the extent of the beam waist, which can be used to illuminate a "single plane" of the sample; SPIM is also known as

Light Sheet Fluorescence Microscopy or LSFM. One camera acquisition (in a basic setup) is acquired per plane / light sheet. This has the result that a much higher percentage of excitation light is translated to in-focus emission than in widefield or confocal microscopies, in both of which the entire sample is illuminated to collect only one plane's worth of in-focus emitted light.

Although SPIM and confocal theta microscopy are closely related, as described above, the effect and purpose of the imaging in SPIM and confocal theta microscopies is completely different. In confocal theta microscopy, one point is acquired at a time, with the sole aim of improving axial resolution, slowly building up a high quality map of a sample; in SPIM, a whole sheet is quickly acquired at one time with the aim of improving light efficiency. The SPIM microscope has a lower resolution than widefield both laterally and axially, requiring the same sacrifice of numerical aperture on the emission side as the theta confocal but without the high NA focus on the excitation side and the pinhole to improve axial resolution. While SPIM, like a confocal, does inherently produce optical sectioning -- a result of the illumination being restricted to a single plane and tapering off like a Gaussian outside that plane -- for samples the size of *C. elegans* embryos or larger (*C. elegans* embryos are approximately 25 x 25 x 50 micrometers), the requirement of keeping twice the Rayleigh length to greater than the width of the embryo results in a beam wider than the depth of field the detection objective PSF, or equivalently, in a total PSF for which the axial component of resolution is dominated by the detection objective.

While the first implementation of SPIM used an upright agarose cylinder to contain the sample, SPIM can also be implemented on a typical inverted microscope setup. Wu et al (2011) built a single plane illumination microscope in this more traditional geometry by introducing a pair of objectives at 90 degrees onto the top of an inverted microscope setup, with the SPIM objectives being placed in the position where the microscope condenser would typically go. As the microscope I constructed is closely based on this design, and indeed uses many of the same components, I will discuss additional aspects of this microscope in the following chapter (Chapter 2) when I discuss construction of my own SPIM microscope.

A SPIM microscope will often use water objectives with long working distances; in a SPIM rig it is difficult to accommodate an objective of higher than numerical aperture 1.0 (Gary Rondeau, ASI, personal communication), the use of which would then force one to use a very low numerical aperture objective (perhaps .3 NA) for the excitation side. If one makes the requirement that the excitation and detection objectives have the same numerical aperture (necessary for generating an isotropic point spread function in certain related implementations, e.g. (Planchon et al. 2011)), then working under the geometrical constraints brought on by the objective design, it is hard to do better currently than to use twin .8 NA objectives. Use of a .8 NA imaging objective results in lateral resolutions that are approximately a factor of two worse than in high-end widefield systems, and an axial resolution about 3 times worse. The axial resolution

may be as much as four times worse in SPIM than in high NA point scanning confocal microscopes using small apertures (e.g. Stemmer et al. 2008; Schrader et al. 1996).

Extensions of single plane illumination microscopy

Various improvements on the most basic implementation of SPIM have been proposed and implemented, starting even in the initial paper presented by the Stelzer group.

One of the most common extensions of single plane illumination microscopy is the acquisition of images from multiple perspectives, for subsequent registration. In the first biological paper using the first light sheet microscope (Huisken et al., 2004), axial resolution was improved over "traditional" SPIM by acquiring four views, accomplishedby rotating the agarose cylinder containing the sample and imaging from a fixed geometry; the views were fused by looking for peaks in the cross-correlation function (Brown, 1992), and then acquiring maxima in frequency space across all four views in a kind of frequency space maximum projection. This effectively takes the best view for each frequency component, meaning there is no "bad" (i.e. axial) direction, with this procedure having the unfortunate side effect of throwing away much of the information acquired in the imaging.

Wu et al (2013) built a two-view system using the basic SPIM setup of two objectives at 90 degrees, but with sequential excitation and detection from the two axes. Using a sequential deconvolution algorithm, in which the results of each stage of a Lucy

Richardson deconvolution (Richardson, 1972) from one objective were fed as the Bayesian prior "guess" to the other objective's Lucy-Richardson problem – the researchers report dramatically improved lateral and axial resolution down to ~300nm isotropic resolution with only a two-fold increase in excitation intensity.

Keller et al (2010) combined SPIM and structured illumination approaches to produce improved resolution at depth over baseline SPIM, essentially using the sectioning mode of structured illumination (Juskaitis et al., 1996). This is of biggest utility in thick samples like zebrafish embryos, but could still be useful in our system of *C. elegans* embryos. Researchers working in Eric Betzig's lab Planchon et al (2011) and Gao et al (2013) have used Bessel beams to replace the Gaussian beams in traditional SPIM, reporting improved lateral and greatly improved axial resolution, achieving isotropic 300nm resolution. Bessel beams are a surprising, focused non-diffractive type of beam which continually replenish their central peak from surrounding side lobes (Durnin et al., 1987; Durnin, 1987), in theory infinitely, but in practice with an extent varying with several factors, being among other things proportional to the lateral size of the lens aperture used in making the beam. The SPIM-Bessel combination employed a pair of clever tricks for minimizing the emissions from the side lobe excitation, in particular, the simultaneous use of a structured illumination approach can be used to decrease their amplitude. Another approach employed by the Betzig group to minimize the side lobes was the use of two-photon microscopy, which requires a combination of two photons at twice the normal excitation wavelength to produce one normal

wavelength quantum fluorescent transition, a method which therefore has a cross-section (efficiency of excitation) which goes as the square of the incident intensity and can dampen the smaller side lobes. Two photon SPIM microscopy with Gaussian beams has also been implemented (Lavagnino et al., 2013) to improve resolution at depth in thick samples. The Bessel-SPIMmicroscope has been improved by replacing the single beam with a multiple beam setup, thus permitting reduced peak intensities because of increased dwell time of the beams at each position (Chen et al., 2014).

Groups have reported implementing line-scan confocal microscopy in a SPIM setup (Silvestri et al., 2012), which is an intermediate form of confocal microscopy in which an entire line is illuminated at once, and a stripe is used instead of a pinhole. The idea here is to use the line by line readout of a CMOS camera (Fossum, 1997) as the striped-pinhole which tracks the sweep of the laser beam. Silvestri et al describe the use of this technique as a contrast enhancement tool rather than as a means of enhancing resolution, although presumably the tool could be employed to improve resolution in the line-scan direction and perhaps axially as well.

SPIM use in developmental biology

The first SPIM microscope developed in the Stelzer lab (Huisken et al, 2004) used a multiview setup to image all the muscles of the medaka fish *Oryzias latipes* as well as producing a time series of a cell-membrane-labeled *Drosophila melanogaster* embryo. Huisken et al used a very low numerical aperture objective (.25 NA), presumably to

accommodate the largish size of the embryos they imaged, with the result of a rather low reported resolution (1.1 um isotropic). Their imaging at ten frames per second was sufficiently rapid as to observe the heart beat of the Medaka fish for the first time at its natural rate.

Keller et al (2008), also working in Stelzer's group, used a methodology similar to that of the 2004 paper, but employed a swept beam to generate the light sheet, generating massive, high time-resolution recordings of all nuclei in the early zebrafish embryo. They derived information about gross morphogenetic movements in the zebrafish, in particular noticing a "radial symmetry breaking" round of cell divisions which presumably could not have been observed with a less global imaging technique, also identifying those cells of the early embryo which ultimately gave rise to the mesendoderm.

Continuing Keller's previous work, (Tomer et al., 2012) produced a static implementation of multiview SPIM with four optical arms, with the composite imaging permitting clean whole *Drosophila* embryo imaging without the need for multiphoton microscopy to reduce scattering at depth (for use of two-photon imaging in Drosophila embryos see e.g. (Gregor et al., 2007)). This multiview system was used to study nuclear movements and divisions in the late mitotic cycles of the drosophila syncytial blastoderm, with information about nuclear speed and division distance derived. A similar SPIM system was subsequently used to record calcium expression data from the entire drosophila nervous system (Lemon et al, 2015), permitting analysis of expression

in particular regions of the nervous system during whole brain activity associated with forward and backward movement.

Additionally, several studies have been conducted in the Shroff lab using single plane illumination microscopy to describe aspects of *C. elegans* development, especially neural development. Wu et al (2011) characterized the migrations and neurite outgrowth of the canal-associated neurons CAN-L and CAN-R, using the high speed of SPIM imaging to follow their development past twitching. The outgrowth of the neurites of the ALA neuron was also observed, which begins around the time of twitching. Wu et al (2013) followed development of the AIY interneurons past twitching, quantifying rate of axon outgrowth with sufficient resolution as to distinguish between retrograde and anterograde extension (Heiman and Shaham, 2009). Christensen et al (2015) followed outgrowth of several neurons including the ALA through the end of development, using a novel image registration pipeline to untwist two- and three-fold animals (see below) and compare neurite development across animals, permitting quantitative analysis of neurite development in the three-fold animal.

C. elegans: Overview and life cycle

All of the biological work which I present in this thesis was conducted in *Caenorhabditis elegans* embryos. Here, I provide a brief overview of the life cycle and development, especially the embryonic development, of the animal.

C. elegans is a soil nematode which was introduced as a model system in the 1970's (Brenner, 1974) because of its many useful characteristics. Among other excellent qualities: first, *C. elegans*' invariant lineage renders repeat experiments possible on individual cells; second, the animal is roughly transparent, so that microscopy experiments are comparatively easy to perform on these worms relative to thicker, more heavily scattering systems such as *Drosophila* embryos; third, the *C. elegans* life cycle is extremely rapid, with a single hermaphroditic worm generating approximately 200 more hermaphrodites in 5 days. While in the wild, males are rare, in the laboratory they can be generated and mated to hermaphrodites, thus providing the means of crossing genetic strains.

The *C. elegans* lifecycle consists of an approximately 14 hour embryogenesis (at 20 degrees Celsius), running from fertilization to hatching, followed by passage through 4 larval stages (L1, L2, L3, L4), defined primarily by increasing size, nervous system complexity and gonadal maturity, before adulthood is reached. The worm increases in volume by around 1000 times between the end of embryogenesis and adulthood, while not quite doubling its number of cells, with the volume increase primarily owing to increased size of its cells.

In contrast to the larval and adult volume increase, the initial stages of *C. elegans* embryogenesis proceed in a series of roughly synchronous rounds of cell divisions across the embryo without very much growth in total cellular volume, beginning with 1 cell and ending with 558 cells within the same eggshell. In fact, 671 cells are born over the

course of embryogenesis; the discrepancy between cells born and cells present is explained by the wide use of programmed apoptotic cell death in the embryo to kill and clear unneeded cells (Sulston et al., 1983; Horvitz, 1999). Individual "founder blastomeres" E, MS, AB, C, D, and P4 (Figure 1.4) give rise to lineages with roughly synchronized division times, with all founder cells giving rise to diverse tissue types except for P4 (germline) and E (intestine). Early identities are established by a mix of asymmetric cell division inheritance and cell-cell signaling (Gönczy and Rose, 2005); (Owraghi et al., 2010). Later the descendants of early blastomeres migrate substantial distances (Schnabel et al., 1997) to locations specified by their lineage inheritance; homeotic transformations may cause cells to migrate to incorrect locations. Cell fate and movement can be influenced by the location of diffused morphogens (Harterink et al., 2011), such as the Wnt proteins CWN-1, CWN-2 (Pan et al, 2006).

Figure 1.4: Stages of *C. elegans* embryogenesis

Embryos develop from a 1 cell organism encased in an eggshell to a freely moving larval worm in approximately 14 hours at 20 degrees. The ball stage (marked here) is reached at approximately 300 cells; also of note is the development of the tail during "elongation" in the comma, 1.5-fold, and two-fold stages; as well as the onset of twitching at the end of the 1.5-fold stage; and the three-fold stage in which the animal moves in arbitrary directions within its eggshell. Adapted from WormAtlas.

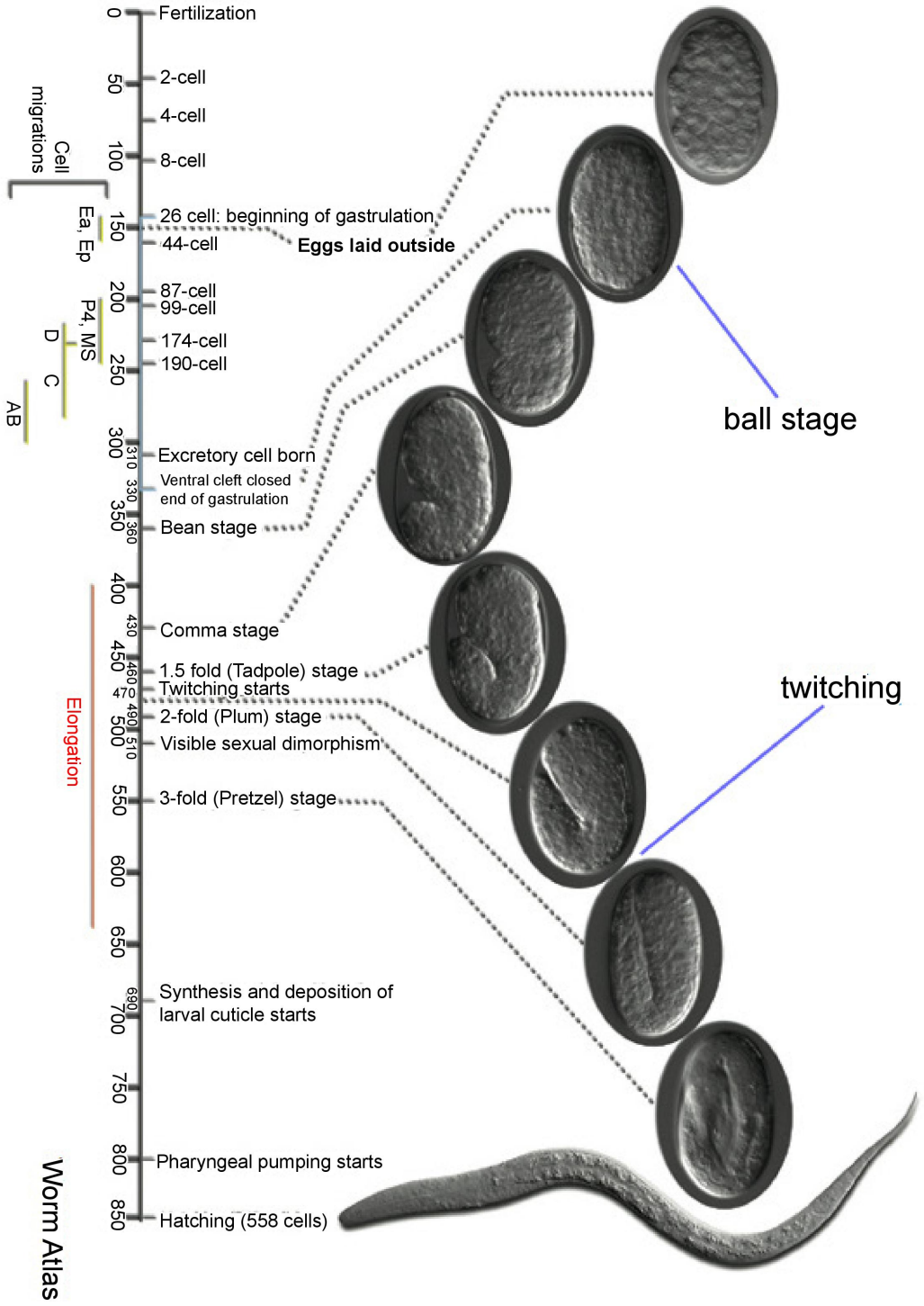
Fertilization
2-cell
4-cell
8-cell
26 cell: beginning of gastrulation
Eggs laid outside
44-cell
87-cell
99-cell
174-cell
190-cell
Excretory cell born
Ventral cleft closed
end of gastrulation
Bean stage
Comma stage
1.5 fold (Tadpole) stage
Twitching starts
2-fold (Plum) stage
Visible sexual dimorphism
3-fold (Pretzel) stage
Synthesis and deposition of
larval cuticle starts
Pharyngeal pumping starts
Hatching (558 cells)
Cell migrations
Ea, Ep
P4, MS
D
C
AB
Elongation
Worm Atlas
ball stage
twitching

The worm embryo develops inside an eggshell having several layers (Stein and Golden, 2015), of which the second to outermost is a thick, chitinous layer which resists mechanical impacts and confines the developing embryo to a fixed extent until hatching. While in the earliest stages the cells of the embryo do not quite fill out the eggshell, a limited overall growth in cellular volume in the first few rounds of division result in the eggshell being filled out by approximately around 100 cells. By the time the embryo consists of several hundred cells, formed as described above by cleavage division without very substantial growth, those cells have become small enough that if just the nuclei alone are examined (for example, with a fluorescent reporter), they appear to extend to near the position of the surrounding eggshell in all directions.

A number of overall morphological changes occur during the course of embryogenesis (Figure 1.4) for example, gastrulation and epidermal closure. Twitching, a period of jerking developmental movements, which might be described as the first obvious signs of nervous system or muscular system activity, begins as the tail wraps around the ventral side of the embryo during "elongation." The animal continues lengthening (Christensen et al, 2015) during the course of the two- and three-fold stages, when it rapidly moves in the eggshell and increasingly resembles a trapped larval worm. Timed aspects of development proceed through these stages until hatching. The initial anterior-posterior axis of the animal is roughly fixed until twitching, while the dorsal-ventral and left-right axes vary over time (see Chapter 3).

Cell lineaging in *C. elegans*

Much of the quantitative biological work done in *C. elegans* has been related to the cell lineage of the animal, which has been observed to be approximately invariant. This has inevitably attracted interest from researchers seeking to understand just how variable "invariant" is, researchers who have also in some cases derived population level information that provides insight into the way that this invariance is produced. As this lineaging work has been a driver of image analysis techniques and tools (some of which were used in my thesis work), and also of specific results of importance for my thesis, it bears covering the major results and papers in this area.

The complete, nearly invariant lineage of *C. elegans* was initially worked out without the aid of fluorescence microscopy, using the differential interference contrast imaging technique (DIC), also known as Nomarski imaging (Murphy, 2001) -- a transmitted light microscopy technique commonly used in *C. elegans*, which essentially visually represents magnitude of optical path length gradients perpendicular to the imaging axis (which can be caused by curvature at the surface of a sample, or by changes in refractive index such as are found at the boundaries of nuclei or in refractive granules) overlaid on absolute transmission intensity. Working primarily by eye, albeit with the early embryonic lineage already mapped out on videotape (Deppe et al., 1978), John Sulston and collaborators (Sulston et al., 1983) mapped out all cell divisions in the embryo until hatching. Having already determined the cell divisions of the larval worm (Sulston and Horvitz, 1977) using a similar methodology, but with the already-hatched

worm pressed under a coverslip to reduce its movements, Sulston was able to identify known larval cells with cells of the two- and three-fold embryo and thus to connect all cells of the animal from the first to the last division. The difficulty of the task of following individual cells and groups of cells by eye in rapidly moving late embryos and wriggling larval and adult worms cannot be overstated. Sulston notes that the electronic noise from videotaping embryos, and the mechanical jitter from movement of the stage during time lapse imaging, rendered late lineaging impossible using recordings, so that his by-hand and by-eye approach provided the highest accuracy possible at the time. (In fact, in my own experience, improvements in camera technology still have not replaced the by-hand approach for DIC imaging.)

Sulston's work is quantitative insofar as specific times post-fertilization are given for particular divisions, and these times are generally considered in the field to be extremely accurate. Nevertheless, the Sulston embryo is a "consensus embryo," derived from an unstated number of individual animals picked up and examined at arbitrary times during development, and "synchronized" by prominent cell divisions. Certainly no error bars can be provided with this method, and only a very limited capacity to compare between animals is possible. Ralf Schnabel and collaborators, working a decade or two later (Schnabel et al, 1997; Schnabel et al 2006) took this a step further. Using a computer controlled multi-focus video microscope, which had been implemented in the *C. elegans* field for studying cortical actin flows in one cell embryos (Hird and White, 1993), Schnabel imaged whole embryos in 4D using DIC. A computerized manual

lineage entering system greatly facilitated the analysis of the movies. (At the time, just introducing a system for archiving and interacting with 4D image sequences was worth a Nature paper -- (Thomas et al., 1996)). Following 8 embryos, some at 20 and some at 25 degrees, for 6-7 hours after fertilization, Schnabel and his group manually lineaged as well as positioned all cells of the embryo until approximately 300 cells (ball stage) and were able to derive a variety of information based on this data. They found substantial variations in individual cell division times, up to +-20 minutes – a finding contradicted by later results from other groups, but which nonetheless provided the first error bars on division timing. Using their positional data, they found that sections of the embryo are filled in by descendants of various blastomeres using a fate-derived movement cue which leads them to the correct location. Blastomeres may establish whole regions of the embryo through movements of their descendants over a restricted patch.

Schnabel et al report widespread developmental rotations at pre-morphogenetic stages of embryogenesis, up to 235 minutes past fertilization. Using the measured positions of known nuclei in the embryo, they attempted to correct for these rotational differences by taking the average rotation about the center axis of certain clusters of cells and unrotating**.** Schnabel noted that these rotations are a serious problem in embryogenesis and may deserve more systematic attention in future, attention which I have endeavored to give in my thesis work to subsequent overall rotations in the embryo which I observed and which occur too late to have been described in Schnabel's paper.

Automation of lineaging efforts

Nomarski imaging, although informative to a human eye, is not well suited for automated computer processing: it provides very low contrast images that cannot be easily understood by a machine (e.g. (Hamahashi et al., 2005)). The introduction of GFP and other fluorescent reporters (Chalfie et al, 1994; Shaner et al, 2005), greatly expanded the facility with which automated lineaging could be accomplished in the *C. elegans* embryo, permitting lineaging which was mostly automated and introducing a range of new image processing techniques to the field.

Zhirong Bao, John Murray, and other researchers working in Bob Waterston's group developed a range of strains containing a pan-nuclear, histone driven fluorophore (eGFP or mCherry), with typically another fluorophore of the opposing red/green color to label particular cell populations of interest. Some of these strains contain markers driven by promoters localized to particular tissues (such as pharynx, or body wall muscle), while others exhibit less tissue-specific expression. (I extensively used the RW11144 strain as well as the RW10029 strains in my own work.)

Using these RW strains, Bao, Murray and collaborators (Bao et al., 2006) developed a system for segmenting fluorescently labeled nuclei from whole embryos, and tracking the nuclei between frames. This method is based on a 3D local maximum approach, in which approximately nucleus-sized regions of the image are binned to find likely nuclear centers; the centers are then shifted by an iterative method until the local fluorescence density looks like a predefined template. For the tracking step, nuclei are

identified with the nuclei in the preceding image (either as being identical to them, or as being their daughters) by finding the nearest match in the previous frame and then employing a heuristic based on shape and fluorescent intensity. Lineaging and segmentation errors can be corrected manually using accompanying AceTree software (Murray et al., 2006). Bao and collaborators used this software to follow the timing of cell division in twenty embryos, with some manual curation, demonstrating among other results on the timing of embryonic cell cycles that individual embryos have overall cell cycle clocks that vary with an s.d. of 4.5% over the period that was lineaged, up to 350 cells. The Starry Nite software was later updated (Santella et al, 2010) to improve the segmentation approach, with a simple 3D maximum approach improved by pre-filtering with a difference of Gaussians filter to improve nuclear detection and a simple ray tracing method used for finding nuclear shape as opposed to the more complicated procedure previously used, in addition to several other improvements. The novel approach dramatically improves segmentation fidelity at later stages of embryogenesis.

This version of Starry Nite was used by researchers in John Murray's lab (Richards et al., 2013), along with an improved confocal microscopy technique which permitted more frequent Z sectioning (resonance-scanning confocal, for faster point scanning, reducing phototoxicity), which allowed automated lineaging of *C. elegans* embryos out to the final stage of cell divisions, but before elongation. Richards et al initially sized embryos using a minimum volume ellipsoid method (Van Aelst and Rousseeuw, 2009), and moved them to a common initial position and orientation, then

tracked the resulting nuclei through time. They report low variation in both cell cycle division timing and position throughout the lineage, with a median variation in cellular position of only 2.2 μm about their reference model.

Software apparently similar to Starry Nite, but with a greater emphasis on progressive manual curation, was employed by researchers in Andrew Chisholm's lab (Giurumescu et al., 2012) to track nuclei through the last round of cell divisions, at a cost of three weeks user time per embryo. Results were provided describing the local topology of nuclear interactions, with number of nearest neighbors tracked in both compressed (coverslip pressing sample to slide) and uncompressed (no coverslip-slide compression) embryos. Compression appears to somewhat reduce movement of individual cells within the embryo (i.e., they have fewer nearest neighbors over their lifetime), but apparently lacking a global coordinate system in which to define movements, they did not report data on specific positioning of the nuclei.

Image registration methods

In my thesis work I captured image sequences taken of different *C. elegans* embryos at different times, in different orientations, and aligned them together to a joint coordinate system. Alignment of visual data is also known as image registration, and it can be done in two dimensions (images) or in three dimensions (stacks of images), or even in four dimensions, as in this thesis. A basic statement of the problem of image registration might be formulated as follows: look for the transformation function F which,

when applied to a first image I_1, best maps it onto a second image I_2; i.e., a function F which optimizes an objective function O of both images. In general, one must always consider the type of correspondence which is to be calculated between images (the objective function O) and the class of allowable transformations F before beginning. Allowable transformations might be restricted to a set of global transformations with a small number of parameters, such as affine transformations (Weisstein, n.d.), or rigid transformations (i.e. isometries), which preserve all distances between points; or to a set of locally varying transformations, which allow nonlinear local shifts in an image subject to regularization conditions that make these problems well-posed. The best known example of a local class of transformations is the set of thin plate spline transformations (Bookstein, 1989). A hybrid of global affine transformations and thin plate splines for local details was used by Hanchuan Peng and collaborators (Peng et al., 2011) to align *Drosophila* brains globally to an estimated 2μm variance.

Classical problems in image registration include aligning images of the same scene from different sensors, finding the best alignment of an imaged object to a template object, and aligning a distorted or moved version of an object onto itself (Brown, 1992); (Zitová and Flusser, 2003). In general, images to be registered cannot be expected to be exactly identical even if "they should be," because sensor noise or photonic noise, as well as differences or movements of the sample or scene between images, or even movement of the sensor, will always play a role. Dealing with variations in the images to be registered registration is therefore a standard problem. Image registration methods have

been used in fields as disparate as medical imaging (Oliveira et al, 2014) and computer vision.

Standard techniques for registering images include global methods such as correlation-coefficient based-methods, which look for maximum correlation between two images, or between an image and a template object, as a function of parametrized spatial transformations of one image; the related (frequency space) Fourier transform methods, which map images onto one another based on phase differences in Fourier space, and which have better characteristics under band-limited noise or differences in scene intensity; or mutual information based methods (Maes et al, 2003).

Another wide class of registration methods, in which the method that I developed for my thesis is situated, functions by first establishing a set of points of interest in an image and then seeking to match these onto corresponding points or regions in a target image directly. This point alignment problem comes in two main flavors, sometimes referred to as control point matching and point set registration.

In control point matching, the same set of points is enumerated in two images, with the correspondence known a priori; this problem is exactly solvable, in a least squares sense, for noisy control points the positions of which do not exactly correspond in two images (Horn, 1987). Horn found a fast, closed-form solution for more than three points in test and reference images in three dimensions, using the allowable transformations of scaling, rotation, and translation; i.e., for transformations which were rigid up to an overall scale factor.

While exact solvability is obviously appealing, the general problem with control point methods is that they require identification of specific, named points in images. This might work in a case when identity of all cells or tissues in a biological image is already known, but, for example,this was not the case for my own imaging for which identity of the points to be registered was not generally established.

Recently, researchers have introduced a control point alignment method used for registering late *C. elegans* embryos, from 1.5-fold stage through hatching (Christensen, Santella, Bukinsky, Wu et al, 2015). The method works by segmenting out the seam cells, a bilaterally symmetric set of epithelial cells that extend for the length of the animal, providing a set of fixed points with which to "untwist" local rotations and translations in the animal. Using this method to straighten the animals, the authors derived results on the growth of the worm during the three-fold stage and also were able to track positions of the neurites of the ALA neuron, a neuron (mentioned previously) which is located in the dorsal part of the head and is implicated in a variety of behaviors including sleep (Hill et al., 2014) and locomotion (Fry et al., 2014).

The other class of point-based methods, point set registration, involves matching two sets of points, not necessarily of the same length, and with the correspondence not known in advance. In general, because of the large number of degrees of freedom involved with a large number of points all moving independently, these point set registration methods are iterative and search locally for correspondences at each step. The classic algorithm in this area is the Iterative Closest Point (ICP) algorithm (Besl and

McKay, 1992), which functions by matching points in a test image to the closest target points at the current iteration, conducting a global registration according to Horn's Method, and then re-updating the correspondences between test and target points after movement. After several rounds of such iterations, points no longer move substantially between iterations (as judged by a defined threshold) and the points are considered matched.

Development of matching methods related to ICP has been an active area of investigation, with improvements generally relating to improving the resilience of the matching to outlier points and noise as well as avoiding local minima in the matching (Gold et al., 1997; Chui and Rangarajan, 2000); Luo and Hancock, 2003).

The method used for point matching in my thesis work is the rigid-transform (no scaling) version of Coherent Point Drift matching (CPD) (Myronenko and Song, 2010). The Coherent Point Drift algorithm functions by treating points in one image as a set of Gaussian distributions with their means centered on the current point position, and then solving a maximum likelihood problem (Myung, 2003) for the positions of the other set of points relative to the first set of Gaussians. A uniform distribution is added to the Gaussians to permit inclusionof points which are nowhere near points in the other set (outliers). The width of the Gaussians is dynamically reduced over time, which effectively permits a very wide range of possible point matches at the start with diminishing matches available over time. I found this method to be much more effective than ICP in tests. (The phrase Coherent Point Drift refers to a local nonrigid alignment

method distributed with the software, which I never used, preferring to keep the embryo geometries intact.)

The *C. elegans* nerve ring

The main biological component of my thesis work centers on the placement of the nerve ring in the *C. elegans* embryo prior to twitching. The nerve ring, sometimes described as the "brain" of the animal, is the main neuropil in *C. elegans,* containing many of the animal's synapses between interneurons, motor neurons, and sensory neurons. Processes wrap around the animal's pharynx (Figure 1.5) forming the ring structure and synapse onto one another en passant (Jin, 2005). Of the 302 neurons in the adult hermaphrodite, 180 send axons to the nerve ring (White et al., 1986; Zallen et al., 1999).

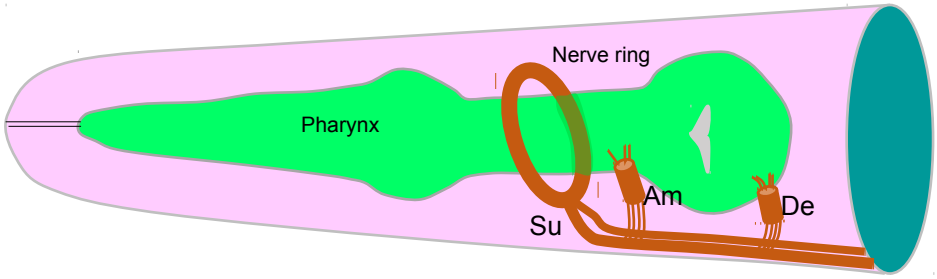

Adapted from Worm Atlas

Figure 1.5: *C. elegans* nerve ring model

The *C. elegans* nerve ring wraps around the pharynx (green) of the animal, with axons growing in to the nerve ring through a variety of commissures. Marked are the amphid and dereid commissures, which execute turns before entering. The sublateral neurons enter the nerve ring from immediately ventral of the ring without turning.

While neurons continue to project axons into the nerve ring throughout late embryogenesis (Rapti et al, unpublished) by several commissures, including the amphid commissure, the dereid commissure, and the sublateral commissure, the structure itself is formed prior to the twofold stage, before the series of rapid embryonic movements called twitching begins. Recent work from the Bargmann lab (Kennerdell et al., 2009) has shown a special role for the sublateral neurons in formation or maintenance of the nerve ring, with ablation of the SIA, SIB and SMD sublateral motoneurons using a promoter acting at the comma stage (Harfe and Fire, 1998) resulting in a 20% defect in nerve ring placement. The authors speculate that the small size of the defect results from inefficiency of the promoter in killing sublateral neurons, with at least one sublateral neuron surviving in each worm for which the ablation was conducted.

In the same work (Kennerdell et al., 2009; Kennerdell,2008), a genetic screen was carried out in larvae to identify nerve ring placement defects. The Wnt pathway was especially implicated as having a role in nerve ring placement, with the Wnt homolog *cwn-2*, the frizzled homolog *cfz-2*, and the Ror homolog *cam-1* all identified in the screen. Cell specific rescue experiments done with *cam-1* show that it acts in the sublateral SIA and SIB neurons, suggesting a role for *cam-1* in placement of the nerve ring structure.

Recent work conducted in our laboratory provides strong additional genetic evidence that the nerve ring is pioneered by the sublateral interneurons SIA and SIB (Rapti et al, in preparation). These neurons remain the earliest that have been observed to

enter the nerve ring, from among dozens that have been imaged (Georgia Rapti, personal communication).

Work from our laboratory has additionally clarified possible roles of glial cells in nerve ring assembly. Satoshi Yoshimura (Yoshimura et al., 2008) discovered a role for the CEP sheath glia (Oikonomou and Shaham, 2011) in establishing or maintaining nerve ring structure. Georgia Rapti has observed (Rapti et al, in preparation) CEP sheath glia and sublateral neurons extending processes in or next to the nerve ring at approximately the same time, suggesting the possibility that the CEP sheath glia may be directly involved in its construction.

Chapter 2: Construction and Operation of a SPIM Microscope

Summary

High speed, low phototoxicity microscopy is of critical importance in imaging developing embryos with sufficient temporal resolution to observe developmental changes as they occur. To facilitate studies in our laboratory on developmental processes in the *C. elegans* embryo, I have built a functional single plane illumination microscope (SPIM). The design largely follows previous work from the Shroff lab (Wu et al, 2011), with some notable differences, among which is the use of a scanning galvanometer rather than a cylindrical lens for light sheet creation. The microscope was constructed independently after a two-day visit to the Shroff lab in which the layout and operation of their microscope was observed, based on notes and recollections of their setup and descriptions from Wu et al. Additional assistance was provided in the form of a simple Labview control script for their microscope provided by Yicong Wu, which was substantially altered to form the Labview control software used here.

Microscope parts and general design

Figures 2.1 - 2.3 show the light path and optical components of the SPIM microscope, with Figure 2.1 providing an overall view. Figure 2.2 presents the

microscope optics and light path on the optical table, while Figure 2.3 presents the optics and light path within the microscope body.

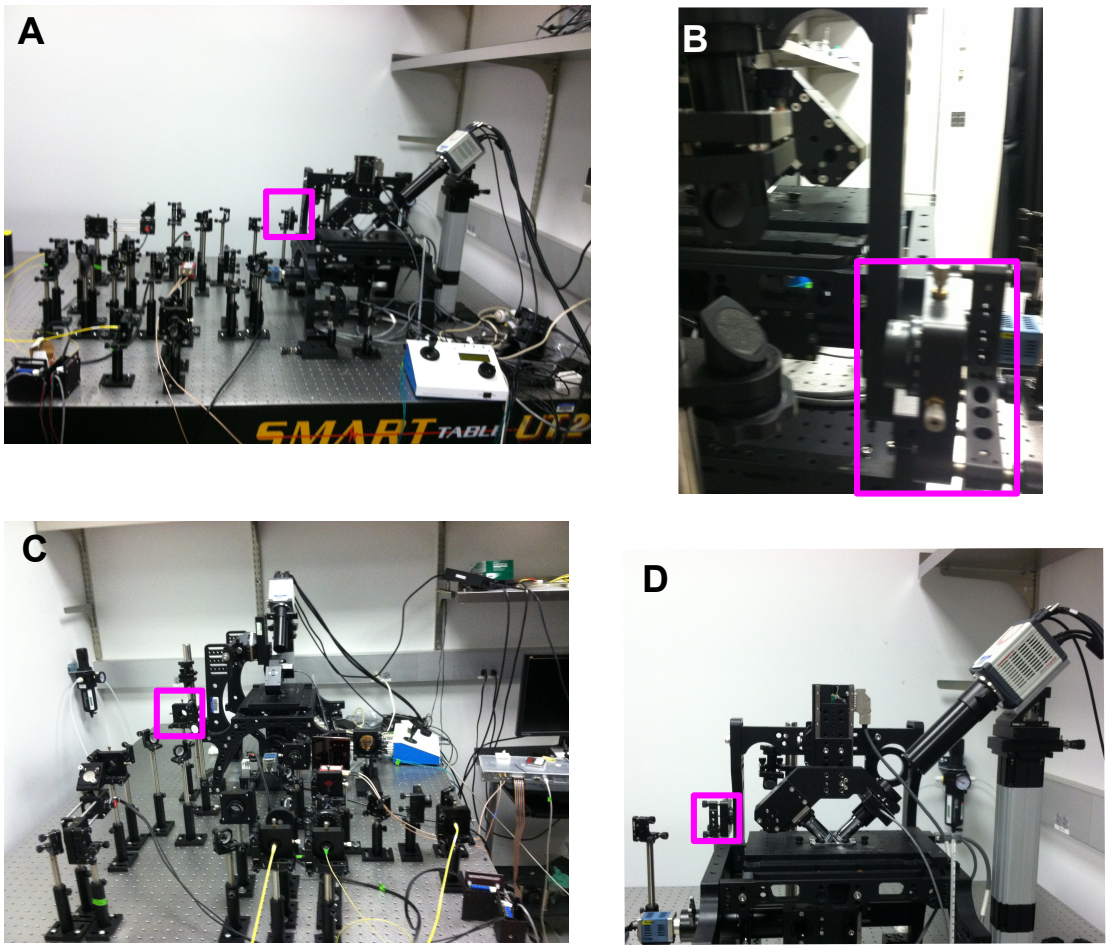

Figure 2.1: Overview of SPIM microscope optics

Photographs are presented of all externally visible microscope optics. The 500mm lens is outlined in magenta as a guide to the eye in translating between views. **A:** Front view. **B:** Back view. **C:** Side view. **D:** Microscope main body view.

Figure 2.2: SPIM optical table light path

A diagram of the light path on the optical table, with the light path within the microscope body provided in a separate figure. A 488nm and a 588nm laser are combined by a long-pass beamsplitter and run through an accoustic optical tunable filter (AOTF) used for beam shuttering. On the way to the microscope body the beam encounters a variety of optical elements, most notably a pair of galvanometers which are used to scan the beam and generate the light sheet and volume. Mirrors and relay lenses are used to reimage the galvanometers onto the back focal plane of the excitation objective, which has the effect of converting the angular shifting of the laser beams by the galvanometers into positional movement at the sample. Further details are presented in the main text.

A: Front view of microscope. **B-C**: The light path is traced on the optical table, with the periscope and back port of the microscope broken out for a clearer view. **D**: Diagram of the light path through the optical elements on the table. Mirror 1 is conjugate to the sample plane and can be used to adjust angles at the sample. Mirrors 2 were important in aligning the microscope and are described in the main text. **E.** Legend for B., C., D.

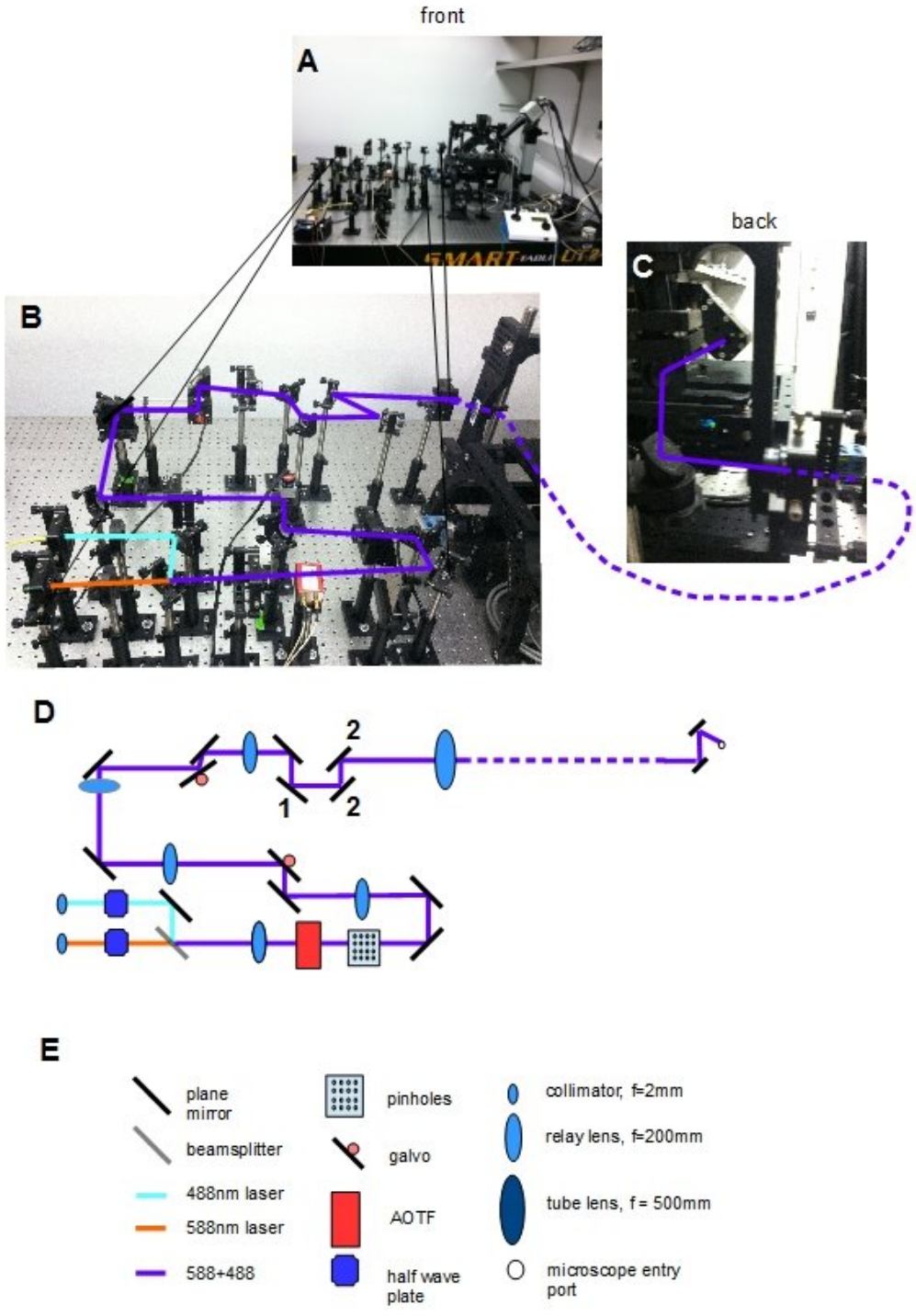
front
A
back
C
B
D
2
1
2
E
plane mirror
beamsplitter
488nm laser
588nm laser
588+488
pinholes
galvo
AOTF
half wave plate
collimator, f=2mm
relay lens, f=200mm
tube lens, f = 500mm
microscope entry port

Figure 2.3: Microscope body light path

A diagram of the light path in the microscope body. Excitation light (purple) is focused onto the sample by the excitation objective ("Ex"), producing fluorescence (magenta) which is collected by the emission objective ("Em"). Laser excitation light may also be collected by the underside objective; for a low numerical aperture objective (e.g., a .3 NA), this will only be by scattering; for a higher numerical aperture objective (e.g. 1.3) directly transmitted laser illumination will also be acquired. **A:** Front view of microscope. **B**: Light path drawn on front view of microscope for excitation and emission light. **C:** Diagram of light path and optical components. **D:** Legend for B.,C.

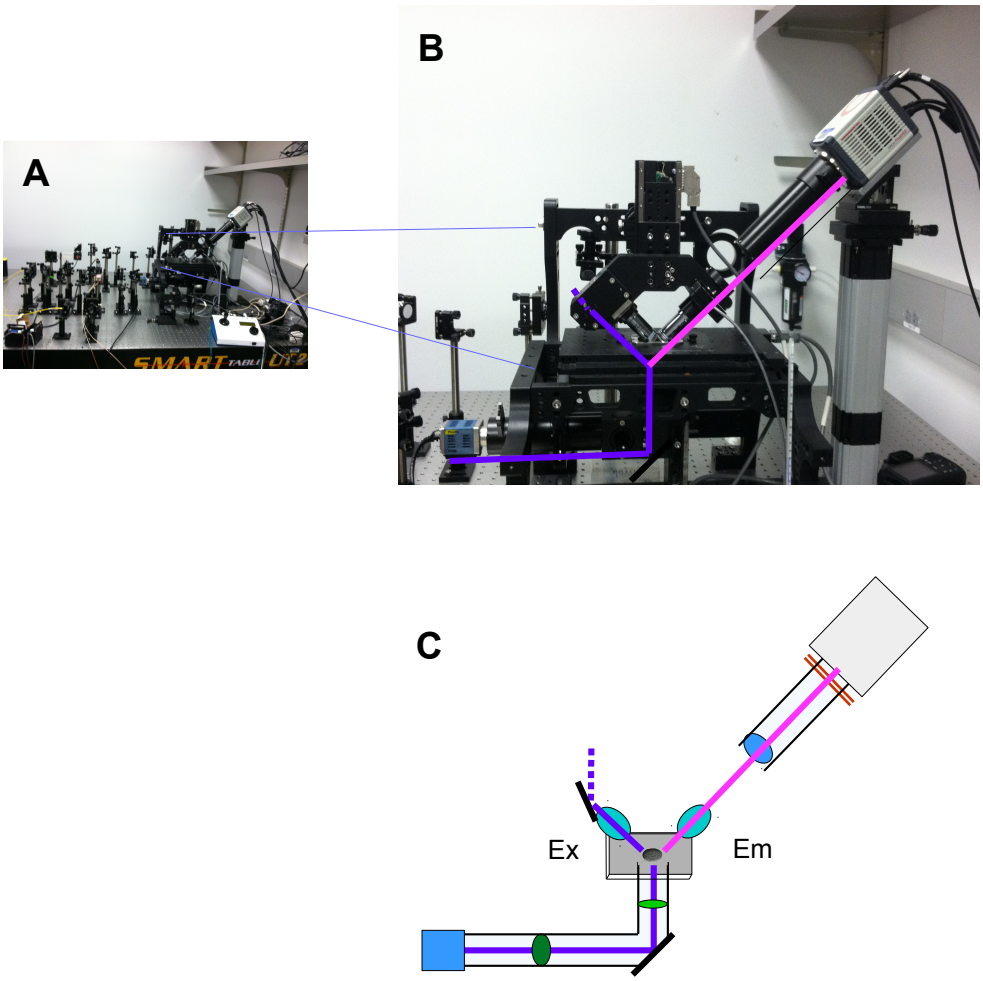
A
B
C
Ex
Em
D
sample-finder camera (Pixelfly)
sample chamber
sCMOS camera (Hamamatsu)
color filter
40x .8 NA SPIM objective
.3 NA sample-finding objective
100mm tube lens
plane mirror
200mm tube lens
excitation light
emission light
sample

Two laser lines outputting single mode Gaussian beams (Figure 2.2) – a 20mW 488 nm laser for GFP imaging (Thorlabs S3FC488), and a 40mW 588nm laser for mCherry imaging (Coherent Sapphire 588-FP) – are collimated (2 Thorlabs CFC-2X-A collimators) and coupled into one light path by a dichroic mirror (Thorlabs DMLP505). The beams are then passed through a pair of half wave plates (Thorlabs WPH05M-488 and WPHH05M-532), and then an acoustic optical tunable filter (AAoptoelectronic AOTFnc-400.650-TN), which diffracts up to 4 distinct colors with electronically controllable densities in each diffraction peak, used for beam shuttering and power modulation. The half-wave plates are rotated to polarize the incoming beams to the correct linear polarization for optimal diffraction efficiency at the AOTF. After passing through the AOTF the beams focus down onto a chrome-on-glass photomask (Photo-sciences.inc), with an array of pinholes which can be used to truncate the beams to various sizes. In practice we only ever use a pinhole of 2.1μm radius

We always align the pinhole to the first order diffraction peak out of the AOTF rather than the zeroth because the efficiency of shutting off the first peak has been low with our device, while nearly all of the power (>99.99%) can be turned on and off past the filter with the AOTF, using the first order peak. This comes at the expense of a very low coupling efficiency at this point -- approximately 90% of the 588 light is lost at the AOTF while 60% of the 488 light is lost. These losses are not a problem because of the extremely low power levels needed for SPIM. The 488 and 588 lasers were of the lowest power available from their respective manufacturers, and only perhaps 10% of the full

power output is ever used in imaging even after the losses at the AOTF (and the further losses at the pinhole, which in current alignment are an additional 10% of 488 nm and 60% of 588 nm).

The pinhole mask is conjugate to the sample plane, separated from it by six lenses in 4-f configuration pairs, which reimage objects at twice the first focal length plus twice the second focal length (without altering angles or positions relative to the optical axis, if the two focal lengths are equal). The 4-f lenses consist of two pairs of relay lenses – 4x 200mm Thorlabs achromats (AC254-200-A-ML) -- followed by a tube lens / objective pair, consisting of a 500mm Thorlabs achromat (AC254-500-A-ML), and an excitation objective with a 5mm effective focal distance. This optical arrangement demagnifies the beam passing through the mask pinhole by 100 times and reimages it onto the sample. On its path to the excitation objective, the beam impacts two galvanometers (GVSM001), both conjugate to the back focal plane of the objective. For an object located in the back focal plane of a lens, positional movement is essentially converted to angular movement at the front focal plane and vice versa, angular to positional; the six lenses are aligned to the galvanometers so that rotating the beam using the galvanometers translates to positional movements of the beam in the sample volume, with two axes of movement permitting volumetric scanning. The laser is brought up from near the level of the table to the level of the back port on the microscope using a periscope (Thorlabs RS99).

See Figure 2.3 for a representation of the microscope body optics and light path. The excitation and detection objectives (Nikon 40x .8 NA MRD07420 water dipping) are

mounted at 90 degrees to one another on a specially-designed SPIM frame obtained from Applied Scientific Instrumentation (ASI; Wu et al, 2011). A third, 10x low NA (.3 NA) objective (Olympus UPLFLN10x2) is arranged in the typical inverted microscope configuration, confocal with the two top objectives, and is used for locating and centering samples. Samples are mounted between the objective by attaching them to a 24x50mm coverslip with polylysine. The coverslip itself is secured in a sample chamber open on the side which faces the detection and excitation objectives (so that the coverslip is presented to the bottom objectives). An O ring around the coverslip makes a water-tight seal when the top half of the chamber is pressed tightly to the bottom with thumbscrews. The sample chamber can be filled with water, M9, or any other water-based medium (the medium must have index of refraction 1.33). The sample chamber is mounted with clips on an X-Y stage.

A piezoelectric device (ASI APZOBJ-200) is used to track the imaging objective up and down in synchrony with the galvanometer scanners, so that the plane illuminated by the excitation objective is imaged in focus onto the camera. The imaging objective and tube lens transmit light through a dual color emission filter (Chroma 59022m) to a Hamamatsu Orca Flash 4.0 camera, which is a fast modern sCMOS capable of taking 100 frames per second at full frame and over 600 FPS if the frame is trimmed to the size of the embryo and centered. Since we use a dual color filter, the color imaged at a given time is entirely controlled by the choice of excitation light (through the AOTF).

The underside light path (10x objective) brings light down through a 100mm Nikon tube lens to a CCD camera (Pixelfly QE). (Originally a Canon T3 Rebel commercial CMOS camera was used, but it was found to be too insensitive for some applications.) Ceiling lighting in the room is sufficient to form an acceptable white light image of embryos or other samples.

The microscope stage has 5 axes of control. The axes are defined as: "F," which controls the vertical position of the top block; "Z" which controls the vertical position of the underside objective; "X" and "Y" which control the position of the stage, moving it in its plane; and "P" which controls the position of the piezo and thus of the detection objective. All axes of motion can be addressed either directly using the physical controls provided on the ASI controller or indirectly through a USB or RS232 connection using serial commands. The piezo can additionally be controlled with an applied voltage, with the position linearly tracking voltage (0-10V) across its 200µm range.

During image acquisition, the scanning galvanometers and the piezo are controlled by a pair of DAQ cards (NI PCIe-6363). The camera acquisition is likewise triggered off of one of the DAQ cards. All hardware is operated through custom software written in Labview and running on a SuperMicro workstation running Windows 7 64 bit Professional. The various electronic components are synchronized using a mix of software and hardware synchronization (see Main Scan section for more detail).

All microscope optical elements mounted on the table are 1 inch (25.4 mm) in diameter. All lenses including the collimators were mounted on 6-axis mounts (Thorlabs

K6X), which permit small adjustments in X, Y, and Z position as well as substantial tip, tilt, and (unused by us) axial rotation. Most mirrors were mounted on KM100, 2 axis mounts (tip, tilt) except a few which were mounted on KS1 3-axis mounts (tip, tilt, Z) when a fine Z positioning adjustment was required (all used in the tight spacing near the first galvanometer in the light path). All optical elements (except the periscope, which is secured to the table with an adjustable clamp, Thorlabs PF175) are mounted on BA2 bases, which can be screwed to the optical table anywhere along their 1.25 inch length slots. Typical breadboards have screw slots placed every .98 inches (metric) or every inch (Imperial) in a square configuration. The 1.25 inch travel range of the BA2 therefore permits optical elements to be placed at arbitrary positions on an optical table in the slot direction.

The microscope was initially mounted on a 4' by 2.5' optical table (Thorlabs SDP75120 base and PBH11112 breadboard), which uses hand-pumped balloons for vibration isolation. Subsequently the microscope was moved to a new room and an 8' by 4' optical table (Newport S-2000A-423.5 isolators and ST-UT2-48-12 breadboard) with superior, metered vibration isolation using wall-supplied air.

Microscope construction and alignment:

The 4' by 2.5' optical table on which the microscope was initially built was the largest that could fit in the room we devoted to the project. The use of 200 mm relay lenses -- recommended to me by Yicong Wu over shorter focal length alternatives,

because the longer focal length makes them more resistant to errors in positioning (by, e.g., the thin lens equation – Hecht, 2016) – meant that the footprint of the microscope was on the large side compared to the table and required careful planning to fit everything into the allotted space. The collimators sat on one corner and the microscope body on the other corner on the same side, both facing the user, with the lasers mounted off the table and fed into the collimators by fiberoptic cables. The microscope was directly transferred from its position on the old optical table to the new table.

After placement of the microscope body and the collimators, the optics were constructed approximately in the the order of the beam trajectory. I checked each component as it was placed to verify to the extent possible that it was in the right position before continuing on to the next one. Unfortunately, movements of a component downstream in the light path frequently required substantial realignment of other components upstream of it, in order to redirect light to the new position. The situation could have been simplified somewhat by using larger mirrors and lenses (at a somewhat higher overall price for the microscope), since the biggest problem occurs when large shifts cause the beams to fall off the edge of an optic necessitating a shift in the position of the (BA2) slotted base.

Since the 4f configuration of the lenses required 2.4 meters of total light path, I used a set of 8 mirrors (counting from after the first relay lens) to tile the light backwards and forwards in order to increase the optical path length covered on the small area of the original table. Lenses and mirrors were positioned using a ruler to measure distances to

the centers of the mounted lenses, under the assumption that the apparent centers of the (doublet) lenses would correspond to their optical centers. X-Y-Z positions of mounts and bases on the optical table were continually updated as beam angles and positions were changed to ensure that the 3D distance between the parts of the optical components seen by the beams remained correct (the 25.4 mm diameter of the optics is a not inconsiderable fraction of the typical 200 mm focal length of the lenses, so that these shifts across an optic might lead to noticeable errors). The slotted bases of the optical components permit coarse positional adjustments of components, and when translational adjustment of lens or mirror mounts were available this was also used, permitting ultra-fine corrections over a small range.

I initially worked only with the 488 nm laser, adding the 588 nm laser after the microscope was completely aligned to the 488, and then aligning the 588 laser using the existing 488 position as a guide. The AOTF and the pinholes were also added after the microscope was set up, with some shifting of existing components to accommodate them.

Although final alignment of the optics required imaging the beam in the microscope to observe its trajectories under galvo scanning, I was able to roughly align the optics first by noting the behavior of the beam under galvanometer movements at positions two lens focal distances away from the galvos, where rotations of the galvanometer are translated into positional shifts. The room in which the microscope was constructed was quite dusty, and while this was surely not good for the optical components it was found to be very helpful in alignments, as with the light off I could

directly see the 488nm laser propagating in the air as it scattered off the dust motes. I shifted optical positions and alignments until the beam trajectories seemed correct in the region around the angling mirror conjugate to the sample plane (marked 1 on Figure 2.2); approximately correct alignment was considered achieved when the movements of the beam under the galvanometer rotations were symmetrical about that mirror, with no obvious bending or twisting incoming to it or outgoing from it.. I lastly inserted the 500mm tube lens to finish the table optics. The pair of mirrors before the 500mm tube lens could be moved together to add path length without substantially affecting the position or angle of the laser heading into the 500 mm lens. I adjusted these mirrors as well as the 500mm lens position until the distance from the 500mm lens to the objective (based on descriptions of path length within the microscope provided by ASI and external measurements by ruler) and mirror 1 seemed approximately correct.

Fine alignments required imaging the beam in the microscope optics, which was accomplished easily by observing the scatter of the beam off of the water (Figure 2.4) in the sample chamber. First the beam was roughly aligned to the microscope body by extracting the lens from one side and maneuvering the periscope mirrors at the back of the microscope until the beam could be viewed by eye down the slot for the objective. (The adjustable focus, low numerical aperture lens of the human eye permits it to find a beam which is at arbitrary distance away, when with a high numerical aperture, i.e. low depth of field, lens the same beam can't be seen.) This method is used to approximately center the beam in the field of the detection objective, but gives no information as to the

P-axis position of the beam. I replaced the objective and mounted a camera, and slowly screwed and unscrewed the detection objective in its slot until the beam began to be visible. Further adjustments of the objective and of the mirrors were performed until the beam came into focus. Although easy to describe in theory, in practice, this was a very complicated procedure since changes in one part of the system often required compensation in another part. The beam must enter into a small slot in the back of the microscope body (Figure 2.2), and the angle and position of the beam at the slot can vary only slightly or no light will propagate further down the light path to the sample. The alignment involved many components each with several degrees of freedom and no clear readout until the beam became visible. Both objectives needed to be moved simultaneously before the beam could be viewed in the detection objective. Then the excitation objective could be screwed in and out until the beam waist appeared in the frame visualized by the detection objetive. Once the beam waist became visible and was roughly centered in the detection objective, both objectives were locked in position with provided lug nuts. The in-focus beam must be viewed with a color filter (nominally blocking the excitation light) in place, or else it will saturate the camera and the exact position of the waist be invisible, as well as possibly damaging the camera sensor. Although the Chroma color filter obviously permits excitation light through, or this procedure would not work, imaging quality is not substantially degraded during regular imaging since the beam is barely visible at normal powers and exposure times, which are much lower during regular imaging than during beam observation.

Figure 2.4: Visualization of the beam and light sheet

A: Visualization of the light sheet. The beam is scanned at a multiple of the camera exposure rate, generating the appearance of an even sheet. The top half of the image shows scatter in water; the bottom half shows the stronger scattering in the coverglass. The interface between the two is the white spot of B, below.

B: The laser is visualized by scatter in water and glass as in A. Left: The laser is incorrectly adjusted, with the F axis set too high and the beam waist off the surface of the coverslip. The large, bright white spot is the reflection and scatter from the point where the (diverged) beam crosses the coverslip. Right: The crossing point is correctly situated at the bottom of the beam waist, so that the full waist sits directly on top of the coverslip. This aligns the beam waist to an embryo sitting on the coverslip; an offset is then set in software from this middle position to bring the top of the scan volume up above the embryo. The marked lines on the beams are ~2.5μm.

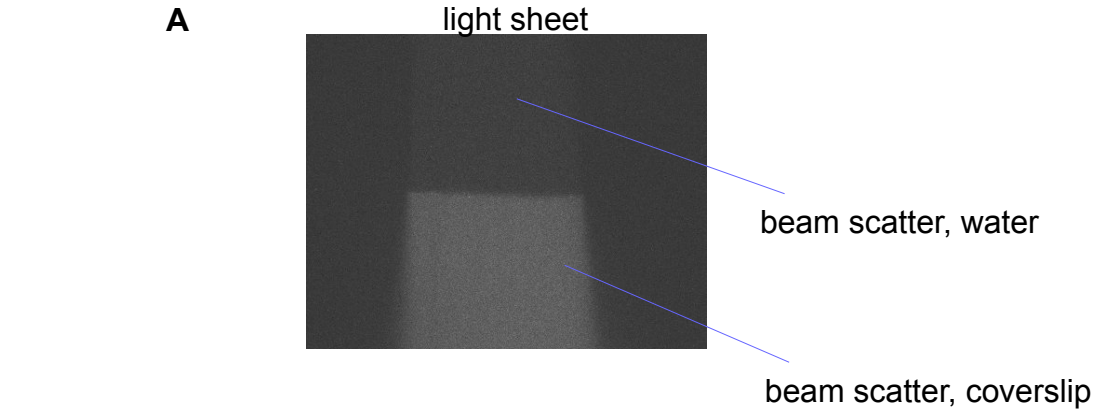
A
light sheet
beam scatter, water
beam scatter, coverslip

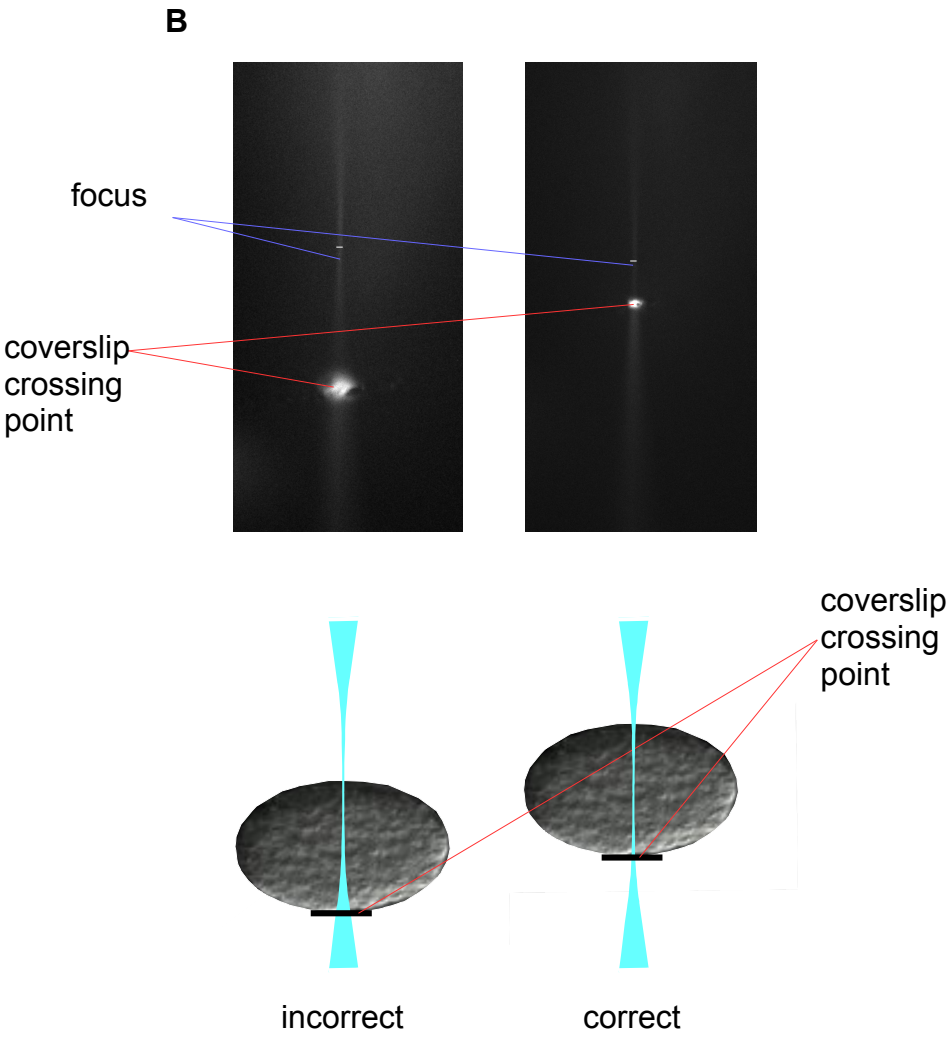
B
focus
coverslip
crossing
point
coverslip
crossing
point
incorrect
correct

Finally the underside objective was brought into position like any other microscope objective, by observing samples on the coverslip. It could be aligned to the top axis in Z by simultaneously imaging the surface of a coverslip in the detection objective and in the underside objective. Secondly, the entire top block is shifted in X and Y by two screws provided on the microscope until the foci of the underside objective and the detection objective coincide. At this point all three objective foci roughly coincide.

The angle of the detection objective can be adjusted using three screws provided behind the piezo objective, at the same time as mirrors are moved, until the beam appeared maximally elongated in the detection objective.

The light sheet could be visualized directly in water (Figure 2.4) or preferentially using a living, fluorescing sample. The galvanometers were calibrated (i.e., correct voltages were determined) and extensive adjustments made to the system until the beam appeared to track approximately straight across its range of motion (actual angular movement during scan is **on the order of**5 degrees). Additional adjustments were required to ensure that the beam tracked approximately vertically with the orthogonal linear combination of galvanometer movements. The correct piezo voltage per micrometer of movements was adjusted from the nominal value by trial and error in three dimensional samples until an entire fluorescent volume, i.e. a *C. elegans* embryo with fluorescing nuclei, appeared to be in focus under the volumetric imaging.

Control software

The control software was programmed in Labview and is structured in several stages: first, a user-facing part ("main SPIM module"); second, a "main scan" program which actually executes the imaging procedure called for by the user in the main module; third, subordinate routines called by one or both routines, which are mostly invisible to the user. (Figures 2.5 – 2.7).

Figure 2.5: Overview of Labview control software interface

A screenshot is presented showing the general layout of the user-facing part of the Labview Main Module program. The user can enter various parameters relating to the the light sheet acquisition and specify positions of embryos to acquire.

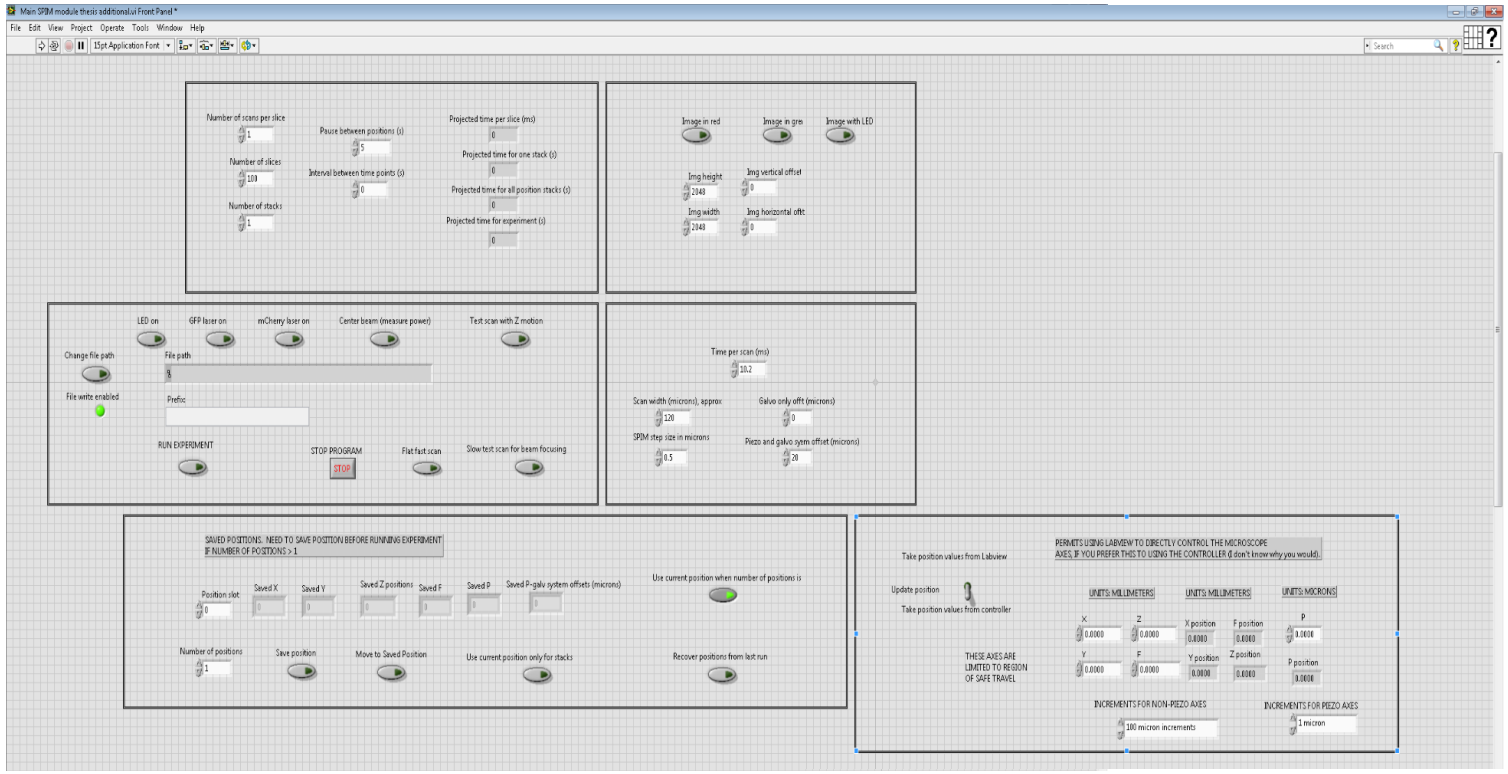
Main SPIM module thesis additionalui Front Panel *
File Edit View Project Operate Tools Window Help
15pt Application Font
Search
Number of scans per slice
Pause between positions (s)
Projected time per slice (ms)
Number of slices
Interval between time points (s)
Projected time for one stack (s)
Projected time for all position stacks (s)
Number of stacks
Projected time for experiment (s)
Image in red
Image in grn
Image with LED
Img height
Img vertical offset
Img width
Img horizontal offt
LED on
GFP laser on
mCherry laser on
Center beam (measure power)
Test scan with Z motion
Change file path
File path
File write enabled
Prefix
RUN EXPERIMENT
STOP PROGRAM
STOP
Flat fast scan
Slow test scan for beam focusing
Time per scan (ms)
Scan width (microns), approx
Galvo only offt (microns)
SPIM step size in microns
Piezo and galvo sym offset (microns)
SAVED POSITIONS. NEED TO SAVE POSITION BEFORE RUNNING EXPERIMENT IF NUMBER OF POSITIONS > 1
Position slot
Saved X
Saved Y
Saved Z positions
Saved F
Saved P
Saved P-galv system offsets (microns)
Use current position when number of positions is
Number of positions
Save position
Move to Saved Position
Use current position only for stacks
Recover positions from last run
Take position values from Labview
PERMITS USING LABVIEW TO DIRECTLY CONTROL THE MICROSCOPE AXES, IF YOU PREFER THIS TO USING THE CONTROLLER (I don't know why you would).
Update position
Take position values from controller
UNITS: MILLIMETERS
UNITS: MILLIMETERS
UNITS: MICRONS
X
Z
X position
F position
P
Y
F
Y position
Z position
P position
THESE AXES ARE LIMITED TO REGION OF SAFE TRAVEL
INCREMENTS FOR NON-PIEZO AXES
100 micron increments
INCREMENTS FOR PIEZO AXES
1 micron

Figure 2.6: Labview imaging parameters

Screenshot showing user-definable parameters in Labview governing aspects of the light sheet imaging protocol, such as time per scan (which controls frequency of galvanometer light sheet creation as well as camera acquisition time), beam scan width, and camera ROI controls. From these inputs the user can call a variety of "test scans" which are used for alignments, as well as activate the main scan program, which starts the specified time lapse 4D imaging procedure. Further details in the main text.

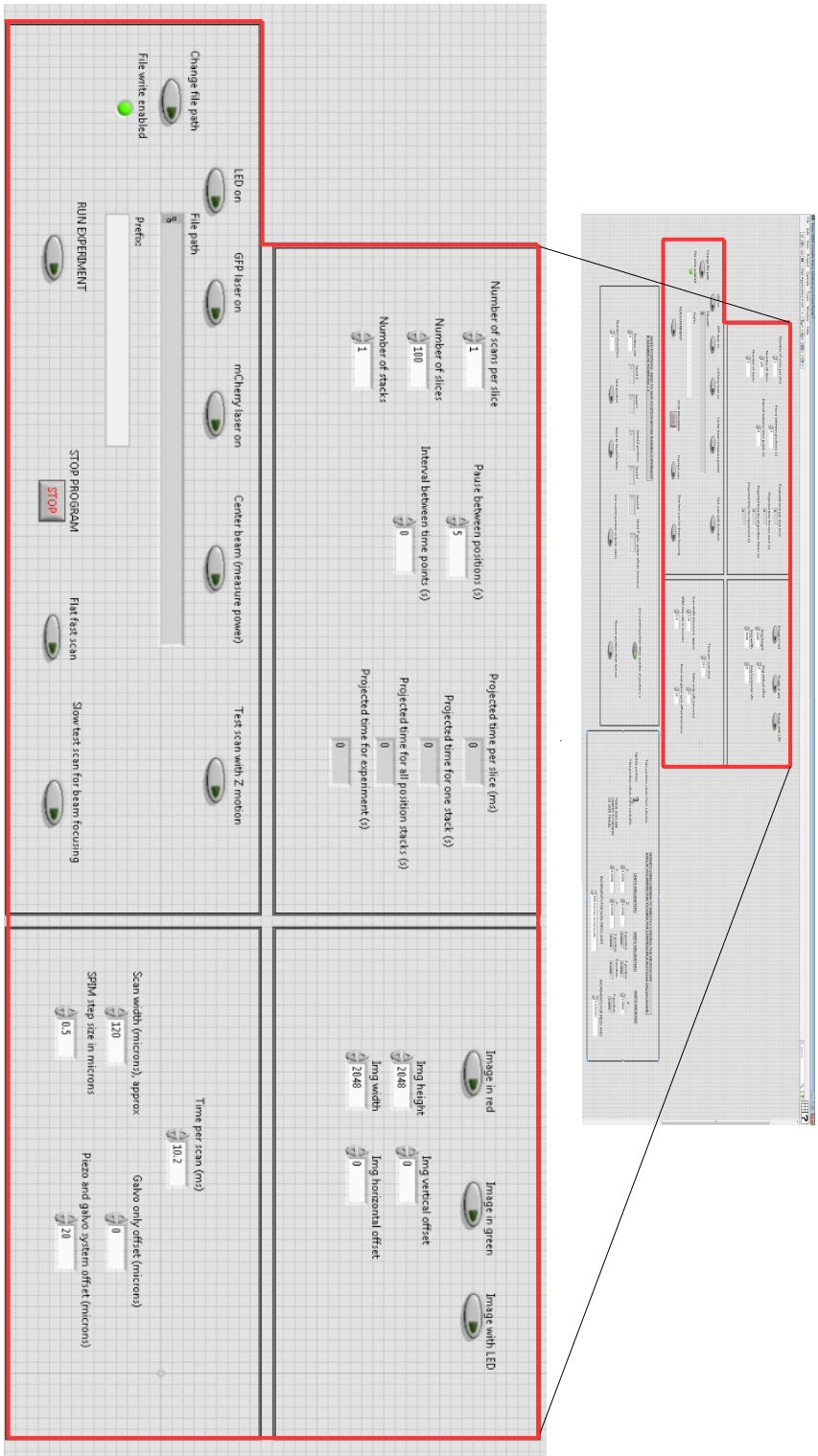
Number of scans per slice
Pause between positions (s)
Number of slices
Interval between time points (s)
Number of stacks
Projected time per slice (ms)
Projected time for one stack (s)
Projected time for all position stacks (s)
Projected time for experiment (s)
Image in red
Image in green
Image with LED
Img height
Img vertical offset
Img width
Img horizontal offset
LED on
GFP laser on
mCherry laser on
Center beam (measure power)
Test scan with Z motion
Change file path
File write enabled
File path
Prefix
RUN EXPERIMENT
STOP PROGRAM
STOP
Flat fast scan
Slow test scan for beam focusing
Time per scan (ms)
Scan width (microns), approx
Galvo only offset (microns)
SPIM step size in microns
Piezo and galvo system offset (microns)

Figure 2.7: Labview positional parameters

Screenshot showing the Main Module controls having to do with setting embryo positions for acquisition in the main 4D acquisition ("main scan") module. Users can choose between entering positions manually in Labview or setting positions based on the current position of the ASI stage controller. Further details in the main text.

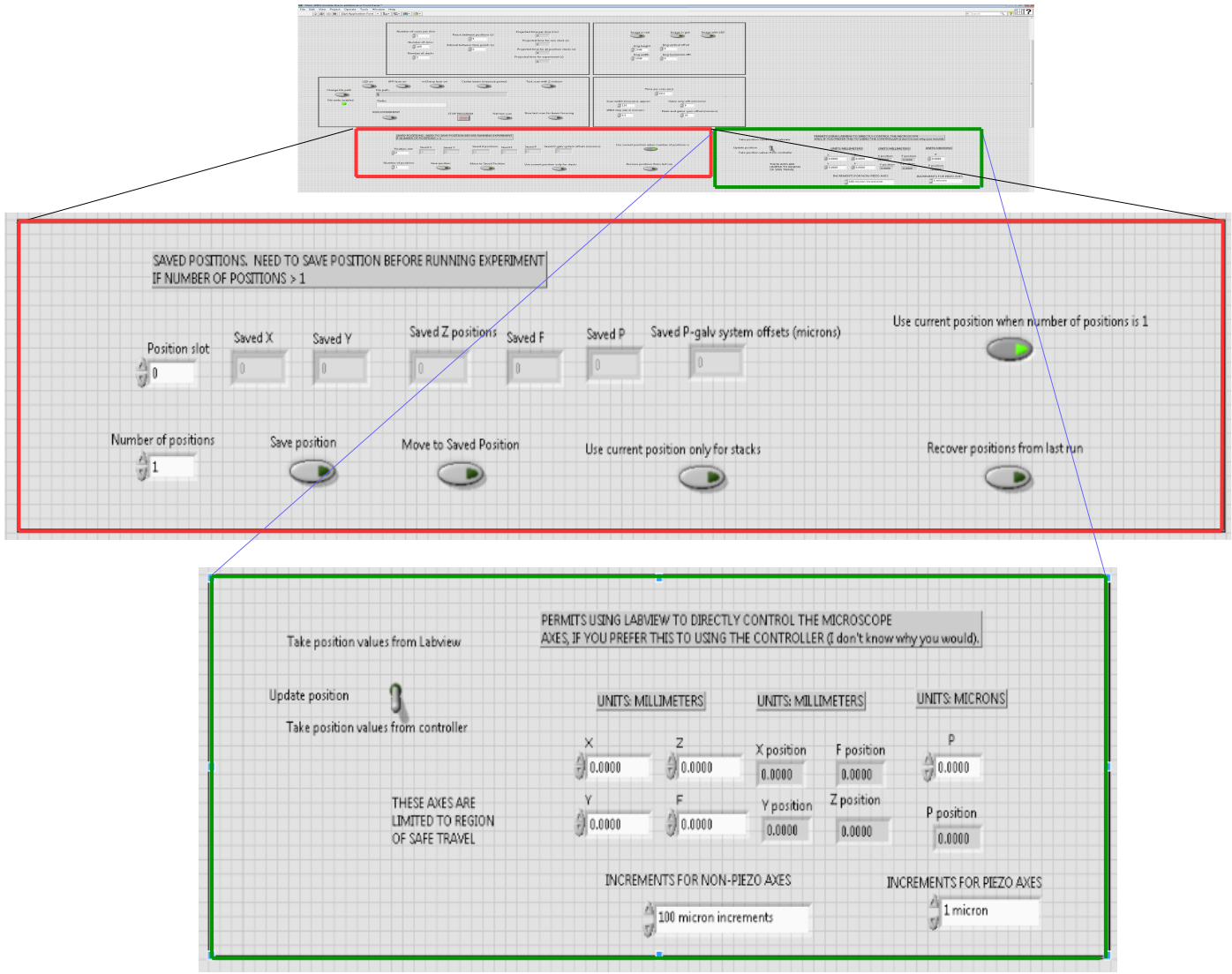
SAVED POSITIONS. NEED TO SAVE POSITION BEFORE RUNNING EXPERIMENT
IF NUMBER OF POSITIONS > 1
Position slot
Saved X
Saved Y
Saved Z positions
Saved F
Saved P
Saved P-galv system offsets (microns)
Use current position when number of positions is 1
Number of positions
Save position
Move to Saved Position
Use current position only for stacks
Recover positions from last run
Take position values from Labview
PERMITS USING LABVIEW TO DIRECTLY CONTROL THE MICROSCOPE
AXES, IF YOU PREFER THIS TO USING THE CONTROLLER (I don't know why you would).
Update position
Take position values from controller
UNITS: MILLIMETERS
UNITS: MILLIMETERS
UNITS: MICRONS
X position
F position
Y position
Z position
P position
THESE AXES ARE
LIMITED TO REGION
OF SAFE TRAVEL
INCREMENTS FOR NON-PIEZO AXES
100 micron increments
INCREMENTS FOR PIEZO AXES
1 micron

The main module loads default states of variables, permits users to enter parameters for the image acquisition, permits turning laser excitation on and off for both colors and adjustment of laser power levels via the AOTF, and keeps track of all axes of positional information. Additionally, the main module permits executing various "test scans" which use much of the functionality of the microscope but do not acquire images. (These are used regularly for alignment, see below.) While in the main module, the user can choose between two positional modes: in the first, "Take position values from controller," positional information is constantly read in from the ASI controller and the Labview positional states matched to them as they are read in; in the second, "Take position values from controller," Labview will overwrite the existing internal states in the controller, thus positioning the microscope directly. Direct input of positional information is primarily useful for specialized purposes such as calibrations, or when some mistake is made and a previous known position needs to be recaptured exactly; for general purposes the controls on the controller are used.

User-definable parameters on the main page are (Figure 2.6): time per scan (ms, sets the frequency of the galvanometers and camera acquisition); scan width (in microns, describes the extent of beam movement); SPIM step size, the P distance to translate per slice; galvo only offset (microns), which permits moving the galvanometers independent of the piezo and is only used for calibrations; "image in red," "image in green," which tells the program which colors to use for the imaging; image height, image width, image vertical offset, image horizontal offset, which are piped to the camera to restrict the

capture window to a specified region of interest (ROI); "number of stacks," i.e. number of time points to acquire; "number of positions," number of X-Y positions; "number of slices," number of piezo P positions to acquire; "number of scans per slice," number of times to repeat each slice. The user can set a pause between each position acquisition, which I do in all experiments to permit any vibrations from stage movement to damp in between positions (I usually use 10 seconds); and interval between time points. The assumption is that the user will choose to approximately align the microscope to the central slice of the embryo. Therefore, the user is offered an option to specify an imaging offset from the current position, to start imaging at the top of the sample volume ("piezo and galvo system offset," which I usually set to around 20μm under normal operation).

While in the main module, the user can choose between two positional modes (Figure 2.7): in the first, "Take position values from controller," positional information is constantly read in from the ASI controller and the Labview positional states matched to them as they are read in; in the second, "Take position values from Labview," Labview will overwrite the existing internal states in the controller, thus positioning the microscope directly. Direct input of positional information is primarily useful for specialized purposes such as calibrations, or when some mistake is made and a previously established and recorded position needs to be recaptured exactly; for general purposes the controls on the controller are sufficient.

Several varieties of test scan are offered to the user (Figure 2.6), two of which are used always before every experiment and one of which is used semi-routinely. These are

all built using the basic architecture of the "main scan" program (see below), but much simplified and without camera integration, and with most of the scan parameters preset for specific uses. The first of these scans is the "flat fast scan", which produces a light sheet at the current position at and is used for finding embryos and aligning the galvanometers and P-axis. The second of these, "Test scan with Z motion" produces a light sheet that tracks slowly in the camera Z direction (i.e., piezo Paxis) to fill out the specified sample volume. It is used to verify that the embryo is correctly positioned in the imaging volume and alsogenerally to check alignment in particular, to check that the piezo and the beam are tracking one another correctly). The third, "slow test scan" produces a flat beam sweep at speeds a human eye can follow, and is intended for visualizing the beam in motion; this button is used to help focus the microscope if the alignment has been drastically changed for some reason (see also Appendix B). Test scan light sheets are produced at a typical imaging scan rate of 10ms per sweep (100 Hz), except for the slow scan which is at .5 Hz.

A user on the main module can communicate with the AOTF via simple toggle buttons, numerical inputs, and sliders permitting power level changes and shuttering (Figure 2.6). All information to the AOTF sent by both main module and main scan is sent in the form of serial commands (invisible to the user).

The main module continuously updates a parameter file on the disk which permits instantly rebooting the module into its last state. This is usually not required but can be helpful when communication with one of the electronic components fails for any reason,

requiring program restart. Failure almost never occurs except at the very start of imaging or while accessing the main module, and usually stems from issues with camera and/or galvanometer drivers (see Appendix B to this thesis). Instant rebooting permits easy redress of any issues.

This main module program is useable with no special background in Labview. I constructed it to be as user-friendly as possible, with the vast majority of options (for example, voltage calibrations, etc.) which are available to an experienced user suppressed for a routine user.

Main scan program

The "main scan" program is structured as a nested series of for loops over several variables: in order, stack number, position number, color number, slice number, and scan number. (The meaning of these terms is described above.) The main scan program coordinates camera operation, microscope stage operation, piezo P position, AOTF settings, and galvanometer positions. (It can be operated independently of the user-facing main module, but this is not recommended.)

The basic organization of the Main Scan program is as follows. A software timer is used to determine when the interval for a given time point (counting across all positions) has elapsed and the next is ready to be obtained. A second software timer introduces delays between positions. In a third loop, colors are switched, with a built in 50 ms software delay to provide time for the relevant color-switching serial command to

be read and implemented by the AOTF. At the start of acquisition at a new position, the camera is activated (by a software command) and primed to receive voltage signals. The camera is set to end an individual acquisition and begin the next based on receipt of a TTL (high) pulse. At the start of every slice, the camera receives its pulse, completing an image and beginning work on the next one. At the same time the piezo is sent a voltage signal which causes it to begin relocating to the next P position. The piezo has a settling time of approximately 10ms; there is an optional software delay at this point to give the piezo time to settle, which I used for slow moving samples (Chapter 3) and not for fast moving samples (Chapter 4). There is additionally a 2ms software delay per slice while Labview prepares to send signals to the electronic components. When the electronics have been signaled and requisite delays have elapsed, the galvanometers are given the cue to translate the laser beam to the next P position and begin generation of the next light sheet. The beam is typically held well away from the sample in between image acquisitions (typical scan width is 120 micrometers), to prevent accidental fluorescence generation and phototoxicity while imaging is not actively being conducted. Calculations involving imaging parameters, for example calculation of the correct voltage for a given piezo position, are done in real time in various positions in the program (these are obviously not computationally intensive). Additional aspects of program operation are discussed below.

Galvanometer sweeps are generated as triangle waves using analog output from a DAQ card, with galvanometer angular position linearly correlating to applied voltage.

The correct waves are generated computationally and output to the electronics within each slice's for loop. Because of the geometry at which the beams enter the back port on the microscope (Figure 2.2) – there is a 45 degree mirror built into the microscope to redirect horizontal laser light down into the excitation objective – the direction of the galvanometer sweeps does not correspond either to the camera X axis sweep or to the Y axis but approximately to a 50-50 linear combination of the two. Basic light sheet construction therefore involves a synchronous linear combination of both galvanometers to produce a sheet, followed by an orthogonal linear combination to produce the P direction of the sweep, which fills out the volume.

The full functionality of the AOTF, which permits microsecond scale control over the lasers, is not currently enabled. The AOTF as currently operated, via a pseudo-serial USB port, has a latency of 20-50 ms for color switching. This has not been a problem except in some cases where exact alignment of both colors within a given slice is more important than overall accuracy of a given stack within a single color (an embryo may move somewhat during the course of a single stack's acquisition, which will be exacerbated by acquiring both colors at the same time). For most imaging, switching color once at the end of a given stack (and incurring the 50ms latency just once) works well.

In our CMOS camera, the only pixel readout option is the "rolling shutter mode," in which pixels of the camera are read out sequentially line by line (some CMOS cameras offer a global shutter mode (Fossum, 1997)). An individual pixel can collect light

immediately before and after it is read out, but all light it collects after readout will belong to the subsequent frame of the line for example 20 rows below, until that line also reads out. Rolling shutter provides maximum speed of acquisition at the expense of asynchronicity between sections of the image, which is unacceptable in any rapidly moving sample. The main scan program therefore carries out a kind of simulated global shutter operation. Since the end of each exposure, beginning of next readout and beginning of the next exposure are synchronous and simultaneously triggered by a voltage pulse, a delay was added between the beginning of an exposure and the start of the beam sweep. The rolling readout for the previous exposure therefore runs down off the edge of the frame before the actual imaging begins. During this time the beam sits well off the edge of the embryo, as in all other lag periods, to prevent fluorescent light from being accumulated in the already read-out pixels. The length of this delay is calculated programmatically, and depends on both the vertical (i.e. the readout direction, i.e. camera Y) size and vertical position of the ROI in the sensor. For embryo work (almost all imaging done on the microscope has been of *C. elegans* embryos) I have always used a 500 pixel x 500 pixel ROI (81.25 μm x 81.25 μm), roughly centered in the overall camera frame. For this placement the delay is 2.7 - 3.7 ms across the range of typical Y positions.

The main scan program outputs formatted information about each microscope run: the exact time interval between each slice is calculated; the actual interval between stacks / time points is calculated; and all parameters and positions used in the imaging

run are saved to disk. All stacks are written immediately to disk (HGST Deskstar and Deskstar NAS HSDs) after both red and green channels are acquired.

Typical microscope operation

Some components of the microscope are not especially stable, in particular the angles of the top objectives can change substantially if they are brushed by a human hand (for example, when inserting or removing the sample chamber). Everyday imaging with the microscope therefore requires a (quick) alignment before beginning. This procedure is a simpler form of the more complicated one described above in the section on the microscope construction.

The typical procedure is as follows. The user lowers the top block of the microscope (F-axis) and looks to see the beam in the emission objective. For this purpose the Hamamatsu Live software provided with the camera is used, since just a simple camera readout is required , i.e. no synchronization with other hardware is needed. Provided the microscope is approximately aligned, and depending on the power of the laser, it should be clearly visible in the detection objective via scattering in the water, or through the higher intensity scattering in the coverglass as the beam waist is brought down through the glass (Figure 2.4). A 100ms exposure is typically sufficient for viewing the beam. The top objectives are lowered until the beam waist of the laser crosses the coverslip. The crossing point is visible in the top camera as a bright spot appearing to move up the scattered beam as the beam is brought down further into the

water. The bright spot is positioned using the F-axis control at the limit of the beam waist in the excitation axis direction, so that the full beam waist is sitting in the water just above the coverslip. The piezo axis is adjusted until the image of the scattered laser in the water comes into crisp focus.

This alignment is usually not quite accurate, and to correct it, at this point a fluorescent sample is needed. In order not to damage any of the embryos that would be used in imaging, often a "sacrificial" sample is used, usually an embryo that is not the right stage for the experiment that is to be conducted. The throwaway sample is first located in the underside objective and brought underneath the top objectives, bringing it into the common focus of the top objectives. The beam is scanned back and forth (the "flat fast scan") and the sample moved until it is positioned directly in the path of the beam. The middle of the embryo is brought to the position of the beam waist by moving the stage (since the beam waist sits just above the coverslip, this position must exist and be obtainable just by moving the stage). The microscope P axis is adjusted until the slice in the sample comes into best focus. The test Z scan and the piezo galvo control are then used to ensure that the whole sample is swept out.

Once the microscope is aligned to a sample, the region containing the sample is precisely delimited in the Hamamatsu software (cropped out of the overall region, usually about 300 x 200 pixels). The microscope can now be considered focused for that imaging window (for a given F, camera X, and camera Y). Subsequently, samples can be brought into good focus by moving them into this window -- i.e., by finding them in the

underside objective, approximately localizing them under the top objectives, then adjusting the F control and stage until the embryos are centered in the camera P, Y, X frame. As an optional final step, depending on the importance of exact focusing and the sample's resilience to phototoxicity, the microscope may be individually focused on each embryo by quickly scanning the 488 beam across it, adjusting the P axis until all nuclei come into best focus, and then cutting the beam off as quickly as possible.

Sample images

Many images taken with the microscope are shown in subsequent chapters of the thesis. Here I show a set of sample images, taken of an mCherry nuclear reporter using the 588 nm laser, to demonstrate the functionality of the microscope in imaging entire volumes (Figure 2.8). The microscope has a lateral resolution of approximately 400-500nm and an axial resolution of around 1.5μm, with the resolution primarily determined by the resolution of the detection objective (the beam is thicker than the depth of field of the objective).

Figure 2.8: Sample images taken with the SPIM microscope

Top: A side view maximum projection of a ball / bean stage embryo expressing a pan-nuclear histone reporter, taken with the SPIM microscope. The embryo is presented in its natural orientation in the microscope (the viewer is in the camera's position). Nuclei appear at their crispest in this position. Bottom: A maximum projection head view of the same embryo. Nuclei appear elongated in the Z axis because of the wider point spread function in the axial direction.

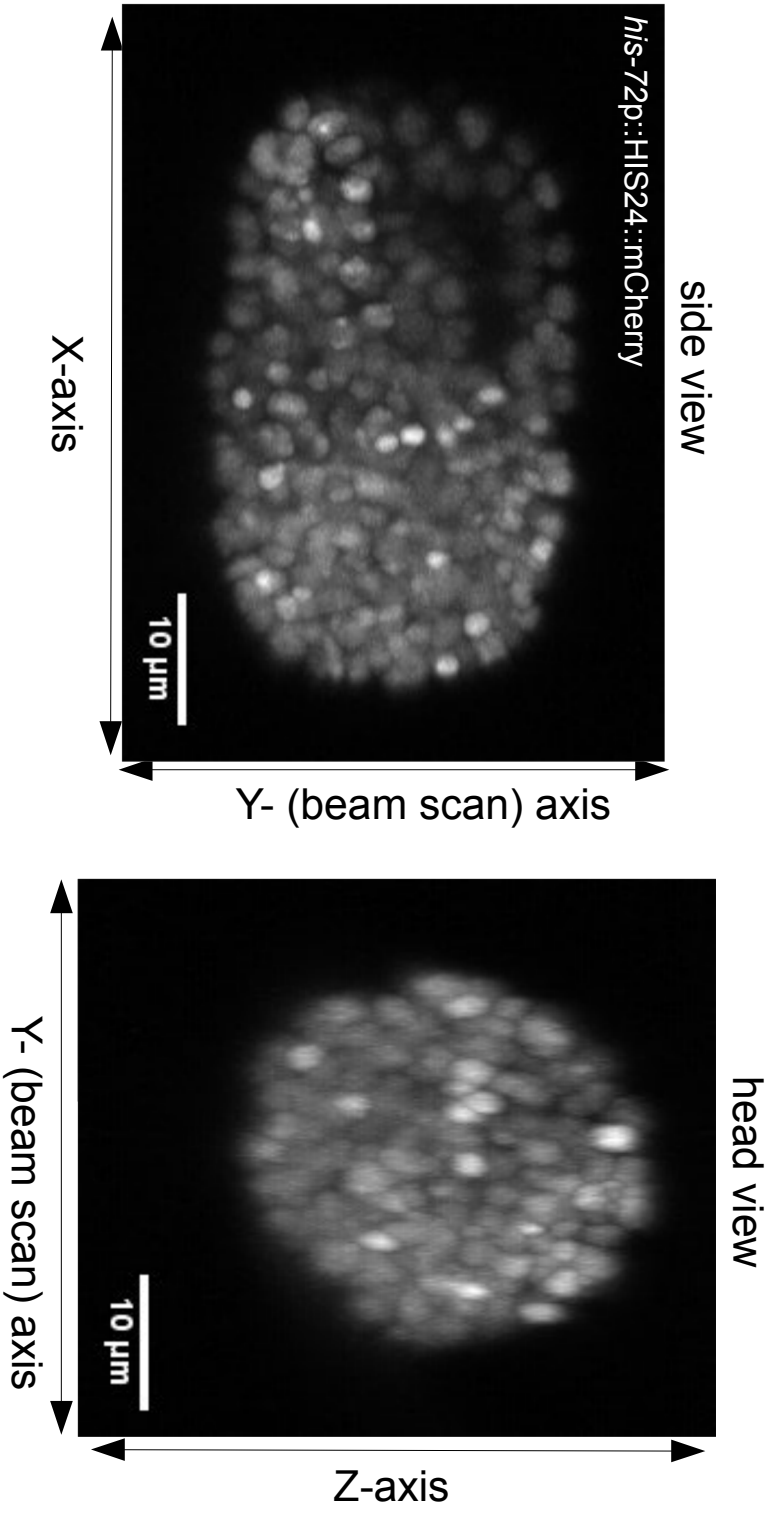
side view
his-72p::HIS24::mCherry
X-axis
10 µm
Y- (beam scan) axis
head view
Y- (beam scan) axis
10 µm
Z-axis

Additional design considerations

The reason for setting the system up with a laser-scanning mode of light sheet creation (e.g. DSLM, (Keller and Stelzer 2008), as opposed to forming the sheet through a cylindrical lens, was to allow ourselves the flexibility to pursue any of several possible resolution enhancing techniques. First, DSLM permits a structured illumination approach for improved contrast (Keller et al. 2010)**;** here the structured illumination is implemented by using the AOTF to modulate the beam power over the course of the scan. In principle, we can implement this modality at any time by making slight wiring and software modifications (i.e., without moving any optical components). DSLM also permits a single plane illumination confocal microscopy approach (Silvestri, Bria et al. 2012), with the aim of improving contrast or improving axial resolution. We are unlikely to pursue this strategy, since it sounds difficult to implement while perhaps affording minimal gains. Finally, DSLM can be easily modified to sweep Bessel beams instead of Gaussian beams, which, when used in conjunction with structured illumination, may lead to very large improvements in lateral and axial resolution (Planchon, Gao et al. 2011, Gao, Shao et al. 2012).

Wu et al (2011) employed an EMCCD camera, which permitted them to take beautiful high quality images at very low levels of light intensity (they report using only 5 uW of power for their nuclear GFP imaging). EMCCD cameras differ from conventional CCD cameras in that they have a built-in gain on the camera chip preceding

the read-out phase, which can be increased to essentially eliminate camera read noise (Buchin, 2011), thus greatly increasing camera fidelity in the low light regime in which camera read noise can dominate total recorded electrons from the camera. However, at the time that I was building my SPIM microscope, EMCCD cameras were limited to around 35 frames per second, which rendered them less attractive than the sCMOS cameras which permit >100 frames per second imaging. Wu et al see non-trivial levels of blurring as a result of the slower speeds permitted for an EMCCD camera, as opposed to a CMOS. Additionally, the large pixel size of EMCCD cameras makes imaging somewhat more difficult and rules out certain speed enhancing measures which we thought we might employ, such as tiling images across a camera sensor during one exposure (Planchon et al, 2011). Finally, there is a large (~$10,000 at the time I was building the microscope) cost difference between sCMOS and EMCCD cameras. Since I built the microscope, faster EMCCD cameras have come into existence which might be worth a second look from a person building a similar microscope system now. In actual practice, and as will be described below, I did not find it necessary to use the full speed of our CMOS camera and the microscope generally was operated in the 25-35 ms per frame speed range (1.5 - 7 seconds per volume).

The microscope was specifically built to work with the mCherry fluorophore, with a non-traditional choice of a 588nm laser as opposed to the 561nm laser typically used for red excitation. The excitation maximum of mCherry is 587nm, while the excitation maximum of traditional RFP is 555nm and DsRed is 554nm**.** As mCherry is

increasingly used instead of RFP, because of its substantially greater photostability and brightness (Shaner et al, 2005), the choice was made to select a laser specifically for mCherry work instead of accepting the 36% loss of excitation efficiency attendant on exciting mCherry using 561nm radiation. This has the effect of preventing us from working with some legacy strains using RFP, such as some of the histone-labeled strains constructed in the Waterston group. The Caenorhabditis Genetics Consortium – CGC – currently holds 178 transgenic worm strains containing RFP, 91 containing DSRED, and 450 containing mCherry. The choice was not unreasonable, but the inability to work with certain strains could be a substantial disadvantage and a 561nm laser would probably have been preferable in hindsight.

Chapter 3: Alignment of Embryos for Visualization and Analysis of Nerve Ring and Associated Neuron Positioning

Introduction

One of the principle motivations of building the SPIM microscope was to be able to image nervous system development in vivo at good temporal resolution. Although the primary use case of the microscope must be imaging the rapidly moving embryos post-twitching, the expanded light budget under SPIM means it can also be used to generate high contrast, high slice density images of earlier embryos with minimal photodamage.

I used the SPIM microscope to study the temporal and positional development of the *C. elegans* nerve ring using fluorescently labeled sublateral neurons as a proxy for nerve ring structure, generating quantitative positional information that could be used to determine intrinsic differences between animals.

I developed a method for aligning embryos both temporally and spatially up until the beginning of twitching, the start of the rapid movements which characterize the two- and threefold stages of embryogenesis, using a pan-nuclear marker for sizing, orienting, and staging embryos, as well as an automated segmentation and point set registration method, operating on a sparsely expressed nuclear marker, for governing rotations and translations between time points. All transformations were globally rigid, up to scaling, the idea being to preserve intact the local geometry and observe differences that might

have been obscured by a locally freer alignment method such as thin plate splines. The nuclei we used for alignment were mostly distributed around the head, permitting an alignment of the whole head region without reference to the position of individual sublateral cell bodies or of the nerve ring itself.

Using my method, I measured the positions and angular configurations of the nerve rings of 31 embryos which had been registered by the algorithm (of 34 total), finding that the sublateral cell bodies sending axons to the nerve ring are loosely positioned to a precision of several micrometers while the neurites of the nerve ring are positioned with ~1 micron precision. The ALA neuron, which is also labeled by our marker and towards which the growing neurites appear to converge, is positioned with similar precision to the neurites.

Using the same set of fluorescent markers as for the wild type case, I also imaged nerve ring development in a strain with a known nerve-ring positioning mutation, *cam-1(gm122)*. *cam-1* is a ROR homolog which has been implicated in nerve ring positioning defects (see introduction). Attempts to align the *cam-1* dataset with my alignment algorithm were only partially successful, presumably because of weak expression in the *unc-130* nuclei. However, we were able to deduce information about the anterior-posterior positioning of a subset of the animals, showing that the anterior placement defect previously observed for *cam-1* does not take effect before twitching. We suggest that it is therefore more properly involved in maintenance of position than in initial

positioning. Additional *cam-1* defects were observed which have not been previously described, suggesting a secondary role for the gene in initial nerve ring positioning.

Results

I collected for imaging 34 embryos from the OS10584 strain, which expresses a *his-72* driven pan-nuclear mCherry marker, visible from around the 50 cell stage, a sparsely labeling *unc-130*::GFP nuclear marker, used for alignments, and a *ceh-17*::GFP reporter, which labels a subset of sublateral neurons and the ALA neuron (Materials and Methods; Figure 3.1).

The mCherry marker was introduced as a means of monitoring division timing in the early embryo, in order to build up an overall clock of embryonic timing, and, additionally, as a means of measuring the overall shape of the embryo. *unc-130* was introduced as a marker for alignments; it was initially identified by Anupriya Singhal in our lab as a possible control point marker because of its sparse expression and asymmetric distribution in the early embryo. *unc-130* is predominantly expressed in the anterior half of the embryo, having nevertheless several nuclei located on the posterior side of the embryo at the ball stage which subsequently migrate to the tip of the tail. It is distributed around the head at all stages until twitching, so that alignments based on average *unc-130* position essentially account for movements of the entire head. Here, it is used in a set of point set registration techniques and in several alignment heuristics.

Figure 3.1: Overview of markers used in the alignments strain

Shown is an overview of fluorescent markers used for alignment and visualization of the nerve ring and sublateral cell bodies in OS10584. Images are processed with a gamma adjustment to permit easier visualization of all markers simultaneously. First row: GFP channel. Fluorescence is expressed in sublateral cell bodies and neurites (*ceh-17*::GFP) as well as in *unc-130::*GFP labeled nuclei. Early: sublateral neuron precursors and *unc-130* nuclei can be difficult to distinguish at this stage. *Unc-130* nuclei are predominantly located in the head with several nuclei extending into the back part of the embryo. Pre-rotation: sublateral cell bodies can be distinguished, with no neurite outgrowth as yet. The *unc-130* nuclei have distributed themselves around the head and are becoming more difficult to discern elsewhere. The embryo is still approximately in the same overall configuration as in the early time point. Mid-rotation: embryos undergo a rotation about their main axis during the course of embryogenesis, which is of varying size and even direction, with the exact timing inconsistent between embryos. This embryo has rotated about halfway to its final position at the time point shown here. The axons are beginning to grow out from the sublateral cell bodies. Neurite outgrowth: rotation is complete in this embryo and the neurites of the nerve ring are growing out towards the position of the ALA neuron (which has itself recently been migrating, in this embryo). Nerve ring formed: the sublateral neurons wrap around the pharynx at least to the ALA neuron, and perhaps beyond. This is the last stack before twitching in this embryo. Second row: mCherry channel for this embryo shows development from ball (early), to bean (pre-rotation), to comma (mid-rotation and neurite outgrowth), to 1.5-fold (nerve ring formed). Third row: Overlay of mCherry and GFP channels. Fourth row: Model of movement and development over time of important fluorescently labeled objects in the embryo. All mCherry nuclear centers are plotted based on a Starry Nite segmentation. *unc-130* nuclei, sublateral cell bodies, nerve ring neurites, and the ALA neuron are modeled based on positions sketched from the first row of images in this figure.

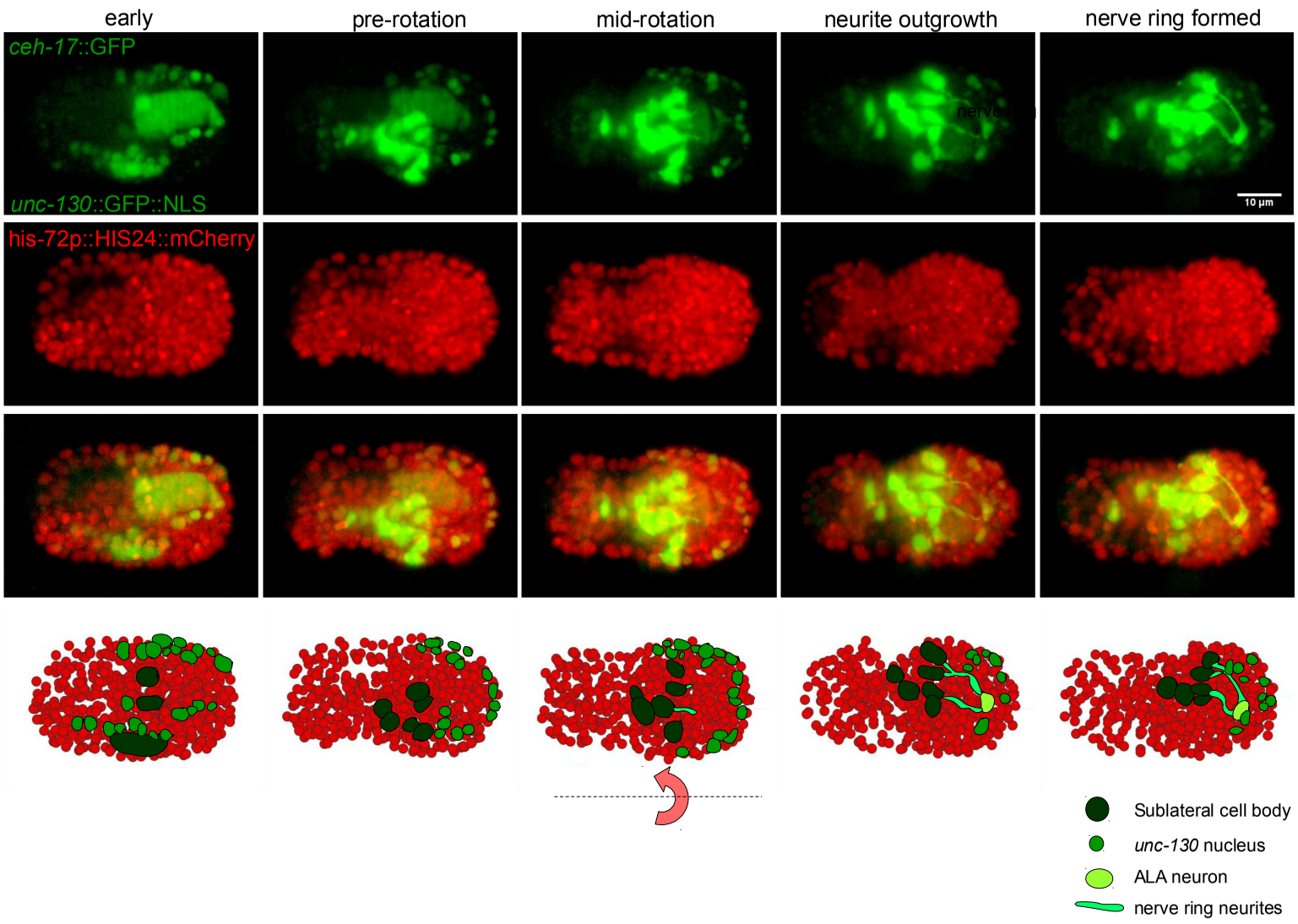
early
pre-rotation
mid-rotation
neurite outgrowth
nerve ring formed
ceh-17::GFP
unc-130::GFP::NLS
his-72p::HIS24::mCherry
10 µm
Sublateral cell body
unc-130 nucleus
ALA neuron
nerve ring neurites

Embryos were staged to within approximately an hour, between one and six cell stages (Materials and Methods). After a two hour wait period, which was enough time for the pan-nuclear mCherry marker to become visible in all embryos, embryos were imaged every 10 minutes for 20 stacks, leading from approximately the 100 cell stage until ball, followed by fast imaging every 2 minutes for 125 stacks, which brought the imaging into at least the two-fold stage in every case. The initial slow pace of the imaging was intended to minimize light exposure of the samples while generating a timeline of nuclear divisions that could be used for synchronizing different embryos for analysis (see below). The faster imaging covered the period of greater interest immediately before and during nerve ring development.

All embryos were initially positioned with their anterior-posterior axes within 45 degrees of the perpendicular to the excitation objective (Materials and Methods), to reduce spread of the Gaussian beam across the width of the embryo. This initial anterior-posterior axis is maintained until twitching. Since the embryos are uncompressed in the SPIM setup, they were initially configured about their A-P axes in an arbitrary dorsal-ventral and left-right position, in contrast to a conventional microscope in which embryos are compressed by the coverslip into one of several defined orientations (Richards et al., 2013).

In looking over the datasets I quickly realized that a single global transformation would not suffice to align the embryos across all time points, since embryos in their raw time courses were seen to undergo widely divergent bulk movements during the course of

morphogenesis and nerve ring outgrowth, most notably a developmental rotation about the anterior-posterior axis which varies in magnitude and direction between animals. I therefore developed a multi-stage positional alignment system, in which embryos are first aligned by center of mass at the origin and corrected for differences in timing, then aligned to the X-axis of imaging, then corrected for bulk rotations, then lastly directly aligned to a specially chosen reference embryo.

The "reference embryo" was corrected for internal movements in a similar way to the rest of the embryos, which were termed "test embryos." The reference embryo was selected from among the others for being positioned with its long axis very nearly perpendicular to the detection objective, with nerve ring outgrowth clearly visible in its raw orientation (as seen in Figure 3.1); and for having been followed through to hatching, demonstrating that its development was largely normal. The final orientation of the head of the reference embryo just before twitching is partway between its right and dorsal sides facing the camera with anterior to the right.

Segmentation

In order to align the embryos, it was necessary first to segment the 4D image sequences to generate positional maps of the different markers involved. The mCherry nuclear positions, which were used to establish overall embryonic shape and timing, were relatively easy to establish, while the *unc-130*::GFP marker and the *ceh-17*::GFP neurites and cell bodies shared a fluorophore and required more effort to distinguish.

To extract temporal and positional information from the pan-nuclear red channel, we turned to the Starry Nite program (Bao et al., 2006; Santella et al., 2010; Materials and Methods), designed in part for segmenting *C. elegans* embryonic nuclei. By conservative tuning of the parameters, we were able to automatically generate a list of nuclear centers for the first forty time points of each embryo, without the usual manual curation. Our parameter tuning was designed to eliminate false positives, while still retaining accurate bulk information about nuclear number and positions.

The green channel segmentation contained three main types of features that could be extracted—the *unc-130* nuclei, *ceh-17* neuronal cell bodies, and *ceh-17* neurites, in particular the axon bundles growing into the nerve ring (other axons connecting sublateral cell bodies are occasionally observed). Attempts to segment using simple criteria like overall brightness failed to separate neurites and nuclei, which have similar intensity, but are effective at extracting cell bodies (see below).

Using the machine-learning based segmentation program Ilastik (Sommer et al., 2011; Materials and Methods), we were able to train a classifier which could distinguish between our three types of features (Figure 3.2). The classifier was trained on five of the embryos, one of which was the reference embryo, with four time points per embryo that were evenly spaced throughout the course of the fast imaging until twitching.

Figure 3.2: Ilastik segmentation of *unc-130* and *ceh-17* labeled objects

Example results from using the Ilastik segmenter on the OS10584 strain. White arrow: false negative. Orange arrow: False positive. **A:** Segmentation is shown at the first fast imaging time point for an arbitrary embryo that was not used for training the segmenter. Top row: GFP alone. Middle row: Segmentation results from the three segmentation channels, *unc-130*, c*eh-17* sublateral cell bodies, and *ceh-17* sublateral neurites. Here, and for most purposes, *unc-130* nuclei are further processed, and truncated halfway along the A-P axis in order to confine segmentation to the head (dotted yellow line; see main text). Cell body segmentation is highly inaccurate at this stage because of the similar brightness and morphology of cell bodies and *unc-130* nuclei. The segmenter correctly describes no neurite segmentation at this early stage. Third row: Merge of segmentation results and GFP channel. **B:** Segmentation is shown in the same embryo as in A, at the last time point before twitching. Top row: GFP alone. Middle row: Segmentation results from the three segmentation channels, *unc-130*, *ceh-17* cell bodies, and *ceh-17* neurites. *unc-130* nuclei are further processed as in A. *unc-130* nuclear segmentation and cell body segmentation are highly accurate at this stage, with neurite segmentation the least accurate of the three, but still sufficient for getting a sense of the shape of the nerve ring. Third row: Merge of segmentation results and GFP channel. (*continued*)

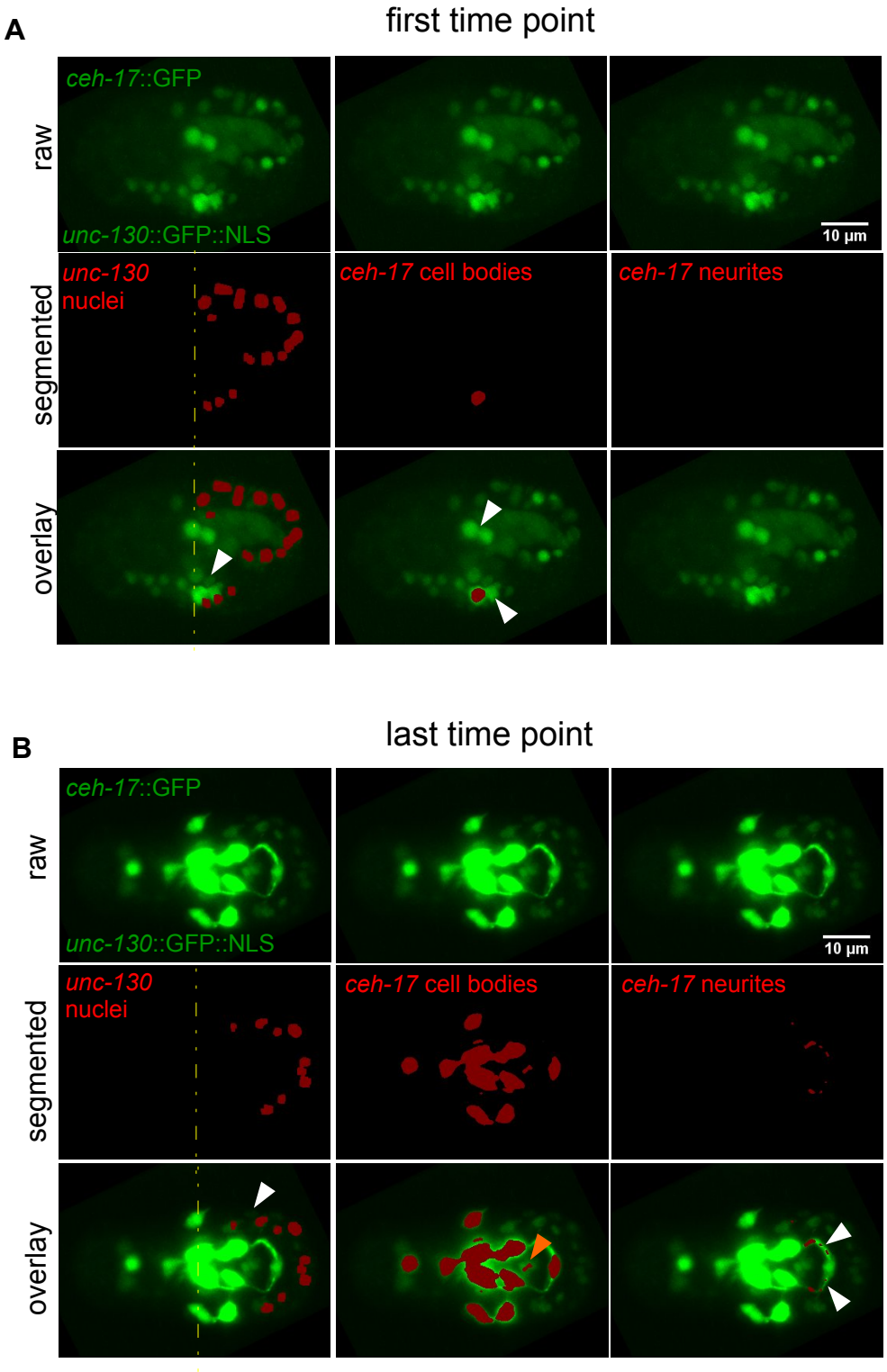
A
first time point
raw
segmented
overlay
ceh-17::GFP
unc-130::GFP::NLS
10 µm
unc-130 nuclei
ceh-17 cell bodies
ceh-17 neurites
B
last time point
raw
segmented
overlay
ceh-17::GFP
unc-130::GFP::NLS
10 µm
unc-130 nuclei
ceh-17 cell bodies
ceh-17 neurites

Figure 3.2 *continued*. **C:** Checking Ilastik segmentation at last time points for neurites and cell bodies, using the "pixels within 1 micrometer" method described in the text. For each pixel in an image stack in the first set, the program looks for pixels in a corresponding image stack in the second set that are within 1 micrometer of that pixel; if a pixel is found, the program scores a match. The proportion reported is across all pixels in all embryos, with standard deviation calculated across embryos. The neurite segmentation channel for the last time point is compared to a manual trace. The cell body segmentation is compared to a simple filter which extracts all pixels above 500 counts. Forward and backward match percentages are provided. Error bars are S.D. across embryos. **D:** The false positive rate in nuclear segmentation was calculated by hand using 90 time points from random embryos, distributed throughout embryogenesis. 13 false positives were recorded out of 1213 nuclei counted by the full nuclear segmentation procedure (see text). **E:** Nuclear counts per time point across all time points, recorded using the full segmentation procedure for *unc-130*. The minimum count across all time points is 6 nuclei, while the maximum (which is in fact the maximum permitted by the software) is 17. Error bar is S.D. across time points.

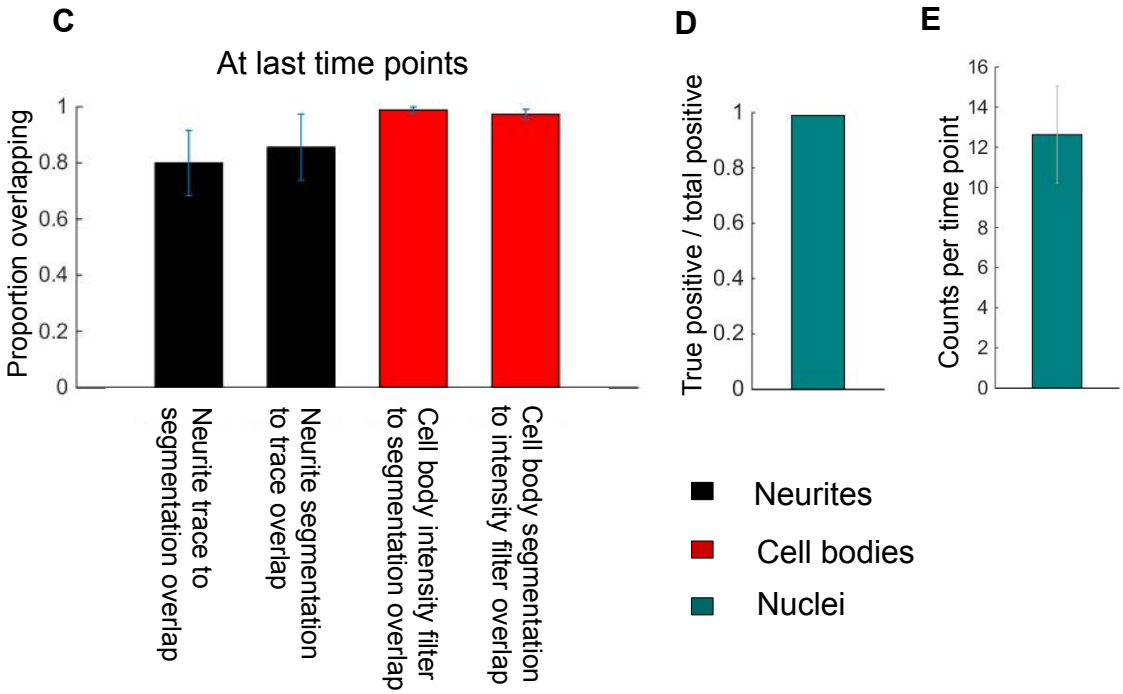
C
At last time points
Proportion overlapping
1
0.8
0.6
0.4
0.2
0
Neurite trace to segmentation overlap
Neurite segmentation to trace overlap
Cell body intensity filter to segmentation overlap
Cell body segmentation to intensity filter overlap
D
True positive / total positive
1
0.8
0.6
0.4
0.2
0
E
Counts per time point
16
14
12
10
8
6
4
2
0
Neurites
Cell bodies
Nuclei

Because we wanted to use the *unc-130* nuclear segmentations generated in Ilastik as an independent tool for establishing absolute position of neurites and cell bodies, it was extremely important that very few neurite or cell body pixels be incorrectly labeled as nuclear. By conservatively designing the segmenter, such that many pixels that really pertained to neurites or nuclei were incorrectly segmented as background, and thus increasing the false negative count, I was largely successful in eliminating false-positive labeling (Figure 3.2).

The base *unc-130* segmentation was only used for anterior-direction identification and first time point inter-embryonic alignment (see below). For all other purposes, the base nuclear segmentation in Ilastik was improved upon in several stages. First, I generated well-defined nuclear objects from the original pixelated labeling using a simple Gaussian blurring operation (2 pixels, or 325 nm, on a side); second, I restricted the segmented nuclei to the anterior half of the embryo, since in later stages the posterior end (now a defined tail) and the anterior end (now a defined head) moved independently, and only the movements of the head (containing the nerve ring) were of interest for the project; third, I "cored" the anterior half of the embryo using a cylinder of defined size to prevent any off-target labeling of the nerve ring and the ALA neuron; fourth, I restricted the program to the objects likeliest to be nuclei by first finding the 5 largest objects (calculated by number of labeled voxels) output by the program, and then permitting it to find up to 12 more objects based on an intensity threshold dynamically calculated from the brightnesses for the 5 largest objects.

I manually checked the nuclear segmentation for false positives across 12 embryos taken at random from among those not used to train the segmenter, two from each day of imaging. A total of 90 time points were examined, evenly distributed through the fast imaging segment for each embryo. 1213 nuclear objects were segmented across all time points, of which 1200 (98.9%) were determined by eye to be real *unc-130* nuclei. Of the remaining 13 objects, 5 were incorrectly labeled sublateral cell bodies (all but one of these in the first ten stacks of a given embryo, when some of the sublateral cell bodies look identical even by eye to *unc-130* nuclei, and can only be distinguished by moving forward in a movie to determine their subsequent development); one was an incorrectly labeled ALA neuron, which extended out beyond the coring cylinder in this embryo; two were contamination outside the embryo labeled as nuclei; one was a neurite; the remaining five were blurry and / or dim and their identity as nuclei or other objects could not be determined. The minimum number of objects found for any time point was 7, with the average being 12.3 objects. (Three is, theoretically speaking, the number required to map one image stack onto another, although in practice more than this is beneficial.)

Cell bodies are inaccurately segmented at early time points, but segmented with excellent accuracy at late time points when the problem becomes easy, as intensity of the cell bodies differs dramatically from that of the other objects in the image (cell bodies are typically 10-15 times brighter at late time points than neurites and nuclei). The effect of the Ilastik segmentation for cell bodies at late time points can largely be replicated with a

simple filter which extracts all objects with recorded intensities at the camera above 500 counts (Figure 3.2), for the laser intensities and exposure times described in Materials and Methods. Neurite segmentation was found to be largely consistent at the last time point with manual tracing (Figure 3.2) but is inaccurate at intermediate time points when neurites are dim (not shown).

Temporal alignment of embryos

Having segmented the embryos, the last step before conducting the positional alignments was to align the embryos in time (Figure 3.3).

Figure 3.3: Temporal alignments of embryos

A: Top: A test embryo is matched in time against the reference embryo using mCherry nuclear counts from 20 time points. Time intervals are interpolated by a factor of five, to every 2 minutes, to provide greater resolution in the calculation. A time-axis offset is calculated by minimizing the summed square errors across all time points between the embryos. The resulting time courses appear matched by eye. Bottom: all time points (various colors) are shown matched to the reference embryo (thick green line). **B:** All embryos were scored for time of onset of twitching, the first jerking movement visible during the course of development with the 2 minute interval imaging. Standard deviations of twitching times are substantially reduced using the time matching ($p < 10^{-6}$, *F-test* of equality of variance), proving both that the time matching is effective and also that twitching is a precisely timed developmental time point.

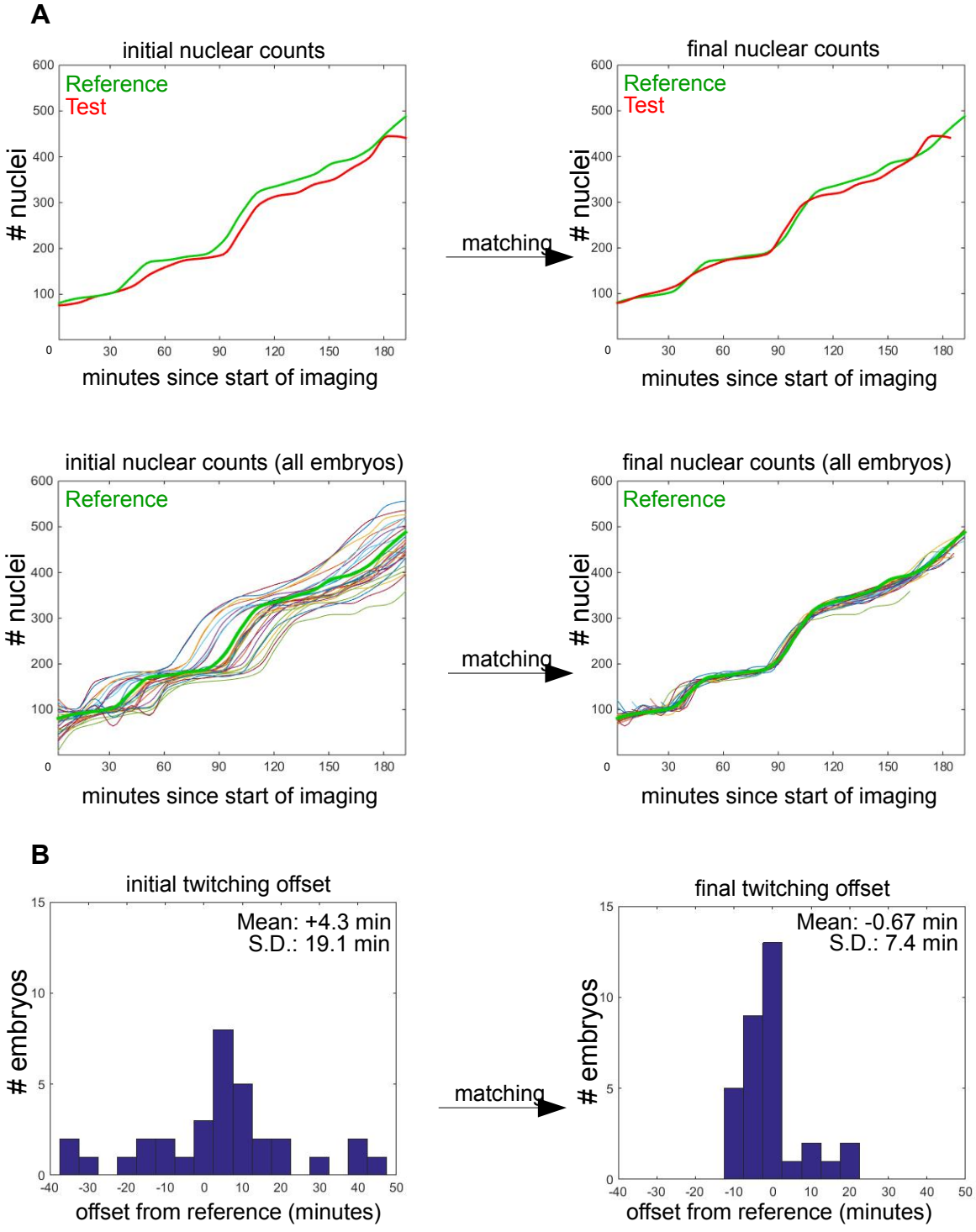
A
initial nuclear counts
Reference
Test
nuclei
minutes since start of imaging
matching
final nuclear counts
Reference
Test
nuclei
minutes since start of imaging
initial nuclear counts (all embryos)
Reference
nuclei
minutes since start of imaging
matching
final nuclear counts (all embryos)
Reference
nuclei
minutes since start of imaging
B
initial twitching offset
Mean: +4.3 min
S.D.: 19.1 min
embryos
offset from reference (minutes)
matching
final twitching offset
Mean: -0.67 min
S.D.: 7.4 min
embryos
offset from reference (minutes)

I used the time course of the nuclear divisions generated by Starry Nite to stage the embryos more precisely than was accomplished at sample preparation. First, total nuclear numbers per embryo over the first 20 frames (200 minutes) were extracted from the Starry Nite data and interpolated to 2 minute intervals using the PCHIP (Piecewise Cubic Hermite Polynomial) method in Matlab (similar to splines, but not necessarily differentiable, with better local behavior; Burden and Faires, 2004). Next, all test embryo cell count graphs were matched onto the reference embryo graph by a simple linear offset on the time axis, with the offset chosen to minimize the summed square difference on the nuclear number axis across all time points. The resulting time courses display very similar characteristics by eye, suggesting that further temporal adjustment such as a linear scaling (Bao et al., 2008) was unnecessary. 9 offsets were positive (meaning embryos were younger than the reference), while the remaining 22 were negative. The mean offset calculated by the method across all embryos was -5.0 minutes. The reference embryo was therefore younger than the mean embryo, but not by very much.

To independently test that the temporal alignment method was working as intended, I timed the onset of twitching in each embryo (Figure 3.3). Twitching was defined here as the first non-continuous movement of the embryos visible during the course of imaging; the movements of twitching are abrupt and obvious enough that this point could always be defined without ambiguity. While the standard deviation in twitching times prior to instituting the time correction was 19.1 minutes, the deviation in twitching times after the correction is 7.4 minutes, indicating a substantial tightening of

the distribution. This result demonstrates both that our system for temporal alignment is quite precise and also that twitching is an exactly defined developmental time point.

Generating a coordinate system for each embryo

With embryonic timing established, I sought to generate global coordinate systems for each embryo in which coordinates of the cell bodies and neurites could be fixed. Embryos had to be centered and initial A-P axes aligned. Bulk movements of the embryo during the course of embryogenesis had to be identified and undone. Substantial rotations about the anterior-posterior axis which occurred during ball, bean, comma, and into 1.5-fold stages were identified as the most significant movements and the alignment system tailored to correct these. These and subsequent alignment steps are summarized in Figure 3.4.

Figure 3.4: Overview of positional alignment algorithm

The steps of the alignment algorithm are broken down into two components. In the first set of procedures (left), a coordinate system is generated for all time points of an individual embryo. Embryos are first aligned to the X-axis using a convex hull method operating on the mCherry nuclear positions; then the head is identified by preponderance of *unc-130*; then developmental rotations are determined and unwound for subsequent time points based on location of *unc-130* nuclei in the head. The reference embryo coordinate system is also generated in this way, with, however, all time points wound forward to the last time point instead of backward to the first. In the second set of procedures (right), the individual embryonic coordinate systems are mapped to the reference embryo coordinate system through a series of individual steps. First, the test embryos are scaled to match the reference embryo. Second, the initial DV-LR angle is estimated from measuring the vector between the posterior-most nuclei and the anterior nuclei at a defined time point. Third, the earliest time point in a given sequence is mapped to a reference embryo from its already nearly aligned position (based on prior identification of AP-axis, centering, and estimation of DV-LR angle). Fourth, at this point time sequences are approximately aligned based on the sum of transforms calculated to this step (indirect alignment). Fifth, a correction step directly mapping between time points in test and reference embryo sequences is instituted.

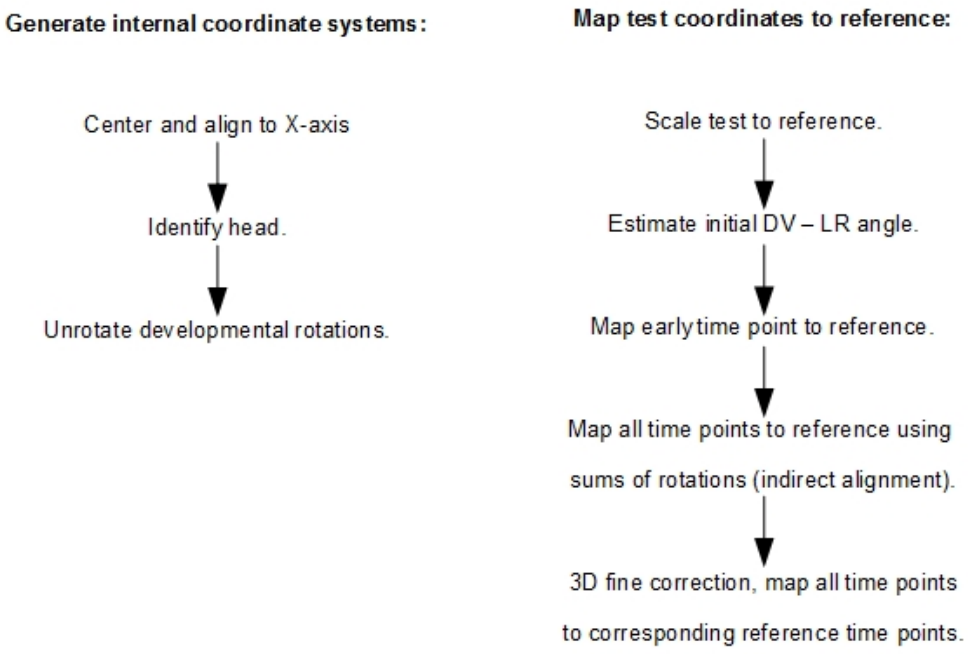
Generate internal coordinate systems:
Center and align to X-axis
Identify head.
Unrotate developmental rotations.
Map test coordinates to reference:
Scale test to reference.
Estimate initial DV – LR angle.
Map early time point to reference.
Map all time points to reference using sums of rotations (indirect alignment).
3D fine correction, map all time points to corresponding reference time points.

Our first step was to computationally place embryos at the center of the image frame with the anterior-posterior axis aligned to the X-axis. *C. elegans* embryos are encased in a hard eggshell and maintain their center position and anterior-posterior axis until twitching; therefore, embryos which are aligned at an early time point will remain partially aligned for subsequent time points. We aligned the embryos based on their overall shape at the ball stage, during which the embryo approximately fills out its eggshell. We used the positions of the nuclei on the surface of the embryo as an indicator of embryonic shape.

For a given embryo at a given time point in ball stage, I took the convex hull (Weissstein, n.d.) of all nuclear centers, filled the space computationally to a uniform density, and calculated the moments of inertia and centroids of the resulting distribution (Figure 3.5). The axis corresponding to the largest principle moment was placed along the X-axis. As the calculated directions of the second and third principle moments of the embryos were not consistent over time, as indeed would be expected for an embryo displaying approximate rotational symmetry, up to noise, about the main axis, the directions of the second and third axes were left randomized at this stage. Additionally, as the moments of inertia calculation gave no information about which was the anterior and which the posterior end of the embryo, anterior-posterior orientation on the X axis was at first randomized. I chose this method over the related minimum volume ellipsoid method previously employed for *C. elegans* embryos (Richards et al., 2013), since the minimum volume ellipsoids did not seem to accurately fit the embryonic shape, with the

ends of the ellipsoids extending substantially past the first and last nuclei on the A-P axis. (Embryos have a "snub nose" compared to ellipsoids.)

The results of the procedure were averaged over approximately fifteen time points per embryo, with the exact number depending on the particular temporal offset calculated for that embryo, such that the overall temporal range over which averaging was done remained constant. Centroid positions were directly averaged to produce a mean centroid position for each embryo. Rotations cannot, in general, be averaged; however, a reasonable notion of rotational averaging exists for rotations deviating by small amounts from each other (<~20 degrees), as indeed is the case for these repeat measurements (Gramkow, 2001). I generated an average rotation by converting the rotation matrix of principle axes to quaternions (Weisstein, n.d.) directly averaging, and normalizing, a procedure which produces smaller errors than other such methods (Gramkow, 2001)

Figure 3.5: Alignment of embryo to A-P axis

A: The convex hull is taken of the Starry Nite segmentation of mCherry nuclear centers. The longest principle moment (orange axis) is determined using a moments of inertia calculation, and aligned to X. **B:** The anterior end of the embryo is identified by the greater density of raw *unc-130* segmentation in that region as opposed to the posterior.

A

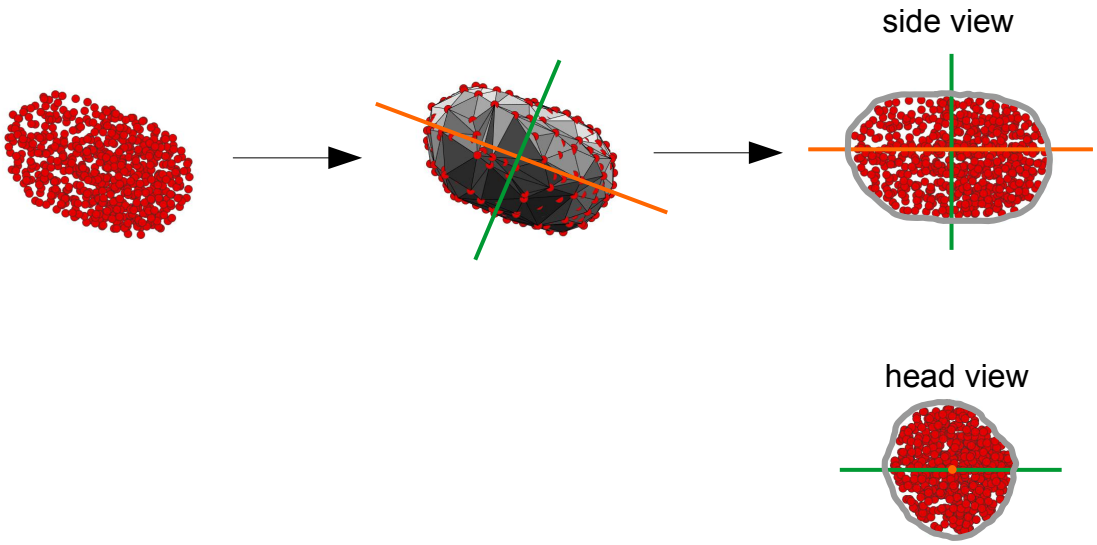
side view
head view

B

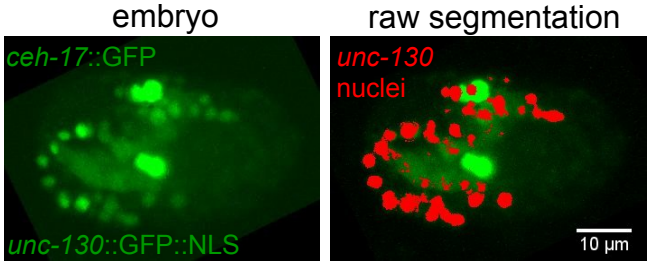
embryo
raw segmentation
ceh-17::GFP
unc-130::GFP::NLS
unc-130
nuclei
10 µm

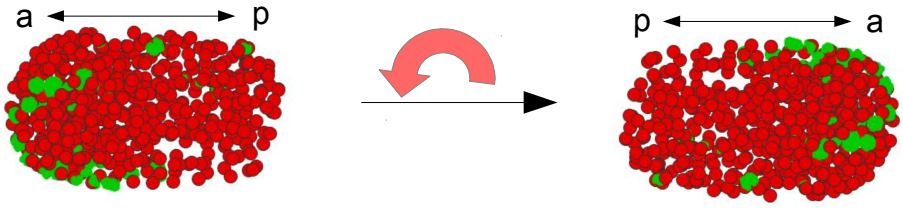
a
p
p
a

With the embryo placed at the center of the frame and its A-P axis coincident with the X-axis, I used the *unc-130* segmentation to identify its anterior and align it to +X. Taking a time point from early in the 2 minute interval of imaging (ball / bean stage), and noting that *unc-130* expression was much stronger in the anterior half of the animal (Figure 3.5), a simple module of the alignment algorithm checks whether the average position of nuclear pixels segmented by Ilastik is to the left or the right of the overall embryo center in the initial configuration, flipping the embryo to bring the side with greater density of nuclei to the +X side if necessary.

Unrotating developmental rotations

The *unc-130* nuclear segmentation, although variable between embryos, was broadly consistent between neighboring time points of the same embryo. I therefore sought to use the *unc-130* segmentation results as inputs in a point set registration method for eliminating rotations between neighboring time points. With neighboring time points rotationally aligned, all rotations could be unwound to the first time point or wound forward to the last time point by summing or subtracting the intervening rotations. The first procedure (winding back to the first time point) was followed for test embryos and the second procedure (winding forward to the last time point) for the reference embryo (Figure 3.6).

Figure 3.6: Unrotating developmental rotations by matching nearest time points

unc-130 segmentation from neighboring time points in a single embryo is used to match these time points to one another, using the Coherent Point Drift (CPD) registration program. **A**. Representation of neighboring time points in the same head view. **B**. Before: overlay of initial segmentation data from the two time points. After: overlay after matching. Individual rotations between time points tend to be very small, as shown here (actual data are presented). The sum of rotations can be calculated and used to unwind all rotations to this point (represented here by Θ_n), or to wind rotations forward towards the last time point, as is done for the reference. **C**. A reference embryo time point ("pre-rotation" from Figure 3.1) is rotated to the DV-LR angle of its last time point (78 minutes forward), using the approach described in B.

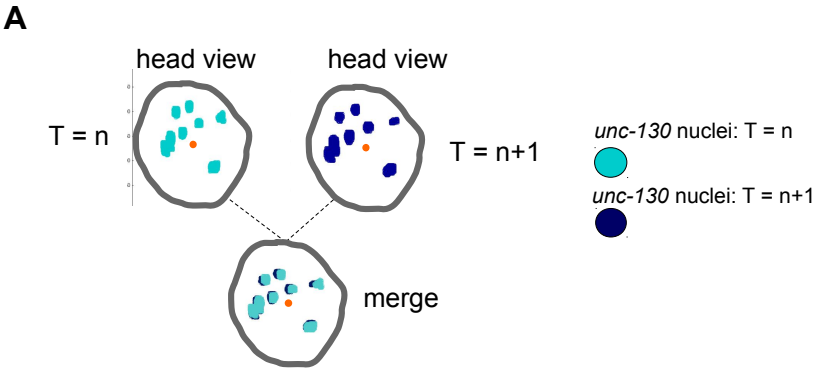
A
head view
head view
T = n
T = n+1
merge
unc-130 nuclei: T = n
unc-130 nuclei: T = n+1

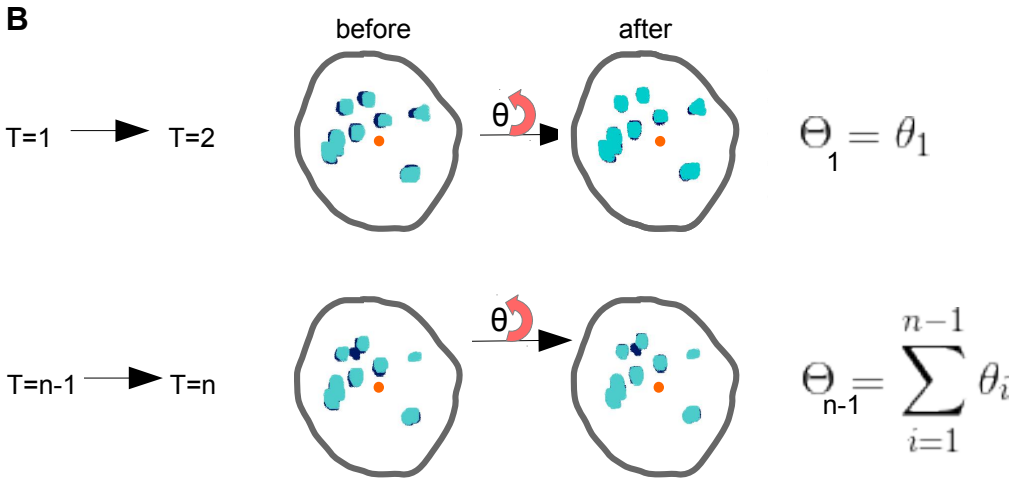
B
before
after
T=1
T=2
θ
$\Theta_1 = \theta_1$
T=n-1
T=n
θ
$\Theta_{n-1} = \sum_{i=1}^{n-1} \theta_i$

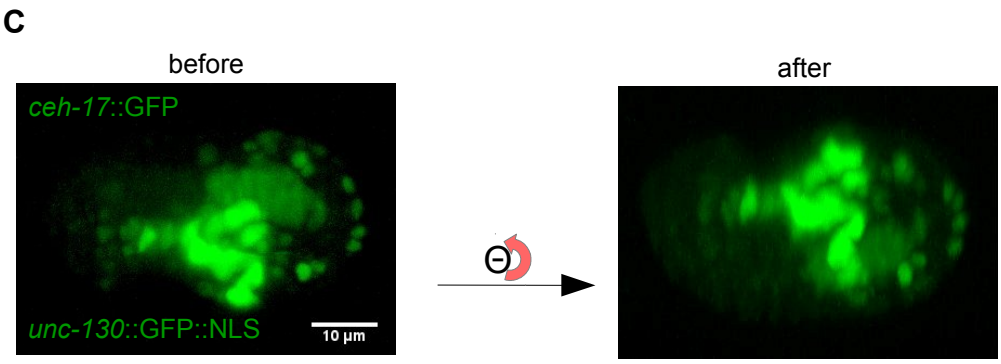
C
before
after
ceh-17::GFP
unc-130::GFP::NLS
10 µm
Θ

I extracted 5000 *unc-130* points at random (with replacement) from the segmentation data at each time point for a given embryo, and 5000 *unc-130* points at random from the following time point. As the purpose here was to correct for rotations about the A-P axis, the points were restricted to two dimensions by projecting down onto the short axes of the embryo. The resulting pairs of point clouds were fed to the point matching program CPD (Coherent Point Drift; Materials and Methods) for rigid alignment. The program generated a rotation and translation that, by eye, always brought the two point clouds into excellent correspondence. My software readjusts the initial transformations generated by the program by applying a uniform translation to fix the image frame center, thus producing a pure rotation about the A-P axis in the Y-Z plane. This re-centering step is necessary; the *unc-130* nuclei seem to undergo translations in the width and breadth of the embryo which can cause whole embryo movements in the D-V / L-R plane over a series of time points if these translations are retained.

Because any error in the sequence of rotations would generate global errors for all summed rotations involving that time point, it was necessary that mistakes be completely avoided. In tests, the system appeared to always match correctly for the small rotations between intervening time points, while a test conducted for larger rotations (for example, those generated by aligning with ten minute gaps between time points) introduced occasional gross mismatches. Plans to average rotations over multiple rotational sequences (e.g., over sequences of five jumps offset initially by a one jump step) were scrapped because observed failures made it unclear whether averaging in this way would

improve or worsen accuracy. Therefore, to generate the complete rotation I composed all time points to subsequent time points, as described. The full rotational corrections about the A-P axis for all animals between the first and last time points of their fast imaging is displayed in Figure 3.7.

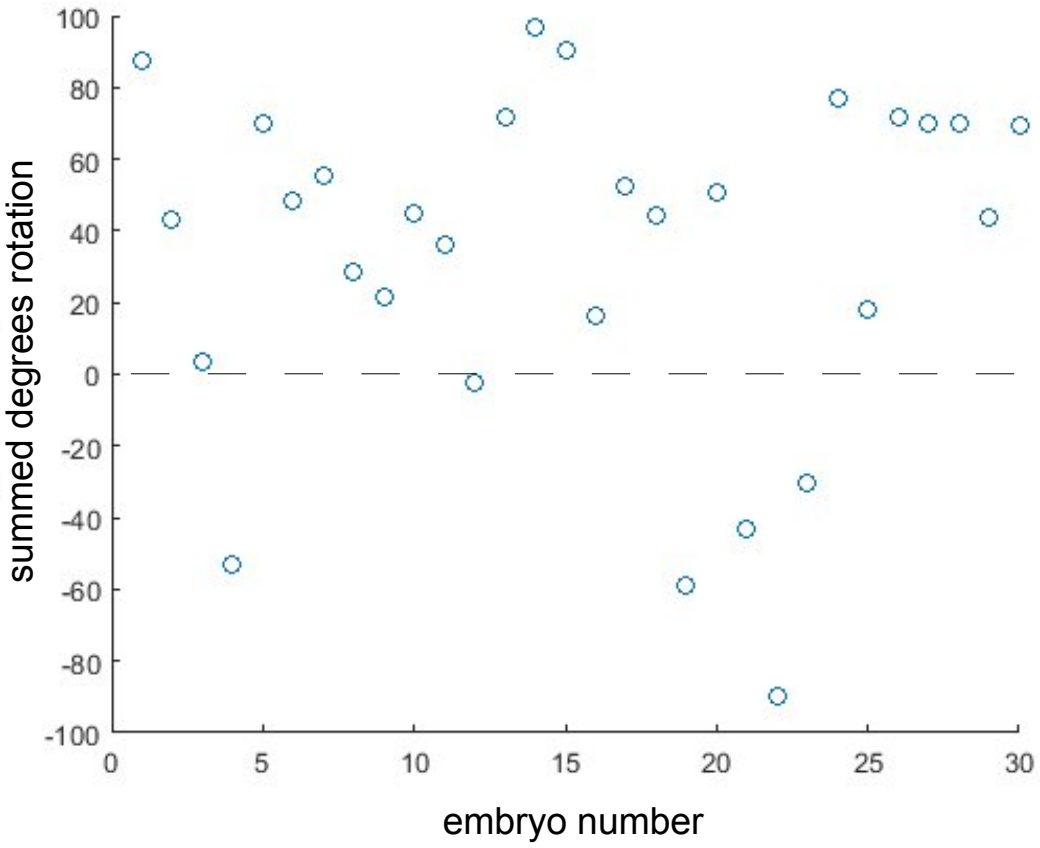

Figure 3.7: Summed rotational corrections over time course of imaging

Plotted is the negative of the developmental rotation exhibited by test embryos over the course of their fast imaging sequence, i.e., the total correction applied with the method described in the previous step. Embryos display a preference for counterclockwise rotation about their AP axes ($P < .05$, Z-test).

Alignments between embryos

Having generated coordinate systems for each embryo, I sought to align the embryos to one another in order to generate a global coordinate system which included all embryos at all time points.

First, to adjust for differences in embryonic size, I took the ball stage moments of inertia and used them to map test embryo geometries onto the reference, generating the unique linear transformation which rendered equal the average moments of inertia of the two embryos. The assumption was made here that the embryos were symmetrical in their short axes, so that the output was a uniform scale factor for length and another for width / breadth. These size adjustments are usually small: the average (absolute value) adjustment for length is 2.9%, and the average absolute adjustment for width is 1.3%, with the maximum absolute length adjustment being 9.3% and the largest width adjustment 4.8%. The results indicate that the reference embryo was very close to being a mean embryo in size: the mean (not absolute value) length adjustment to map onto the reference is a factor of 1.005, and the average width adjustment is a factor of 1.0003. Surprised by the closeness of these numbers to 1, I carried out an alignment run using minimum volume ellipsoids instead of the moments of inertia scaling, providing a partially independent means of checking the moments calculation. The two scaling calculations are highly correlated ($r = .76$ for width, $r = .91$ for length, $p<10^{-5}$ for both

calculations, by t-test) suggesting that the moments scaling adjustment corrects for real differences between embryos.

With the embryos aligned in their long axes, identically sized, and colocalized in the center of the image frame, I sought a means of commonly orienting them about their long axes at the initial time points. I noticed that the distribution of the *unc-130* marker in the early embryo displayed a chiral asymmetry between the anterior and extreme posterior ends at early time points of the fast imaging sequence. A group of posterior nuclei extend further back on what is roughly the ventral side; I was able to specifically extract these nuclei computationally because of the very precise anterior-posterior alignment of the embryo accomplished previously (Figure 3.8). I calculated the vector between the posterior nuclei average position and the anterior nuclei average position, projected the result down onto the D-V / L-R plane, and then calculated the rotation about the AP-axis that would bring these vectors into best correspondence.

Figure 3.8: Estimate initial DV-LR angle and map early time point to reference

Initial angles about the A-P axis are estimated using the raw *unc-130* nuclear segmentation of an early time point, corresponding to 20 minutes after start of fast imaging in reference. Having aligned the embryo to the X-axis and the head to +X, a vector (yellow) is draw between positions of *unc-130* nuclei in the rear of the embryo and those in the front. The projection of the vector onto the DV-LR plane provides a measure of the angular orientation of the embryo. This measure is used to align test embryos to reference, and the resulting DV-LR position is subsequently refined using a point matching method (CPD register). **A.** Side view of this embryo. **B.** Raw *unc-130* segmentation seen from the side view of the embryo. A vector (yellow) is drawn from the mean position of the posterior nuclei to the mean position of the anterior nuclei. **C.** Cartoon version of B. The vector is projected down on the head view (blue plane). **D.** Head view of embryo. **E.** Raw unc-130 segmentation seen from head view. The vector projection calculated in C is represented (brown arrow). **F.** Cartoon version of E. **G.** Vectors are calculated as in C for all embryos. A test embryo vector is aligned to the reference embryo, using the dot product. **H.** The approximate DV-LR angle calculated in the previous steps is refined using the CPD matching program acting on the early *unc-130* segmentation. An angle of rotation as well as a (small) translation are calculated at this stage. Actual alignment data shown.

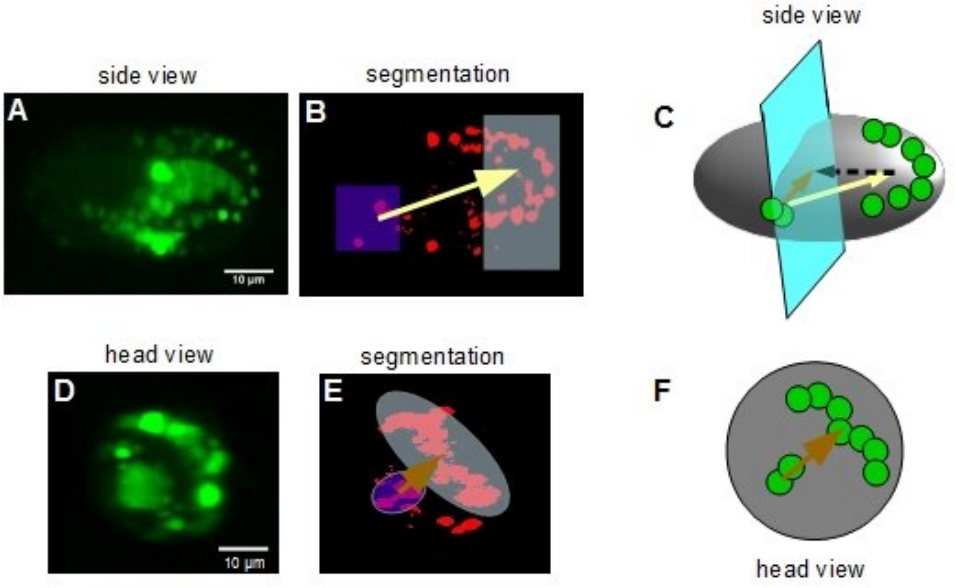
side view
segmentation
A
B
10 µm
side view
C
head view
segmentation
D
E
10 µm
F
head view

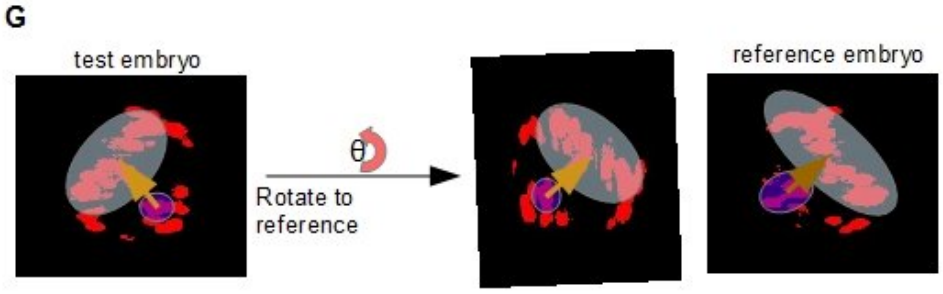
G
test embryo
θ
Rotate to
reference
reference embryo

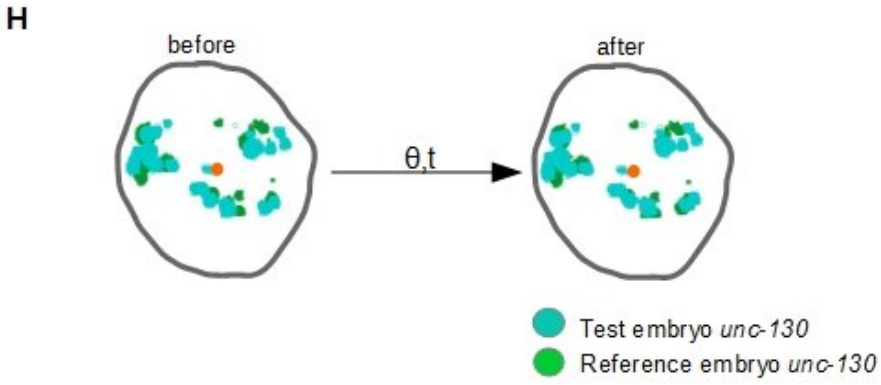
H
before
after
θ,t
Test embryo unc-130
Reference embryo unc-130

This simple heuristic produces a surprisingly accurate alignment of the embryos in their early time points. I subsequently refined the alignment by matching point clouds from the rotated test and reference embryos at the first time point, again using the CPD register program, again operating on the 2D space of points projected on the D-V / L-R plane (Figure 3.8). The threshold for identifying a nucleus (Materials and Methods) used for this early time point alignment is more promiscuous than the one described in correcting the bulk rotations, with the idea being to get as much information as possible for embryonic alignments at these early time points, even at the expense of possibly using non-nuclear information here.

At this point I could align embryos together over the whole of their time courses. I unwound each of the test embryo's time points to the first time point in its sequence (by inverting the sum of rotations to that point), then transformed to the reference embryo using the mappings described above (heuristic + correction); then mapped that time point forward by the reference embryo rotations to generate a full transformation which took any time point of a test sequence into correspondence with the equivalent time point of the reference. This method is referred to below as "indirect alignment." The reason for carrying out cross-embryo alignments at the first time point as opposed to the last is that it is much easier to extract positional cues early on that can be used to infer DV-LR position (i.e. the heuristic) than it is near twitching.

Errors in alignment continued to be observed with this method, particularly near twitching when the head moves anteriorly relative to the fixed eggshell and may twist

slightly. Therefore, as a final correction to the alignment algorithm, the individual time points of each sequence were cross-mapped onto the corresponding time points in the reference embryo, in a refinement step (Figure 3.9).

I took the 3D locations of the *unc-130* nuclei in each test embryo, after alignment to the reference, and aligned them onto reference 3D locations using CPD, to correct any lingering movements or rotations about axes other than anterior-posterior. Since the full 3D point matching alignment problem is apparently not very well posed, with enough degrees of freedom available to the point matching program that a radically wrong alignment with a huge rotation was frequently observed in tests, I altered the CPD program to strongly bias it against rotations at this stage, so that the output of the refinement step is translations of arbitrary size and small rotational corrections. There was no organic way to do this given the basic structure of the CPD algorithm, but it was accomplished by altering a section of the program to force small rotations until the simulated annealing (see Introduction) was sufficiently advanced that no very terrible point matches could be made. Then the rotational component was gradually reintroduced as the search range for corresponding points shrank past a threshold of a few micrometers. This led to excellent alignment between test and reference embryos, aside from occasional frames in which a jump attributable to excess rotation slips through, usually observed around the time of sublateral neurite outgrowth. The reasons for this are not exactly clear but might point to a greater inconsistency of *unc-130* nuclear positioning between embryos at these time points.

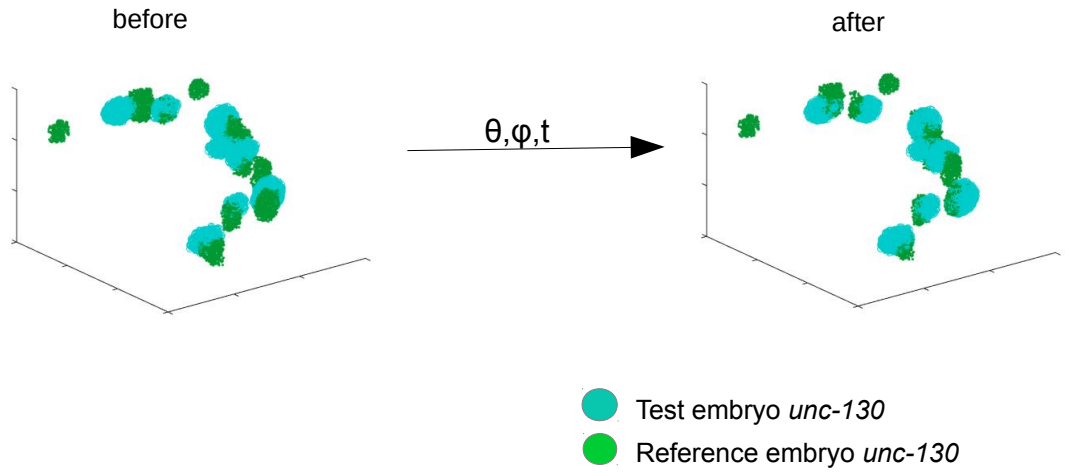

Figure 3.9: 3D fine correction of alignments

Late embryos that have been nearly matched by using the early alignment of embryos calculated in Figure 3.8 together with the individual coordinate systems calculated for embryos (indirect alignment) are matched together in a 3D refinement step using the CPD register program acting on the processed *unc-130* nuclear segmentation.

To test the quality of the alignments computationally, we generated a measure of similarity in nuclear positioning between two embryos (Figure 3.10). The method considers nuclear-segmented pixels in the test embryo and nuclear-segmented pixels in the reference embryo, and for each test pixel searches for a reference pixel within 1 micrometer of that pixel; if the program finds a pixel within 1 micrometer, that test pixel is scored as "matched." The program can also be run in reverse, to find matches for reference pixels among the test pixels. Results of this procedure show increasing accuracy of overlap for Ilastik-segmented nuclei, neurites, and cell bodies over the sequence of increasingly accurate alignments generated by: 1) no alignment, 2) centroid and A-P alignment alone, 3) indirect alignment, 4) indirect + direct alignment.

The results of the alignment are shown for a characteristic test embryo and the reference, aligned by the direct alignment method (Figure 3.10). In general, the full alignment scheme produced excellent alignments by eye in 30/33 of the embryos that it was attempted on, with the 3 that failed owing to misalignments at the early time point (with obvious misalignment of 60+ degrees of rotational error, as well as large translations away from the correct position).

Figure 3.10: Demonstration of alignment algorithm and quantitative measure of alignment accuracy

A: A representative sequence showing overlap of a test embryo aligned to reference using the full alignment algorithm. Overlaps are shown for the series of reference time points depicted in Figure 2.1**,** with corresponding time points in the test embryos. Embryos look extremely well-aligned by eye. **B:** Quantitative measure of overlap at late time points between test embryos and reference using the "pixels within 1 micrometer" method described in the text. For each pixel in an image stack in the first set, the program looks for pixels in a corresponding image stack in the second set that are within 1 micrometer of that pixel; if a pixel is found, the program scores a match. Image stacks are compared to reference at the last time point that could be matched to a corresponding time point in reference before twitching. Ilastik segmentation is used for neurites, and cell bodies, with the unprocessed (raw) segmentation used for nuclei. Overlap is shown after a sequence of four transformations: 1., No transformation (i.e. identity matrix); 2., A-P aligned (with also alignment to +X, and approximate D-V heuristic included); 3., indirect alignment (embryos are mapped using the composition of transforms from generating individual coordinate systems and early time point matching); 4., full alignment, the indirect alignment corrected with the 3D refinement step. Progressive improvements are observed in all three markers with progressive alignment steps. Left: Test embryo segmented pixels compared to reference. Right: Reference embryo segmented pixels compared to test. Error bars are S.E.M., calculated across number of embryos.

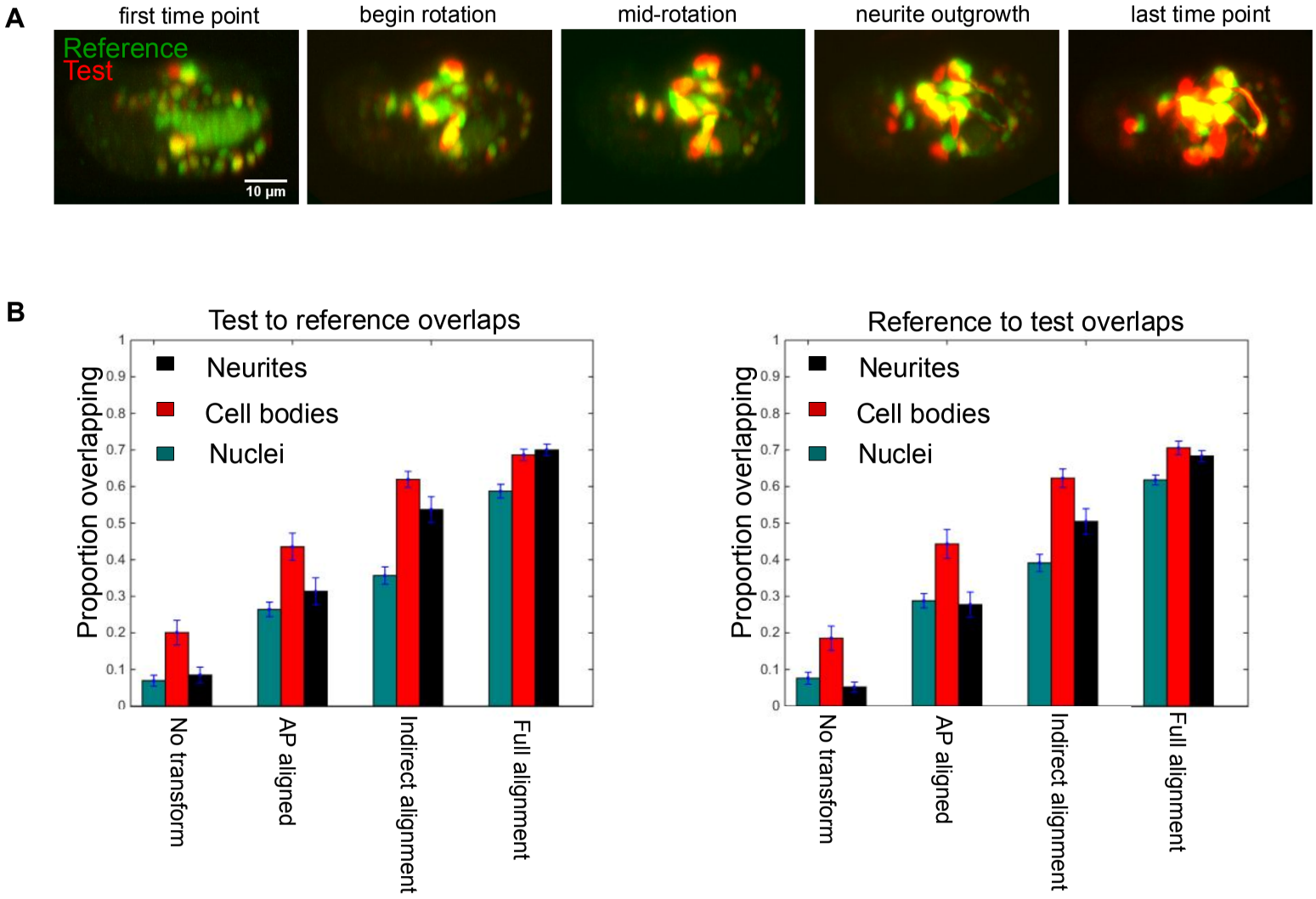
A
first time point
begin rotation
mid-rotation
neurite outgrowth
last time point
Reference
Test
10 µm
B
Test to reference overlaps
Reference to test overlaps
Proportion overlapping
Neurites
Cell bodies
Nuclei
No transform
AP aligned
Indirect alignment
Full alignment

Nerve ring positioning

I used the aligned embryo sequences to determine the degree of similarity between developing nerve rings in individual wild type animals. I manually traced out the nerve rings in the final aligned time points before twitching using the Trak-EM 2 extension to FIJI (Schindelin et al., 2012; Materials and Methods). I calculated the centers of these nerve rings by two methods, first, by simply averaging over the points of the raw trace and second, by fitting the nerve ring to a circle. (As these methods give essentially the same results, only the averaged points method is shown here.) I found that the fully aligned nerve ring centers overlap quite closely (Figure: Quantitative Positioning of Nerve Ring and Sublateral Cell Bodies). To complete the description of the nerve ring geometry, I also fit nerve rings to a plane using a linear averaging method, which would not give undue weight to the non-planar sections of the "ring" near the sublateral neurons. I found that the measured plane angles agreed to within ten degrees after alignment (Figure 3.11).

Figure 3.11: Quantitative measure of nerve ring and cell body positioning in aligned embryos.

A: Tentative identification of cell bodies in reference, based on diagrams in Sulston et al (1983) and descriptions in Pujol et al (2000). **B:** Cell bodies in test embryos are identified with corresponding cell bodies in reference based on overlap at earlier time points in the fully aligned 4D sequences. Differential placement of sublateral neurons is observed while the nerve rings exactly co-localize. **C:** For the 30 embryos that correctly aligned to reference, sublateral cell body centers were measured by hand (Materials and Methods) in their last time point before twitching that corresponded to a reference time point prior to twitching. Sublateral cell body centers demonstrate substantial variability. **D:** Nerve rings for aligned embryos were traced out with a semi-automatic method in FIJI (Materials and Methods) and their centers measured from the traces, while ALA neuron center positions were measured by hand as with the sublaterals. However, 5 of the embryos do not express *ceh-17::*GFP in the ALA neuron and so are not included in the calculation. Time points for this calculation were determined as in C. Nerve rings are precisely positioned after alignment (mean 810 nm total displacement in 3D), similar to the value for the ALA neuron (1.03μm), with both significantly less variable than the sublateral neurons. The angle of the vector pointing through the nerve ring was also measured by fitting the nerve ring to a plane, showing that the angle rarely varies by more than ten degrees in the aligned animals.

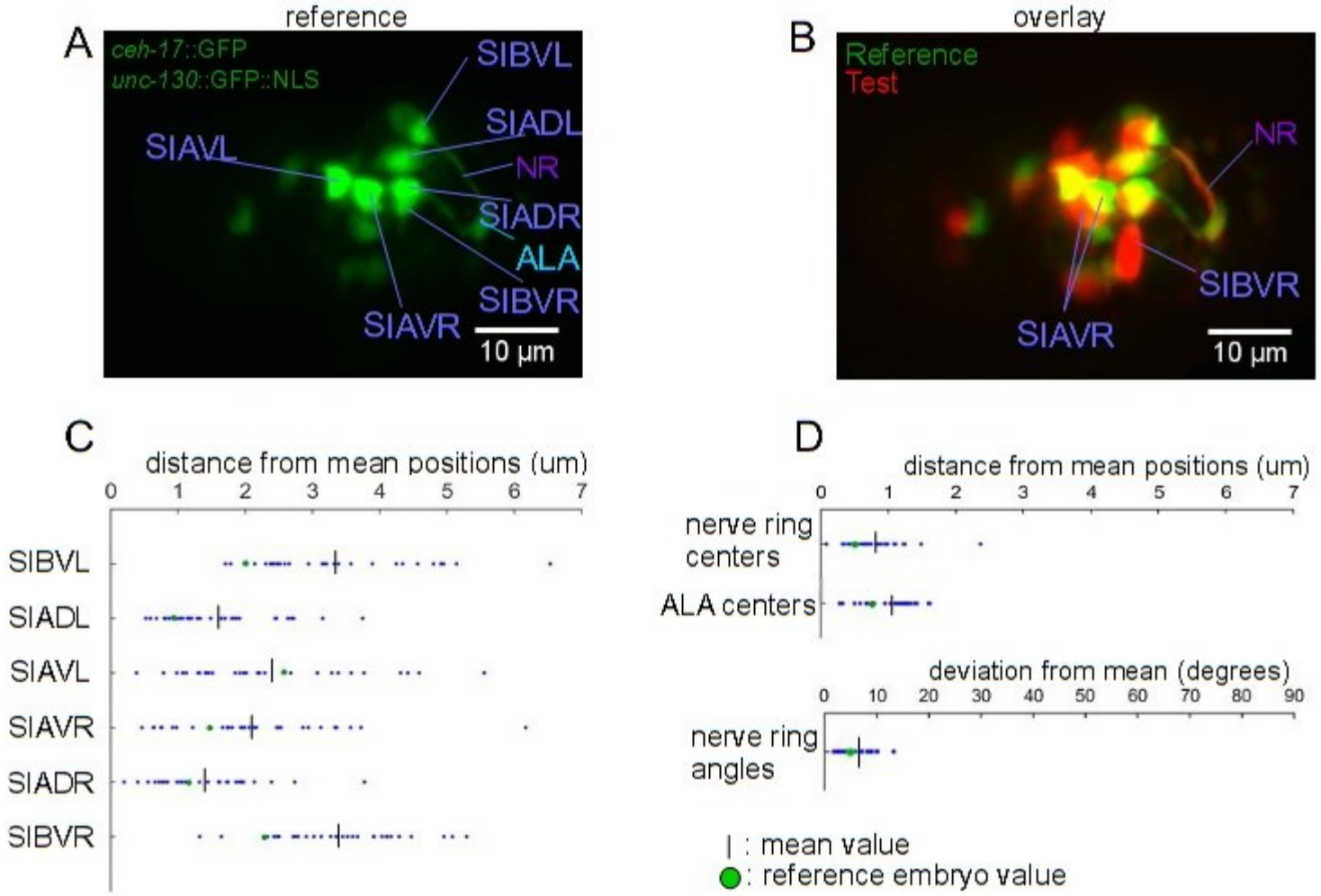
A
reference
ceh-17::GFP
unc-130::GFP::NLS
SIBVL
SIADL
SIAVL
NR
SIADR
ALA
SIBVR
SIAVR
10 µm
B
overlay
Reference
Test
NR
SIBVR
SIAVR
10 µm
C
distance from mean positions (um)
0 1 2 3 4 5 6 7
SIBVL
SIADL
SIAVL
SIAVR
SIADR
SIBVR
D
distance from mean positions (um)
0 1 2 3 4 5 6 7
nerve ring centers
ALA centers
deviation from mean (degrees)
0 10 20 30 40 50 60 70 80 90
nerve ring angles
| : mean value
● : reference embryo value

I next turned my attention to measuring the positions of the sublateral cell bodies. As described before, by the measure of similarity used to measure nucleus and neurite alignment, the Ilastik cell body segmentations came into excellent configuration (Figure 3.10) However, in looking at the data it became clear that the cell bodies that were overlapping were not always the same cell bodies. The method we used for measuring overlap is not sensitive enough to measure large clouds of points like the cell bodies, which overlap in the centers why. In following the aligned embryos through their entire sequences we were able to identify the individual cell bodies as they were born based on their overlap with the equivalent cell bodies in the reference embryo. After the cell bodies were born, they migrated to the varied positions they took up leading up to nerve ring formation. We found that individual sublateral cell bodies end up in highly variable positions (Figure 3.12), indicating that while nerve ring position is exact relative to the overall head structure, the positions of the cell bodies forming the nerve ring may vary widely.

Finally, we found that the ALA neuron, towards which the neurites of the nerve ring seem to grow in our data set, is very precisely positioned. This, together with the observation that twitching begins soon after the nerve ring impacts the ALA neurons, suggests that the ALA neuron may have a central role in guiding the neurites of the nerve ring so that its precise positioning is required for correct nerve ring formation.

cam-1 mutant imaging

As a test of the power of our alignment system we additionally imaged and attempted alignments on the OS10585 strain, which contains the same markers as the OS10584 wild type strain but with the *cam-1(gm122)* mutation introduced. We reasoned that our alignment tool might be powerful and robust enough to align strains mutated for nerve ring development onto the wild type reference frame, which would then permit us to see the effects of neuronal placement mutations on the development of the nervous system in a common coordinate system with the wild type controls. *cam-1* had previously been described as a regulator of nerve ring placement, with *cam-1* larval animals observed to have anteriorly misplaced nerve rings in ~75% of cases (Kennerdell, 2008).

Imaging and alignment were conducted as for the OS10584 strain, with one major difference: because of issues with mCherry nuclear segmentation in some cases preventing good temporal alignment of *cam-1* animals onto the wild type reference, *cam-1* animals were temporally matched using their twitching times instead of by the early time offset. This method presents its own problems, since not all *cam-1* animals twitch and in others twitching is delayed; a better method might perhaps have been to align the embryos by the timing of a known *unc-130* division in the ball stage. However, all simple methods of temporal alignment are likely to present issues in these mutants as temporal delays will likely prevent establishing clear developmental time points that consistently time the embryos across development.

Novel *cam-1* mutant phenotypes

Even without alignment, we observed a number of surprising phenotypes in the *cam-1* population. Out of 39 embryos that were imaged, 10 displayed phenotypes that had never been observed in wild-type animals (Figure 3.12).

Seven of the ten phenotypically abnormal animals exhibited a "giant nerve ring phenotype" at the time when twitching would ordinarily begin. In the giant nerve ring phenotype, the ALA neuron migrates at the time of nerve ring formation to the anterior tip of the animal, and the neurites grow out too large, apparently following the position of the ALA (Figure 3.12). In some animals, while the nerve ring grew out too far anteriorly it appeared to have normal width, while in others the width was enormous in one or both arms (stretching out to the edges of the embryo perpendicular to the normal direction of nerve ring growth). 5/7 of these giant nerve ring animals eventually executed twitching within the span of the 2 minute imaging, after one or both neurites reached the ALA neuron or visibly closed (in cases in which ALA did not express GFP).

The remaining three mutant animals exhibited unique phenotypes. In one, the growing nerve ring at the 1.5-fold stage appeared to break apart into pieces over the span of 2 frames (4 minutes), with the animal immediately arresting (Figure 3.12). A second animal totally arrested at the ball stage, with no clear cause. The third animal exhibited an apparently complete misplacement of the sublateral cell bodies relative to wild type (Figure 3.12). This animal eventually executed a (very slow, drawn out, and at first very weak) twitching and developed into three-fold. Subsequent analysis of this animal

showed that, although the nerve ring was of normal size at the start of twitching, it eventually grew to be a giant nerve ring.

Figure 3.12: Novel *cam-1* phenotypes

Left: Novel *cam-1(gm-122)* mutant phenotypes. Right: wild type animals rotated to a similar orientation. White arrow: nerve ring. Blue arrow: ALA neuron. **A.** The split nerve ring phenotype described in the text is outlined in red, with wild type comparison. This animal arrested immediately after the nerve ring broke apart. **B.** The giant nerve ring phenotype described in the text, with wild type comparison. Typical of this phenotype is the growth of the neurites past their normal destination, seemingly out towards the anteriorly displaced ALA neuron. **C.** The disorganized nerve ring phenotype described in the text. The ALA neuron and the nerve ring are not in their wild type locations, while the sublateral neurons appear too spread out and are erratically placed.

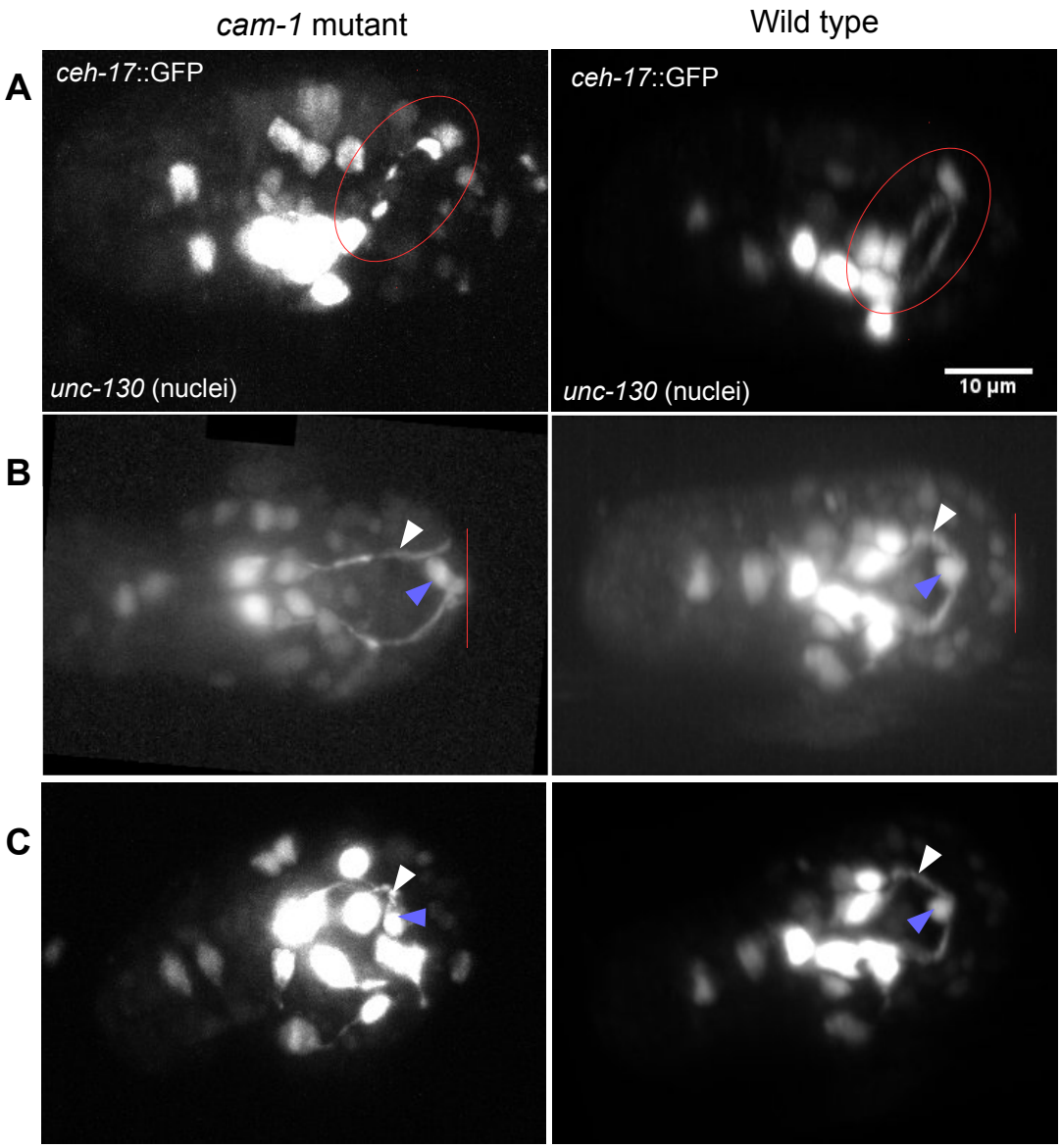
cam-1 mutant
Wild type
A
ceh-17::GFP
unc-130 (nuclei)
ceh-17::GFP
unc-130 (nuclei)
10 µm
B
C

To further characterize the giant nerve ring phenotype, and to understand whether it could be related to the anterior nerve ring phenotype previously described, I generated a dataset of 40 additional animals that were imaged starting prior to nerve ring closure (Methods), every 2 minutes for 90 stacks at low power settings. 40 embryos were imaged, of which 6 were scored as having large nerve rings (Table 1). 31 of the animals were checked for hatching, waiting at least 20 hours from fertilization in all cases, including all of the large nerve ring animals. Among these 31, 8 animals failed to hatch including 5/6 of the ones scored with large nerve rings. Of the remaining 3, 1 had the disorganized nerve ring phenotype.

Table 1: Hatching rates of normal versus large nerve ring *cam-1(gm-122)* animals. The low hatching rate and low incidence of animals with the large nerve ring phenotype suggests these animals can not be responsible for the widely prevalent anterior nerve ring *cam-1* phenotype observed in Kennerdell et al (2009).

	# animals	# hatching	% hatching
Phenotypically normal	24	22	92
Large nerve ring	6	1	17

These results strongly suggest that the large nerve ring phenotype cannot explain this widely prevalent anterior nerve ring phenotype (~75%) previously observed in larvae.

cam-1 mutants: alignments

Given that the large nerve ring phenotype was not identical with the anterior misplacement described by Kennerdell et al, we presumed that the set of seemingly normal animals in our imaging accounted for the previously observed anterior misplacement. We attempted to align the phenotypically normal animals onto the wild type reference, in order to determine absolute positioning of the nerve ring at this stage.

20 *cam-1* animals that twitched and did not exhibit the large nerve ring phenotype were set up for alignment, with the remainder discarded because of various experimental issues (Methods). Of the 20 alignments, one failed in an obvious way with the initial misrotation described in some wild type animals. For the remaining 19 animals, we found that *cam-1* alignments were generally weaker than in wild-type, with frequent frames observed in which the full alignments in particularly fell into incorrect positions. The reason for poor alignment of *cam-1* seems to be to linked to variable expression of the *unc-130* marker in these embryos, resulting in poor segmentation of nuclei, and in some cases (particularly notable in large nerve ring cases) to variations in the distribution of the *unc-130* nuclei between embryos. Nevertheless, important information could be gleaned from these alignments (Figure 3.13).

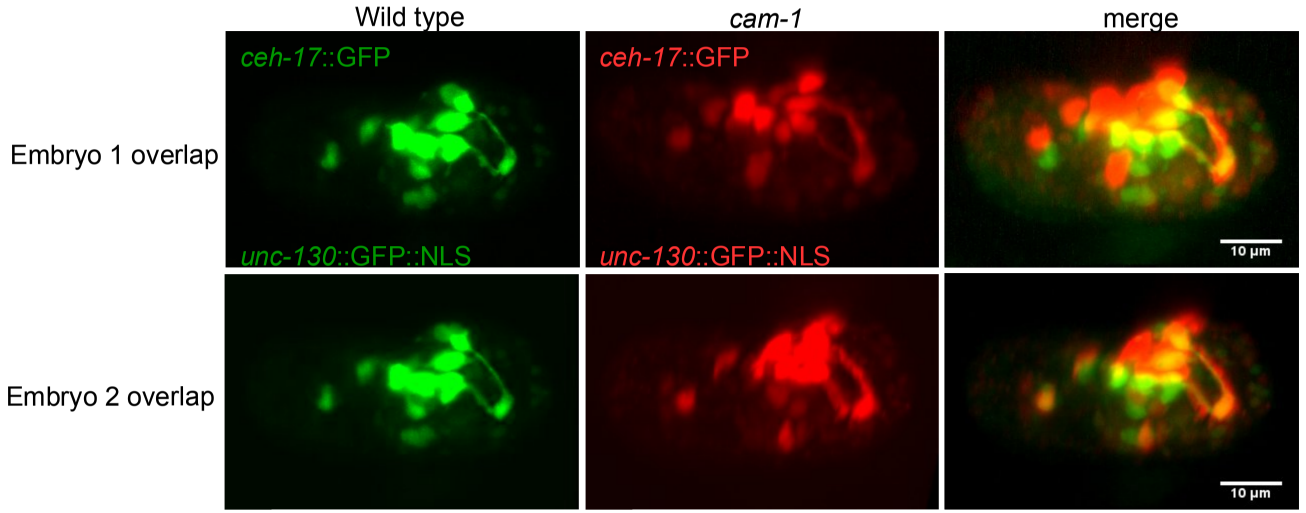

Figure 3.13: Phenotypically normal *cam-1* alignments to wild type animals

Top: A *cam-1* embryo aligned to wild type reference at the second to last time point with the full alignment method. Bottom: A *cam-1* embryo aligned to wild type reference at the last time point with the full alignment method.

I looked through the set of *cam-1* animals aligned to reference and wherever possible selected a *cam-1* animal from the last three frames before twitching which exhibited excellent alignment (Figure 3.13), judging by the outline of the head and by the positions of the *unc-130* nuclei situated at the tip of the animal's nose. In two cases, as the full alignment sequence was unusable, but the indirect alignments (done without the final correction step) displayed good overlap, I used the indirect alignment sequence instead. (Good indirect alignment with bad full alignment presumably indicates a closer correspondence between nuclei in *cam-1* and reference at early time points relative to late time points, or better expression of *unc-130* earlier). I identified 16 animals of the 19 that looked morphologically normal. Of the remaining 3, 2 had gross asymmetries between the two arms of the nerve ring (one had grown out much further than the other) which were apparent after alignment, which would throw off the averaging procedure used for finding nerve ring centers. (Only minor asymmetries are ever observed in wild type.) A third animal has what appeared to be an anteriorly displaced nerve ring with anteriorly displaced sublaterals. However, alignment to reference was evidently very poor and the animal has not yet been further investigated, except to note that the ALA neuron is also anteriorly displaced as in the "large nerve ring phenotype." I traced nerve rings in the remaining 16 animals as for the wild type case and compared the results to the wild type mean and reference (Figure 3.14).

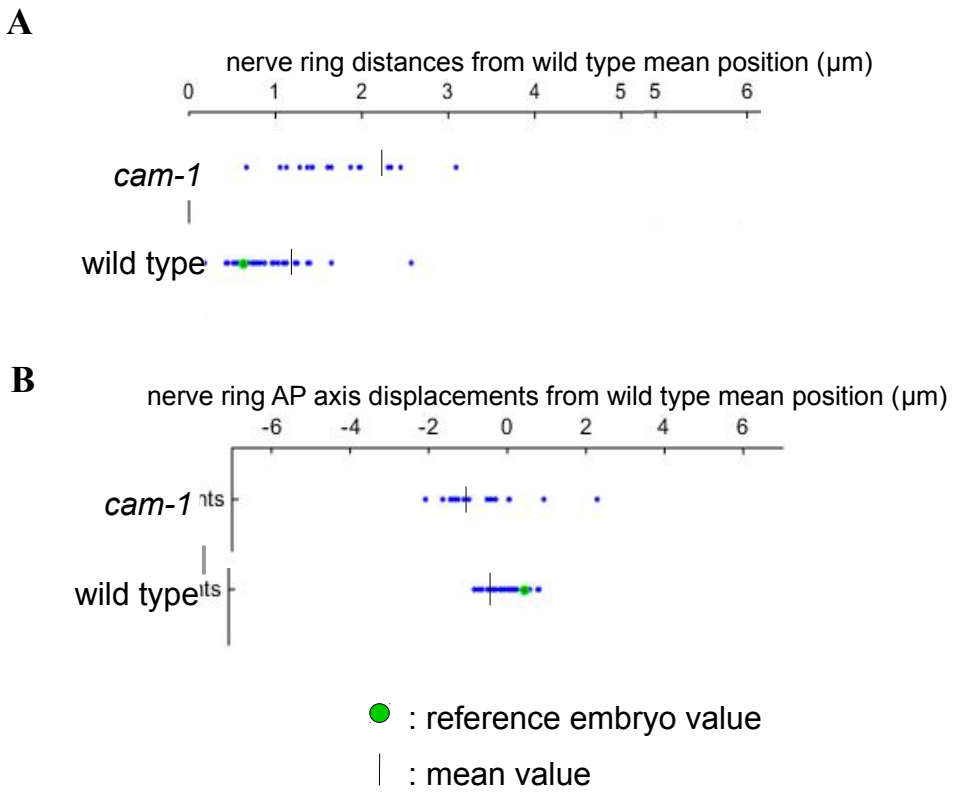

Figure 3.14: Quantitative analysis of nerve ring positioning in phenotypically normal *cam-1* animals aligned to reference

16 phenotypically normal *cam-1* animals were aligned to the reference embryo and their nerve ring centers measured as described in Figure 3.11. **A:** *cam-1* animals deviate more from the wild type mean than wild type animals do, suggesting more inaccurate alignment to reference or greater variation in positioning (they deviate similarly from their own mean position, data not shown). **B:** *cam-1* animals do not have anteriorly displaced nerve rings relative to wild type at time points near twitching.

With the one possible exception mentioned, *cam-1* nerve rings in animals destined to hatch exhibit no obvious anterior displacement relative to wild type animals. We hypothesize that the nerve ring may move in these animals after its initial placement, such that the previously observed anterior nerve ring phenotype may represent a different maintenance of position function for this gene, in addition to a role in nerve ring positioning observed here for the first time in the case of the giant nerve ring animals.

Chapter 4: Tail Spike Cell Death Imaging and Analysis

Introduction

Most cells fated to die in *C. elegans* die before differentiation, with two exceptions, the tail spike cell, a hypodermal cell consisting of a binucleate cell body with a thick, axon-like process extending to the tip of the tail, which dies during the threefold stage of hermaphrodite embryogenesis. and the linker cell, which dies during the L4 larval stage of the male. The linker cell has been extensively studied in our laboratory and to some extent in others (Abraham et al., 2007; Kinet et al., 2016; Schwarz et al., 2012), and has been shown to exhibit complex non-apoptotic genetic regulation, as well as showing non-apoptotic features during the death process in electron micrographs. By contrast, tail spike cell death has been shown to be governed by the core apoptosis pathway, with some unusual regulatory features (Maurer et al., 2007): first, the conserved apoptosis regulator *egl-1 /* mammalian BH3, although of critical importance in typical apoptotic cell death (Conradt and Horvitz, 1998), plays only a minor role in tail spike cell death; second, the tail spike cell death represents the first known example of death in the worm for which transcription of *ced-3* (the executioner caspase in the worm) is required before death initiation. Michael Chiorazzi working in our lab **s**ubsequently demonstrated that the DRE-1 protein partially substitutes for EGL-1 in the tail spike cell, with similar results identified in a human lymphoma line (Chiorazzi et al., 2013).

The work on the tail spike cell done by Carine Maurer and Michael Chiorazzi employed a *ced-3*::GFP reporter for visualization of the tail spike cell, with which it was extremely difficult to see the tail spike cell process. Interested to study the progression of cell death in all components of this complex cell, not just in the core regulation of the death pathway, Piya Ghose in our laboratory constructed an *aff-1*::GFP reporter, which is much brighter than the previous *ced-3* label, incorporating also a myristoylated GFP tag for better process visualization. This reporter has the significant disadvantage that it introduces substantial off-target labeling, most notably in a set of sensory neurons in the head. Piya used this reporter to conduct a screen in L1 larvae, pulling out mutants for which pieces of the tail spike cell failed to clear correctly. One of the genes identified in this screen was *eff-1(ns627)*. *eff-1* (Mohler et al., 2002; Podbilewicz et al., 2006) is one of two fusagens in *C. elegans* (*aff-1* being the other). EFF-1 has recently been shown to be involved in axonal fusion (Neumann et al., 2015) and dendrite sculpting (Oren-Suissa et al., 2010). Additional candidate genes were identified for screening based on their known role in apoptosis, with, for example, *ced-3*, and *ced-5*, an important regulator of apoptotic cell clearance (Ellis et al., 1991), scored for their effects on tail spike cell death. The results of these analyses, particularly evidence collected using a weak *ced-3* allele, together with the results of the screen, suggested a compartmentalization of the tail spike cell death process, with aspects of the death process in distinct regions of the cell apparently regulated by different genes.

Piya subsequently refined the *aff-1* reporter to produce a restricted *aff-1*p::GFP construct which, while still promiscuously expressed in the embryo, had sufficiently reduced expression in the head such that the tail spike cell could much more easily be visualized (*nsIs528)*. This was the reporter used for the experiments described in the results section below.

As three-fold animals move very rapidly in their eggshells, such that normal widefield imaging is effectively impossible, Piya's initial imaging of tail spike cell death was carried out in threefold embryos which were heavily anesthetized to prevent them from moving. These embryos were only imaged at one time point as the treatment was assumed to be fatal. Piya therefore observed a collection of individual three-fold animals having various pieces of the original intact tail spike cell remaining, and from this information was able to form a hypothesis as to the sequence of events involved in tail spike cell death, without however being able to directly observe the death or test her hypothesis.

The SPIM microscope I had built in the lab was considered to be a perfect tool for solving these problems associated with tail spike cell death imaging, with the high speed of the microscope permitting us to watch the death process transpiring in individual three-fold animals.

Substantial preparatory imaging was carried out before the main imaging datasets described below could be collected. I initially imaged a number of wild type and mutant animals using the full *aff-1*::GFP construct. Because of the extreme difficulty of

analyzing these movies, none were ever fully quantified in the style of the restricted promoter movies described in the results section. Clearance of the distal component of the tail spike cell was generally impossible to score because the small distal part was obscured in the images relative to the off-target expression.

There were indications in the initial imaging that I was damaging the embryos through excessive imaging and perhaps delaying or altering aspects of tail spike cell death. The main issues that gave us pause here were that the order of cell clearance and process clearance did not appear fixed in the early imaging, with some elements of the cell lingering for hours or not cleared, and with hatching delayed indefinitely. Since we wanted to get an accurate picture of all aspects of tail spike cell death, including the timing, we sought to minimize harm to the animals by keeping excitation light intensity to the absolute minimum for which the tail spike cell process could be visualized, and by starting imaging as close to the tail spike cell death as possible by carefully synchronizing the animals (Materials and Methods).

Wild type results

I imaged 14 wild type embryos with my SPIM microscope, using the *aff-1* restricted promoter. I was able to confirm Piya Ghose's hypothesis as to the order of tail spike cell death, while adding further details as to the exact nature of the process. The sequence of death events was established as follows (Figure 4.1): first, in the three-fold stage (~590 minutes after the four cell stage was reached, see methods), the tail spike cell

body rounds up and undergoes a morphologically typical apoptosis. Simultaneously or immediately afterwards, depending on the animal (2.0 +- 2.6 minutes later), the proximal part of the tail spike cell snaps off and separates from the cell body, with occasionally a small piece of the process remaining connected. Next the proximal part of the tail spike cell -- the part closest to the cell body and the main body of the animal, away from the tip of the tail -- shrinks in size while an intermediate region of the process thickens, as though the proximal part were being drawn into the thickening intermediate region. After the proximal part disappears, the remaining part of the tail spike cell, the part distal to the thickened intermediate region, begins to shrink until it disappears and only the thickened region remains. We hypothesize that this distal section is also pulled down into the thickened region, which grows brighter during this period. Finally, the intermediate and distal section disappears; this disappearance is usually sudden, leaving no trace, although in some movies fluorescent fragments were observed to linger behind in regions of the animal corresponding to the position of the distal part, in the minutes after clearance. It is not certain whether the fragments are a standard feature of tail spike cell death or whether they are only observed by chance in some movies and not in others owing to favorable positioning of the tail in the image stacks In contrast to distal clearance, cell body clearance is a slow process, as is typical of normal apoptosis, with the final fragments of the cell sometimes taking tens of minutes to clear.

Figure 4.1: Sequence of wild type tail spike cell death events

Shows the sequence of wild type tail spike cell death in cut promoter *aff-1*::GFP animals (nsIs435). Red: cell body. Light blue: intact process. Yellow: retracting proximal process. Green: intermediate region. Purple: distal part of process. Images are processed for clarity with a Gaussian blur followed by a morphological erosion.

A: An intact wild-type tail spike cell shortly before death. **B**: The tail spike cell process separates from the cell body. **C:** The proximal portion of the process (closest to cell body) retracts into the intermediate region. **D:** The proximal process is fully retracted into the intermediate region. **E:** Distal portion of process (furthest from cell body) begins retracting into the intermediate region. **F:** Last time point before distal portion of process clears.

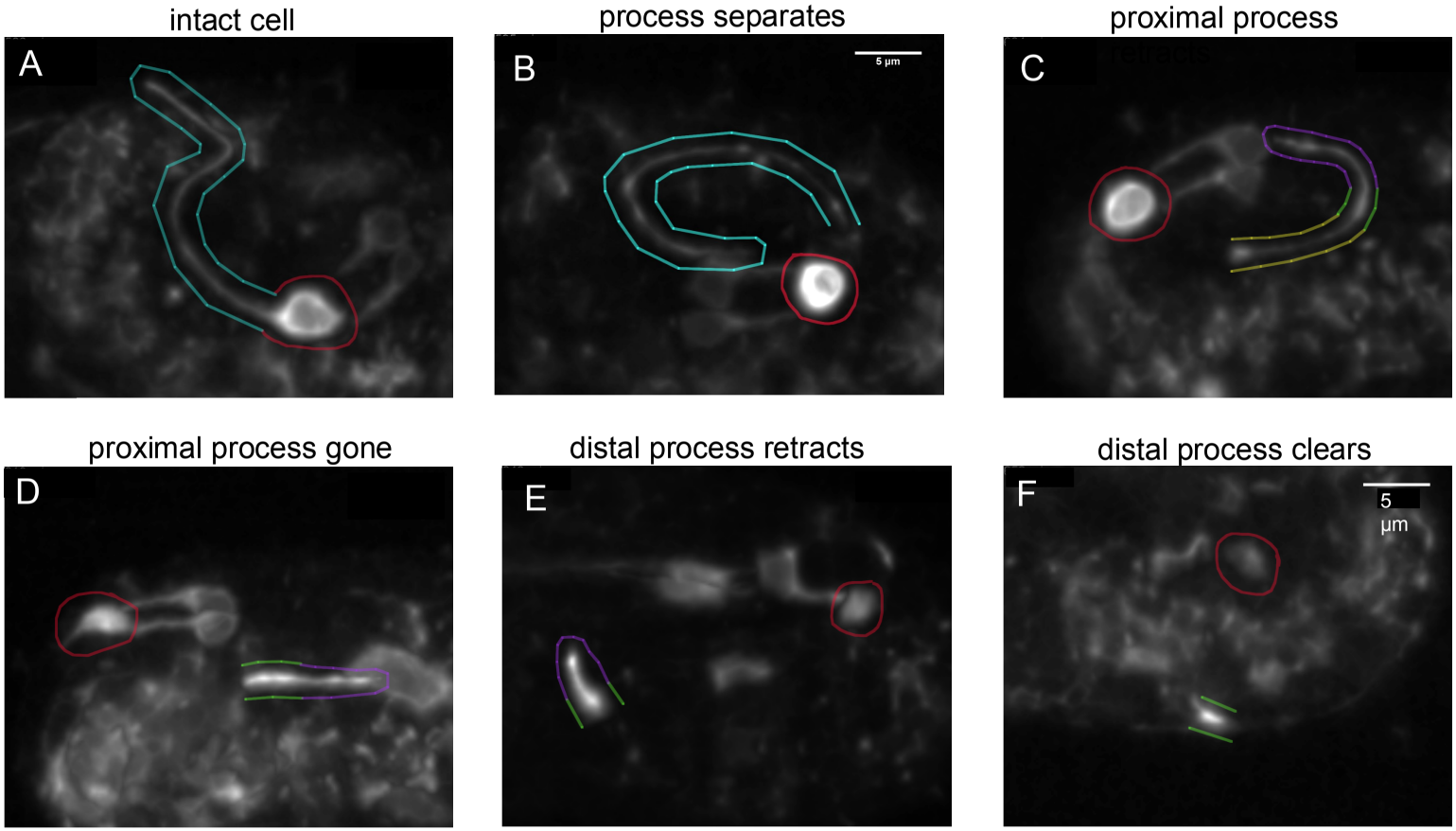
intact cell
process separates
proximal process
A
B
5 µm
C
proximal process gone
distal process retracts
distal process clears
D
E
F
5
µm

While the death process is generally extremely consistent in wild type, some variations are observed. In some animals a fraying of the process near the cell body was observed some minutes before cell body rounding commenced. In other animals a fluorescent bead was seen to linger between the shrinking proximal part of the cell and the cell body, possibly the uncleared remains of the junction between the proximal process and the main cell body. Additionally, in at least one animal the proximal part of the process was observed to "break up," instead of clearly shrinking down into the intermediate region, with beads appearing throughout the length of the proximal process.

My imaging showed this complex death process as it occurs in vivo for the first time, revealing an unexpected wealth of morphological information which is leading to new experiments, particularly ones seeking to describe the sudden clearance of the distal process component. Quantitative data pertaining to the death of the tail spike cell in wild type animals and in the two mutant strains discussed below is described in Figure 4.2.

Figure 4.2: Timing of tail spike cell death events in wild type and mutants

Timing of tail spike cell death events relative to cell body rounding in wild type, *eff-1(ns627)*, and *ced-5(n1812)* animals. Animals were scored for which both cell body rounding and hatching were visible in the movie. Initial death events (proximal separation and proximal process gone) appear identical between wild type and these mutants. Subsequent death events differ, with substantial distal clearance defects in *eff-1* animals (7/8 failed to clear, and the 8th is slowed) and in *ced-5* animals (6/10), with additionally 10/10 *ced-5* animals failing to clear cell bodies before hatching. N=10 for *ced-5* and N=14 for wild type. Not all death events were scored in all *eff-1* animals; in 6/14 total movies, hatching was observed under transmitted light instead of fluorescence; although the distal component lingered to the end of fluorescent imaging in these movies, only animals for which a time of clearance (or not) could be given during embryogenesis were scored for clearance. In addition, because of technical issues interrupting some of the movies in the middle (which were subsequently restarted), the other three death events in *eff-1* are reported for only 11 animals. The infinity sign on the X-axis is used to indicate an event that did not occur prior to hatching.

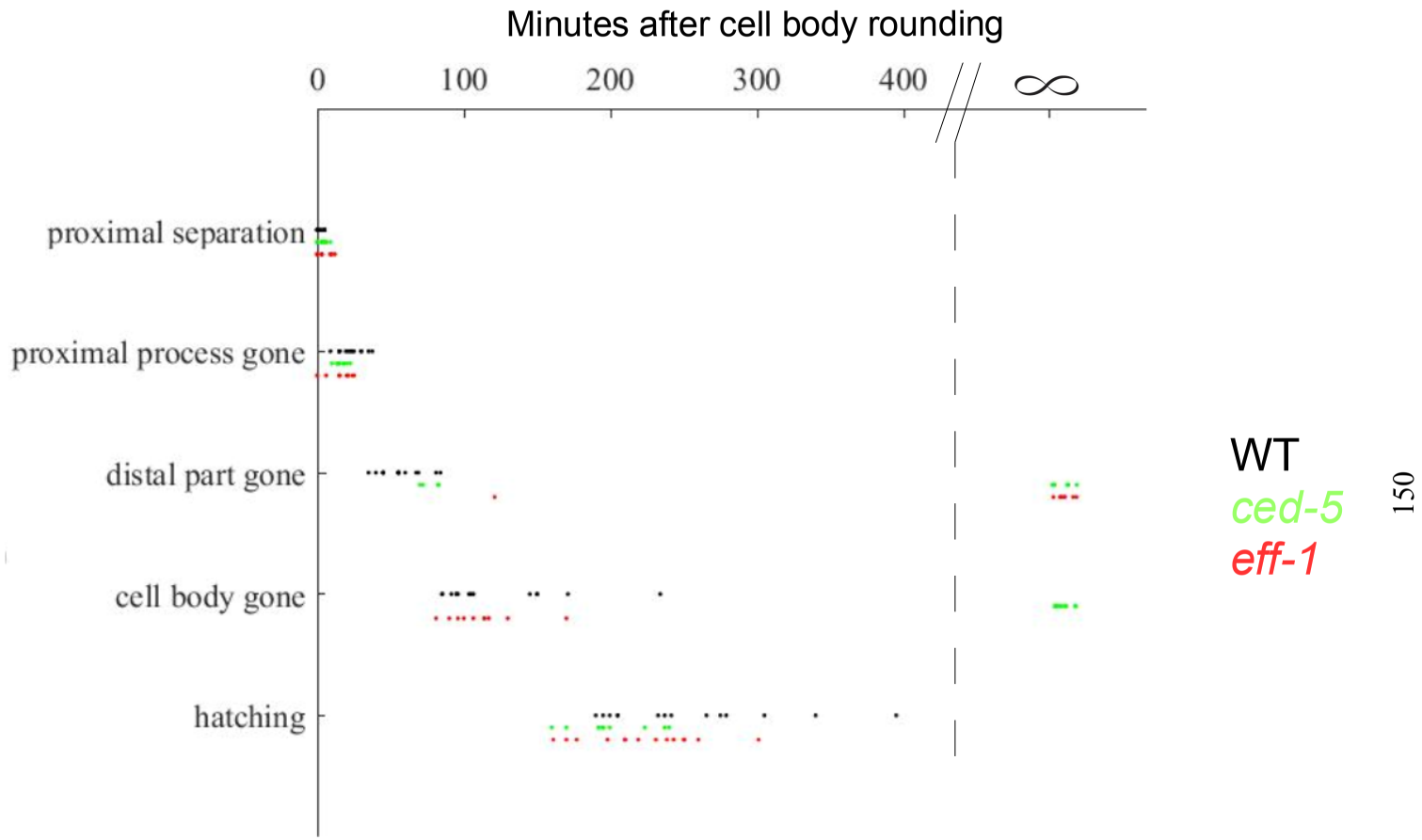
Minutes after cell body rounding
0
100
200
300
400
∞
proximal separation
proximal process gone
distal part gone
cell body gone
hatching
WT
ced-5
eff-1

eff-1 results

We imaged 14 *eff-1* animals from cell body rounding until hatching was observed (Figure 4.3). Only 8 animals were scored for distal process clearance, because fluorescence imaging terminated early in 6 movies (with transmitted light used to observe hatching). The distal component remained to the end of fluorescent imaging in all 6 of these movies, with distal component observed lingering at least 3 hours in each of these movies before the imaging terminated (compare wild type timing, Figure 4.2). At the start of death, the *eff-1* tail spike cell process is seen to be substantially shorter than wild type, consistent with the short tails of *eff-1* observed in larval animals. Nevertheless, despite the differences in the structure of the cell, many aspects of the cell death process occur as in wild type, with similar kinetics. Proximal separation occurs immediately after cell body rounding as in wild type, and the kinetics of proximal process clearance are also similar, although perhaps because the tail spike cell process is shorter for these animals there is sometimes no clear distinction between the separation and the complete clearance of the proximal part. One feature of note here is that some *eff-1* animals appear to have a break in their processes some distance downstream of the cell body already before the start of death. The death process begins to look quite different from the wild type death at the distal clearance step. The intermediate region in *eff-1* animals becomes a large, bright ball (as opposed to the elongated strip normally observed in wild type animals) and

is observed to linger for hours, as opposed to tens of minutes in wild type. Of the 8 animals for which distal clearance was followed through to hatching, only one distal part appeared to clear during the course of embryogenesis, with the rest remaining intact until after hatching. The one distal component that cleared, cleared more slowly than every wild type component. In contrast, the timing of cell body clearance (relative to cell death) is indistinguishable from that of wild type animals, suggesting that *eff-1* has no role in cell body clearance.

My imaging established that the lingering remnant observed in larval *eff-1* animals was derived from the intermediate anddistal region. Piya had previously reported that about 60 % of *eff-1(ns627)* mutant animals show a fanned tail containing a remnant of the distal process segment. About 40% have a blunt tail. The observation here of a 100% *eff-1* distal clearance defect, compared to a defect of 65% observed by Piya, may therefore be explained by the tail "falling off" in a fraction of animals, which been observed both in larvae and in embryos. Taken together, the data indicate that *eff-1* is a critical regulator of distal clearance. *eff-1* appears not to regulate other aspects of the death process, with the kinetics of other aspects of the death sequence indistinguishable from wild type despite the differences in cellular morphology.

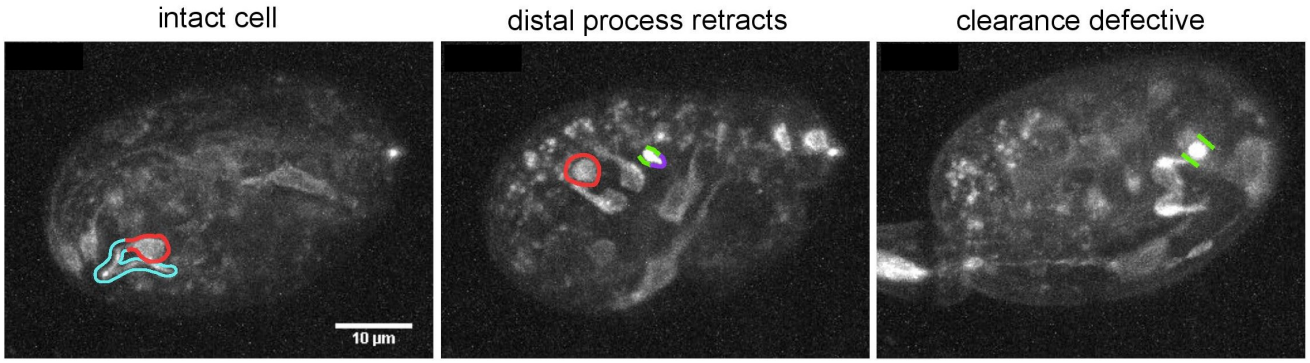

Figure 4.3: Tail spike cell death phenotype in *eff-1* mutants

Shows the typical cell death phenotypein *eff-1(ns-627)* animals, expressing the restricted *aff-1*::GFP. Red: cell body. Light blue: intact process. Yellow: retracting proximal process. Green: intermediate region. Purple: distal part of process. Times given are minutes from late 4 cell stage at 20 degrees (Materials and Methods). Intact cell: An intact *eff-1* tail spike cell shortly before death. The tail spike cell process is shorter than in wild type. Distal process retracts: death process normal to this point. Clearance defective: the animal hatches with a lingering distal component / intermediate region, while the cell body has cleared. 100% of animals exhibit at least slowing of distal clearance.

ced-5 results

ced-5 / DOCK180 (Wu and Horvitz, 1998) is a core regulator of cell body clearance in apoptosis; Piya Ghose originally identified *ced-5* for screening as a candidate gene because of its role in canonical cell death, and also because of its known role in tail spike soma clearance. The *ced-5* clearance defect of the tail spike cell soma has been reported to be about 95% by both Piya Ghose and Carine Maurer; an additional 5% defect was observed by Piya for clearance of the distal part of the process.

Figure 4.4 shows a typical *ced-5* mutant phenotype (with distal process clearance defect). Ten *ced-5* animals were imaged for the duration of the death events. In contrast to *eff-1* mutants, *ced-5* tail spike cells look morphologically similar to wild type animals. Timing the cell death process in *ced-5* animals showed that *ced-5* mutant tail spike cell death was indistinguishable from wild type cell death until the clearance phases. Of more interest was an unexpectedly large defect in distal component clearance; 6/10 animals failed to clear their distal processes by the time of hatching, compared with 0/14 wild type animals. *ced-5* animals hatch at the normal time.

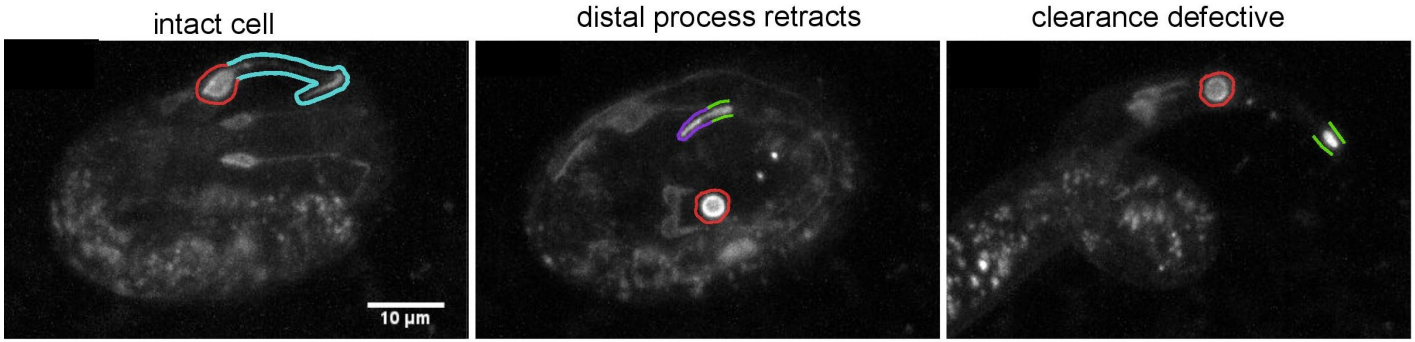

Figure 4.4: Tail spike cell death phenotype in *ced-5* mutants

Shows the typical cell death phenotype in *ced-5(n1812)* mutants, expressing the cut *aff-1p*::GFP. Red: cell body. Light blue: intact process. Yellow: retracting proximal process. Green: intermediate region. Purple: distal part of process. Times given are minutes from late 4 cell stage at 20 degrees (Materials and Methods). Intact cell: An intact *ced-5* tail spike cell shortly before death. The intact tail spike cell process resembles that of the wild type animal. Distal process retracts: death process normal to this point except that the retraction of the distal part of the process is slowed, while the cell body also fails to clear (expected for a *ced-5* animal). Clearance defective: the animal hatches with a lingering distal component / intermediate region as well as an uncleared cell body. 6/10 animals exhibit distal clearance defects at hatching while 10/10 animals exhibit the cell body clearance defects.

The extent of the *ced-5* distal clearance defect observed in embryos was surprising. The explanation of the discrepancy in our numbers is presumably that the distal component in *ced-5* is cleared shortly after the end of embryogenesis, with the absence of *ced-5* slowing the clearance of the process in a large fraction of animals but not completely preventing it.

A possible interpretation of these results, together with those for *eff-1* above, is that *ced-5* plays a clearance role for the distal process, but that *eff-1* can take over in the absence of *ced-5*; another possibility that has been suggested is that *ced-5* functions only in a structural role to facilitate clearance, possibly through its role in actin regulation (Kinchen et al, 2005). In any case, it is neither required nor is its absence quite missed in the clearance of the distal part of the tail spike cell.

Chapter 5: Materials and Methods

Nerve ring project methods

In work described in Chapter 3 of this thesis I used the SPIM microscope I constructed in the lab to image nerve ring development through twitching in a population of embryos. I also developed a novel image alignment algorithm which is used to facilitate comparisons between 4D embryo image sequences. Basic methods for this project are described below, with additional description available in the chapter.

Strains

Worm strains were maintained at 20 degrees under standard conditions (Brenner, 1974). The OS10584 strain which is the "wild type" strain of the project contains three transgenes: stIs10116 [his-72(promoter)::his-24::mCherry::let-858 3'UTR + unc-119(+)]; wgIs76 [unc-130::TY1::eGFP::3xFLAG(P000007_E01)]; and npIS1 [pceh-17::GFP, pRF4]. It was generated by crossing the RW11144 strain (obtained from the Caenorhabditis Genetics Consortium**)** into the IB8 strain (Pujol et al., 2000). The OS10585 strain was generated by crossing the PI1 strain into the NG2615 strain containing the *cam-1(gm122)* mutation (Forrester et al., 1999). *his-72* labels most cells of the embryo, with, however, weak to no expression in germ line depending on stage and weak expression in intestine (Ooi et al., 2006).

Sample preparation

24 mm x 50 mm coverslips (Fisher) were spotted in the center with 30µl of .01% poly-l-lysine solution (Sigma), let sit until dry, then stored at least a day before use to provide time for the polylysine to firmly adhere to the coverslips. The dry polylysine spot is sometimes smaller than the original droplet, and can be of oblong geometry. Only coverslips for which the dry polylysine pattern overlapped the exact middle were used, as the imageable space on the coverslip given the constraints of the SPIM system is only the central ~ 6mm x 3mm. (When subsequently placing embryos on the spot, using a ruler to find the exact center of the coverslip before beginning is extremely helpful as a guide to the eye.)

Embryos were collected for imaging by cutting gravid hermaphrodites in their first 36 hours of laying, in ddH2O. Embryos were mounted in ddH2O on the polylysine coated glass using a mouth-pipette apparatus (Fisher) and a drawn 1mm capillary with the end broken off. Embryos were blown out of the capillary into an acceptable (central) X-Y position before beginning. As embryos fell they were gently rotated into approximately the correct orientation, flat on the coverslip and perpendicular to the excitation axis, by blowing fluid on them or sucking fluid into the capillary as they fell. When embryos reached the coverslip they stuck fast and could no longer be manipulated. The desired orientation, perpendicular to the beam, minimizes expansion of the laser across the width of the embryo, thus leading to slight improvements in sectioning and light efficiency. However, as the placement procedure is difficult to implement and many

embryos could not be brought into exactly the correct orientation, embryos were accepted for imaging that fell within 45 degrees of the correct angle (i.e., two octants' worth, or 1/4 of embryos if they had fallen in random orientations). Once the embryos were stuck, the coverslips were washed 3-5 times in water to remove all loose polylysine, in order to protect the water-dipping SPIM objectives.

After all embryos were mounted, the time was noted and embryos were chosen for imaging that were between the 1 and 6 cell stages. The embryos were subsequently let sit for 2 hours at 20 degrees before start of imaging. All imaging was carried out in a 20 degree temperature controlled room. For all but 4 of the embryos, temperature was measured with a thermometer at the base of the microscope before beginning and was found to be exactly 20 degrees. It is likely that a more complicated temporal alignment procedure involving temporal scaling would have been required if temperature had fluctuated more substantially.

In the case of OS10584, 46 embryos were initially collected over 8 days worth of imaging. Subsequently, 2 days worth (12 embryos) were discarded, since they featured substantial contamination on the coverslips which caused incorrect mCherry channel segmentation (see below) on several of the embryos. 34 embryos were set up for alignment as described in the main chapter. Of these, 31 looked correctly aligned by eye while 3 exhibited obvious misalignments (>~60 degree misrotations) stemming from misalignments at the first time point.

For the main OS10585 imaging, conducted in the style of OS10584, 39 animals were set up for imaging. Of these, nearly half were discarded before conducting alignments for various reasons, including presence of mutations which prevented twitching, contamination of the coverslips, movement of the stage during imaging in one day's worth of imaging (five cases), or failure of Starry Nite segmentation. For the late-imaged OS10585 animals, 40 animals were imaged starting before completion of the nerve ring, providing at least 20 hours from fertilization before checking for hatching.

Microscope operation

All image stacks were acquired with both 488nm and and 588nm light. The 488nm laser power was measured at 165 μW +- 5 μW, and the 588nm laser at 120 +-3, both measured just before the 500mm lens, except for the late imaging experiments in *cam-1* (see below). The power was much more than enough for the cell bodies throughout the period of nerve ring outgrowth but seemed suitable for good visibility with high contrast of the much dimmer *unc-130* nuclei. The laser was scanned back and forth once for each imaging slice to prevent directional effects which were otherwise observed in the imaging. 10 ms was provided for the actual imaging, with a 20 ms delay provided between every slice to give time for the piezo to precisely settle at its final position, a ~3 ms delay for the rolling shutter and 2 ms additional used for software synchronization as previously described, giving 35 ms total per slice. All stacks consisted of 100 slices, and both red and green channels were acquired for all stacks, so each stack took 7 seconds. Stacks were subsequently truncated to 93 slices to remove

occasional bad slices at the top and bottom of the volume and to overlay the red and green channels, which were slightly offset in Z. Up to 6 embryos could be imaged at once given the timing considerations outlined above. Embryos were kept well separated to prevent the excitation light targeting one embryo from affecting another.

For the late *cam-1* imaging, a lower power of ~120µW in 488nm and 100µW in 588nm were used – although not actually used, and therefore not discussed in the main chapter, the mCherry channel was also acquired in addition to GFP as a possible aid to alignment. These lower imaging powers helped ease concerns that photodamage might contribute to the giant nerve ring defect that was sometimes observed (Chapter 3) or prevent animals from hatching.

For most visualization, registration, and position calculations, stacks were linearly interpolated in Z to produce uniform voxels. Stacks were also trimmed in X and Y to more closely match the size of the embryos. The final stacks were 351 x 251 x 287 voxels, with voxel size being 162.5nm x 162.5nm x 162.5nm, yielding an overall frame size of 57.0µm x 40.8µm x 46.7µm.

Image processing methods

Red channel nuclear segmentation was done using the Starry Nite program, which is specialized for C. *elegans* nuclear segmentation and lineaging (see Introduction). I made very slight modifications to the program for my use, affecting only superficial aspects of the program's data handling and interface. Starry Nite parameters for wild-type (OS10584) experiments were determined manually by trial and error, using imaging

done with the RW11144 strain as a guide. Starry Nite segmentation was used to time and position early wild-type embryos. The parameters were adjusted for use with the *cam-1* embryos, OS10585, to improve segmentation to the extent possible with the very dim expression sometimes observed in this strain. As *cam-1* temporal alignments tended to yield bad results (with my least squares time matching program finding a degenerate solution in some cases, and yielding large twitching offsets in others), *cam-1* animals were not aligned temporally using the Starry Nite data.

A multiple of the red channel (set mostly by eye with some computational aids at 1/15 for these imaging conditions, i.e., for the chroma filter that was used and these illumination intensities) was subtracted from the green channel before beginning, to eliminate bleedthrough of the red channel which could otherwise be substantial.

Green channel segmentation of cell bodies, neurites, and nuclei used Ilastik (Sommer et al., 2011), a random forest (Ho, 1995) machine learning method which segments images based on a combination of classifiers such as raw intensity, Difference of Gaussians and Laplacian of Gaussian (Wang, 2014). Probability clouds output by Ilastik were converted to binary matrices by thresholding, usually at .5 for all segmentation channels, although criteria were relaxed for some segmentation procedures in which more than the usual number of nuclei were desired (in anterior end identification, in DV-LR estimation, and in identification of target nuclei for the refinement step of the algorithm).

Point cloud matching was carried out using the "cpd_rigid" alignment method of the Coherent Point Drift (CPD) registration program. CPD register is a Gaussian Mixture Model method using a deterministic annealing procedure to shrink the size of the Gaussians over time**.** We chose it from among other possibilities since it has a Matlab interface, which matched well with our programming environment, and because it seemed to give better results than tests done with the older Iterative Closest Point Method**.** In addition, the theoretical underpinnings of the method seem to be stronger than in some others, with exact instead of approximate solutions to the underlying mathematical model.

Cell body center positions were calculated manually in FIJI (Schindelin et al., 2012) with center positions in X and Y estimated by eye in maximum projections and Z positions found by scrolling through stacks at the maximum X-Y position until the slice with maximum brightness at that position was found. When the max projection X-Y center was seen to be substantially off-center at the maximum brightness slice, the X-Y center was recalculated based on apparent center positions at that slice (resulting in corrections of up to a few hundred nanometers). Repeat measurements show that the procedure is accurate to within several hundred nanometers in each direction. Identification of cell bodies in test embryos with cells in the reference is reliable and based on previous colocalization at earlier stages of embryogenesis (using the full aligned movies). Subsequent identification with particular sublateral cell bodies and the ALA is accomplished by comparing my imaging results with the descriptions of the *ceh-17*

marker provided in Pujol et al (Pujol et al, 2000) and the diagrams in Sulston (Sulston et al., 1983). The actual nomenclature is tentative and may be incomplete, as SIADL and SIADR sometimes appear to have another immediately neighboring fluorescent cell. This may be simply an artifact of the imaging or image transformations, or a visual misunderstanding of the actual shapes of these two neurons. For SIADL and SIADR the apparent center position of a cluster was taken when two cells appeared to be present, with no obvious effect on the calculated variability of positioning.

Neurites were traced using the TrakEM2 add-on to Fiji, using the semi-automatic tracing method ("pencil") with short (5-10 pixel) manual steps between automatic tracing runs. When the automatic tracing method appeared to deduce an incorrect trace, the step size was shortened until the neurite was correctly traced. Short stretches were occasionally manually added ("pen") when the pencil could not find the right route. The main benefit of using the semi-automatic functionality here was that it seemed much more accurate in tracing neurite movement between image slices than could easily be done by hand. Tracing was done on the 93 slice stacks before interpolation to 287 slices, since determining the center slices of neurites was found to be easier in that way than using the interpolated version, and the program seemed to run more smoothly with smaller image stacks. Traces are exported as XML files, read in Matlab and converted to arrays and matrices for further modification and analysis.

All other image processing not described above was done using custom-built code written in Matlab.

Tail spike cell project methods

In work shown in Chapter 4 I used the SPIM microscope to image the death of the tail spike cell, a complex, differentiated cell of hypodermal origin which dies in the threefold stage of embryogenesis. Many of the methods used for this project are identical to the methods used in the nerve ring imaging project. Important distinctions are highlighted below.

Strains

Worm strains were maintained at 20 degrees under standard conditions. Wild type strains mentioned in Chapter 4 include nsIs435 (full-length *aff-1* promoter driving myristoylated GFP) nsIs528 (restricted *aff-1* promoter driving myristoylated GFP; *eff-1(ns627)* with restricted *aff-1*::GFP; *ced-5(n1812)* with restricted *aff-1*::GFP.

Sample preparation

Embryos were collected from gravid hermaphrodites in their first day of laying by cutting, and mounted on a polylysine-spotted coverslip as described above.

As phototoxicity from imaging appeared to affect aspects of tail spike cell development, we sought to start the imaging as close as possible to the time of tail spike cell death. In tests this time was seen to be developmentally determined. In order to obtain a population of animals synchronized to just before tail spike cell death, the choice was made to synchronize them at the four cell stage and wait 8-9 hours until they had developed to the correct stage. In contrast, the canonical method for synchronizing worms at later stages is to wait until a precise point in comma stage, when the tail of the

animal as it wraps around the body of the embryo is precisely perpendicular to the anterior posterior axis (Sulston et al., 1983). In my hands this method is so difficult as to be completely impracticable, yielding at most one or two embryos of the correct stage. Taking the animals at early stages when they could easily be synchronized exactly turned out to work well in most cases. We therefore used this method for all our imaging.

2-4 cell embryos were laid down on a polylysine spot and monitored to determine the time at which they reached the late four cell stage. This determination, made by looking for the period of maximum roundedness of nuclei just prior to the division of ABa and ABp, defined the stage to within around +-2 minutes. The times at which the stage was reached were noted down on a rudimentary map of the embryos, and a population which reached this time point within 15 minutes of one another was identified for imaging. A 150-300 µl droplet of water was placed on the center of the coverslip to keep the embryos moist, and the coverslip placed in a loosely sealed box containing wet paper towels (Edgar and Goldstein, 2012), with the coverslip resting on a pair of slides to keep the droplet from falling off the coverslip.

Because the length of the incubation was so long, and the *C. elegans* developmental clock depends dramatically on temperature, with a~ 5% shift in development speed per degree above 20 (Schnabel et al., 1997), it was vitally important that our temperature of incubation not vary by more than a few tenths of a percent. The coverslips were left for 8-9 hours in a 20 degree incubator chosen from among other incubators in the lab for its absolutely consistent temperature (within about .1 degree),

checked using multiple thermometers. Temperature varied with position in the incubator, so care was taken to always put the box with the embryos in the same position every time.

Although for the main set of experiments described in the chapter the absolute timing of the cell death relative to the relevant period in the 4 cell stage is measured to 588 +- 15 minutes (SD), on some other days tail spike cell death occurred substantially sooner or later than the 588 minute mark. The apparent absolute timing of tail spike cell death in these results is certainly biased by exclusion of animals which had rounded tail spike cells prior to beginning of imaging (as described in Chapter 4), thus the inclusion of the 588 minute number here is intended only as a guide for future experiments, and not as a final answer.

In hindsight, it would have been better to synchronize the embryos at a developmental time point such as twitching, which is precisely developmentally determined (Chapter 3) and could be observed under the transmitted light modality of the SPIM microscope**.** This would presumably minimize errors in cell death timing arrived at from internal variability between embryos (Bao, control) and errors arising from differing conditions during development, permitting a clearer analysis of absolute timing of tail spike cell death relative to other known developmental time points.

Microscopy methods

All imaging was conducted with the 488nm laser power set to 133 +- 5 μW. The microscope was set up to scan back and forth once on every slice, without waiting in

between slices for the piezo to settle. Actual exposure / scanning time per slice was 20 ms, which was necessary for good visualization of the dim restricted promoter at these low powers. As these are rapidly moving three-fold embryos, spending an additional 20 ms between slices as with the OS10584 strain to improve the accuracy of slice separation and regularize it across the frame is unfeasible and leads to lower ultimate imaging quality. All volumes were taken with 800nm between slices and 55 slices in total. The 800nm slice spacing, approximately the Nyquist limit (half the resolution limit) for this microscope, while in theory excessive for visualizing every element of the tail spike cell, was found to help dramatically in practice. A slice separation of the order of the actual resolution in Z, 1.6 um would result in every element of the tail spike cell process being in focus in one frame. I find generally that it is extremely helpful for visualization to see sections of a cell more than once, especially dim and difficult to see aspects of a cell. An element of shading, or a slight variation in texture like is seen in the "fraying" observed in tail spike cell death may be one's imagination if seen in one frame but is certainly real when it is seen in several frames. The doubled image spacing then serves as a kind of internal check on image analysis.

Analysis

For the final datasets, embryos were imaged at 3 minute resolution and at 10 minute resolution. All animals for which cell body rounding was visible in the movie (i.e., for which the cell body had not died before the start of imaging) and for which

hatching was also observed were kept for analysis. As the 3 minute datasets and the 10 minute datasets did not seem to differ, these sets were pooled.

Timing of tail spike cell death was analyzed by looking through the set of maximum projections of the 4D movies and looking through full stacks to more closely investigate difficult-to-see components whenever this proved necessary. "Cell body rounding" was scored at the first stage when the cell body appeared completely round (up to about 5 minutes after rounding was initially detected); "proximal separation" was scored from the first time when substantial damage (beading) or a clear break was detected between cell body and proximal process; "proximal process gone" was scored from when no remnant of proximal process could be seen (not counting the occasionally observed free-floating membranous beads, derived from the proximal process and cleared separately); "distal process gone" was scored from the moment no remnant of distal process was detected; "cell body gone" from the moment no cell body remnant was detected; "hatching" was scored at the last frame before the embryo hatched. For cell body clearance and distal process clearance, we always looked forward three frames from a tentative clearance detection (looking through the full stacks) in order to verify that the process would not subsequently reappear (at the time of final clearance the cell body in particular is a small, dim object in a sea of brighter objects, and can sometimes be incorrectly scored as absent only because it is obscured by a brighter cell). When a decision was difficult to make between two neighboring frames the average of the two was used.

Chapter 6: Discussion

Overview

A limitation of much of the existing work on the *C. elegans* nervous system is that it is carried out after the end of embryogenesis, in larval and adult systems that are more amenable to experimental investigation but perhaps less informative as to the close details of the development as it occurs. The recent renaissance in fluorescent microscopy has facilitated investigation of nervous system development in vivo, not just in *C. elegans* (Wu et al 2011, Wu et al 2013, Christensen 2015) but also in other organisms (e.g., Ahrens et al., 2013) While the single plane illumination microscope I built in the lab was not strictly essential for studying development in the 1.5-fold embryo, which can be imaged with for example a spinning disk confocal microscope, it does permit imaging fairly dim reporters (the *unc-130* marker, as well as the *ceh-17*::GFP in the neurites of the nerve ring) at high contrast with good temporal resolution over a prolonged period of time. This has led to new insights into the reliability of nerve ring construction in the animal, as well as new phenotypes for a known regulator of nerve ring positioning (*cam-1*).

In contrast to the imaging of 1.5-fold animals, a single plane illumination microscope or related instrument is absolutely required for imaging events happening in the rapidly moving three-fold stage. I used the SPIM microscope I built in the lab to

image tail spike cell death in three-fold animals, yielding novel information about the sequence of events occurring in the death of the tail spike cell. By imaging the death process as it transpired, as opposed to in L1s and later stages, we were able to identify a stronger phenotype for the gene *ced-5* and suggest a stronger phenotype for *eff-1* mutant animals.

In the remainder of this chapter, I discuss the surprising accuracy of the alignment algorithm, as well as choices made during its construction, alternative routes that could have been followed, and possible extensions. I describe implications of the results presented earlier in the nerve ring alignments chapter, including possible explanations of why nerve rings are so accurately positioned, discussion of the rotational corrections, and *cam-1* phenotypes. Next I describe results of the tail spike cell death imaging. Lastly I discuss several upgrades in the design of the SPIM microscope that could result in improvements in imaging quality.

The alignment algorithm shows surprising accuracy

The utility of the algorithm I constructed is demonstrated in its capacity to align *C. elegans* nerve rings to a precision of less than a micrometer. This number is remarkably small considering the variety of places in which error might have occurred. Firstly, the average error in placing a single photon with the microscope averaged over all 3 dimensions (given as a standard deviation, as opposed to the usual diffraction criteria, for easier comparison with the nerve ring result), is in the neighborhood of 1.5

micrometers. However, it should be noted that the capacity with which microscope optics can correctly position a point source is much worse than that with which it can position the center of an extended body composed of point sources; with computational processing, the possible resolution scales like 1/sqrt(N) (Thompson et al., 2002) where N is the number of photons counted. Something like this procedure must operate as I trace the outlines of the neurites by hand and average the resulting points, which produces an average over hundreds of individual pixel positions, each of which is individually inaccurate. In fact, a majority of the individual pixel positions themselves are averaged by the semi-automatic tracing that was used (between the fixed points indicated by hand), as the TrakEM2 program looks for context in neighboring pixels in order to find the center lines. The repeatability in finding the centers of cell bodies (including ALA) by hand seems to be about 1 or 2 pixels in each direction, or roughly 500nm in total. Lastly, there are the errors attendant on whatever imperfections may be produced by the alignment algorithm. In general, it is clear that the accuracy of placement of the ALA neuron and the nerve ring neurites in a real embryo must be better than the mean distance figure I determined here, suggesting extremely accurate placement indeed in the real embryo.

Our temporal alignments are also quite accurate, judging by the standard deviation of twitching offsets across these animals – 7.4 minutes, after alignment – especially considering the ten minute intervals between images in the acquisitions that were used for this temporal alignment as well as the absolute minimum inaccuracy that is

baked into the procedure from the two minute resolution of the resampling. The explanation for this accuracy is likely a combination of two factors: first, all time points of nuclear information are used in an averaging procedure, thus improving possible accuracy down to around 2.5 minutes or lower; second, room temperature was observed to be highly constant over the course of these experiments, suggesting that temperature variation did not shorten or lengthen time courses substantially relative to one another. It is worth noting that embryos did not have much time to drift out of temporal alignment after being aligned by the nuclear divisions, with only 138 minutes in the reference embryo between the end of the nuclear divisions and the onset of twitching. Nevertheless, twitching must be exactly developmentally determined if bulk nuclear divisions can be used as an accurate predictor of twitching time.

Possibility of using the algorithm with markers other than *unc-130*, and coordinate system dependence on marker distribution

With some modifications the alignment algorithm I developed might be used to align *C. elegans* embryos containing positional markers other than the *unc-130* nuclear marker. Any marker which can be segmented can be used to align embryos from one time point to the next using these methods, but a requirement for this not to introduce artificial movements to the animal is that the distinct segmented elements (e.g., segmented nuclei) not execute substantial collective movements in any direction over which alignment will be conducted. In tests of the alignment algorithm, permitting translations to act in the time point to neighboring time point alignment procedure (they

are currently eliminated) would result in a drift of the entire embryo in the Y-axis; this suggests that there may be some collective movement of the *unc-130* nuclei in the Y direction over time which simulates movement of the embryo as a whole when the positions of only these nuclei are considered. A similar issue provides the explanation for why a full 3D alignment was not conducted between each pair of time points. In general, rotations of the embryo are not observed using the *unc-130* matching system (judged by movements of the sublateral neurons in the embryo, which provide the only possible check on this), except sometimes small rotations around the time of neurite outgrowth (not in the reference), which suggests that this is a suitable system for use in solving the problem of rotations over time. As the head of the embryo does not move substantially in its other (nominal) five degrees of freedom until near twitching, this makes the *unc-130* distribution sufficient for producing an invariant coordinate system for most of the period that was imaged. This rotational invariance over time would have to be shared by any other marker used for generating an invariant or mostly invariant coordinate system over time for each embryo. It should be noted that the coordinate systems constructed here do not actually keep the head fixed for all time points, because the twisting and anterior movements of the head at the late stages are not compensated for in the reference embryo (and in fact, 3D alignment of the reference embryo to itself seems to introduce additional twists and movements); if accurate comparisons between widely separated time points (separated by more than a few minutes) are required in the late stages before twitching, then it will be necessary to somehow fully correct for these movements in the reference.

A final advantage of using the *unc-130* nuclei for alignment is the chiral asymmetry of the distribution in the early embryo, which was used to approximately match the DV-LR axis to reference in the early time point. Some similar feature must exist in the distribution of any other marker used for this kind of alignment, if automated alignment at the early time point is required (otherwise, possibly a human could guess at the right answer, and subsequent alignments could proceed normally, although this would probably require multiple tries to get right).

The use of a particular reference embryo for alignments might be considered. At the time that the reference embryo was selected, no information was available as to the positioning of its cell bodies, neurites, and *unc-130* nuclei relative to other animals. As described in the alignments / nerve ring chapter (Chapter 3), the reference embryo was chosen primarily for being well-aligned to the anterior-posterior axis in its natural orientation, and for having the nerve ring clearly visible in the same. It might have turned out that the reference embryo was very different from all other animals, in which case these alignments would have failed and we might not have known the cause. The alignments work because all animals are actually quite similar; presumably, any embryo could have been chosen as the reference without altering the results presented here.

A key feature of our alignment algorithm is that it is almost completely automatic. The only part of the algorithm that requests or requires human intervention is in the determination of regions of interest, which was done once for the Starry Nite software and once when truncating images down from the original size for ease of processing.

Our alignment algorithm might be compared with a method presented in a recent paper (Christensen et al (2015); Introduction). An enormous advantage of the Christensen et al (2015) alignment algorithm is that it permits alignments in the worm past twitching, where my algorithm aligns only up to the 1.5-fold stage. Without a marker extending down the length of the animals (the bilaterally symmetric seam cells were used in that paper, although other markers such as body-wall muscle which has a four-fold symmetric distribution down the animals' length, might also work) it is impossible to conduct the kind of local registration that is described there throughout the two- and three-fold animal. In my case, an alignment of the head region might be done for some length of time past twitching by imaging more frequently and tracking the positions of the u*nc-130* nuclei frame by frame using a 3D point set alignment. One additional point to note is that the *unc-130* marker appears to be expressed earlier than the seam cell marker, which may be an advantage in that it permits establishing connections between the early cell body positions in the embryo and later positions (permitting tracing precursors of neurons into their final locations before twitching, for example).

Our positional alignment algorithm, coupled to the temporal alignments, provides a framework for placing neurites from different strains onto a common coordinate system (for example, the reference embryo described here) until twitching. This will facilitate experiments in which neurite positioning and timing of outgrowth can be compared between different embryos expressing GFP in different neurons, thus perhaps

contributing to a larger goal shared by some other researchers of generating a map of neurons in space and time in the developing embryo (Santella et al., 2015).

The nerve ring is precisely positioned:

My alignment algorithm has shown a very precise, repeatable placement for the nerve ring structure at the time of twitching, as measured by the centers of the nerve ring and the relative angles of planes fitted to the nerve ring. ALA neuronal cell bodies, towards which the axons of the nerve ring seem to grow out in all cases in wild type, are also precisely positioned at twitching, while the sublateral neurons that may construct the nerve ring are positioned with substantial variability. In general, and as described above, the accuracy of positioning of ALA and nerve ring centers in real *C. elegans* embryos must be better than what was determined here because of the various sources of error in the analysis. Precise placement of the nerve ring is apparently a highly evolved quantity in *C. elegans.*

The precise placement of the nerve ring is not so surprising in hindsight, as it is a central target towards which more then half the cells of the animal must ultimately send their axons. The developed nerve ring may secrete positional cues which guide incoming axons into their correct positions in the overall nerve ring structure. If the nerve ring were substantially misplaced, then these positional cues could cause large scale realignments of neuropil throughout the embryo; some axons might not receive guidance cues, and fail to form synapses onto their correct counterparts. If the nerve ring functions

as a central meeting ground for neurons, then the location of the meeting ground ought to be confirmed and agreed upon in advance.

A model of nerve ring development which has been suggested in our lab based on work of Georgia Rapti (Rapti et al, in preparation), and which was also suggested by earlier functional ablation results obtained by Satoshi Yoshimura (Yoshimura et al., 2008) suggests that the nerve ring may be established by the CEP sheath glia (Oikonomou and Shaham, 2011), with the sublateral neurons SIA and SIB subsequently directing their axons along the glial processes. If this is the case, then it would help to explain the inaccuracies in positioning of the sublateral neurons, as the glial processes which they may use as a substrate for further growth have already been established. Future work will be required to determine the initial accuracy and exact timing of CEP sheath glial outgrowth compared to sublateral neurons, perhaps using the automated alignment system described here.

Observations on the bulk embryonic rotations

The arbitrary direction and magnitude of the rotations observed over time in the *C. elegans* embryo were also noted in embryos at an earlier stage than those imaged here, by Ralf Schnabel and collaborators (Introduction; Schnabel et al., 1997), using DIC. The method used by Schnabel to identify overall rotations, taking a mean rotation over clusters of cells, sounds very similar in some ways to the method that was used here, although the automatic nature of the procedure here of course is a major difference.

Schnabel reported that the embryo does not appear to rotate as a solid body, with distinct nuclei rotating by different amounts, a feature which was not observed here. In general, the rotations noted by Schnabel cannot be the same as the rotations corrected for here, as they occur before the start of the fast imaging in my setup.

If embryonic rotations vary in direction relative to a fixed point, they may not vary relative to external forces. A preliminary analysis has suggested that these rotations are not correlated with initial geometric configuration of the embryo, thus suggesting that these rotations may represent an active process on the part of the embryo. How the embryo would generate a force to push itself in bulk against the eggshell is unknown.

It should be noted that there may be differences between bulk movements observed in these animals and those observed in animals which are compressed for mounting (i.e., animals mounted between a slide and a coverslip). Compression is likely to affect bulk rotation, and has even apparently been observed to alter aspects of the internal development of the animal, reducing migratory range of individual cells (Giurumescu et al., 2012); non-compression is clearly the better approach when possible for getting closer to the "natural state" of the animal.

Identification of a new phenotype for *cam-1*

In experiments conducted on *cam-1* we identified a new phenotype for the gene, a giant nerve ring phenotype seen in 15-20% of embryos in which the ALA neuron advances to the front of the embryo and the arms of the nerve ring grow out to be too

large, proceeding towards the ALA neuron. *cam-1* had previously been implicated in an "anterior nerve ring" defect, which appears not to be the same as our giant nerve ring defect. Since only 1/6 giant nerve ring animals hatched (representing 1/30 animals studied in the relevant experiment) the giant nerve ring cannot possibly account for the ~75% of animals described as having the anterior nerve ring phenotype in the previous paper. Additionally, the anterior nerve ring phenotype described by Kennerdell appears to be a comparatively much smaller defect, while in one giant nerve ring animal the length before twitching was measured using a spline-fitting technique and found to be 2-3 times as large as a regular-sized ring.

Other defects rarely observed in *cam-1* animals include radical misplacement of the sublateral neurons and a bizarre defect in which the nerve ring appears to fall to pieces during development. Additionally, a number of animals display asymmetries in their nerve ring growth, with one arm appearing to terminate far short of the ALA while the other arm has reached it. Closer inspection sometimes reveals a tiny process reaching down to the ALA neuron; the nature of this process is unclear, but perhaps the likeliest explanation of it is that it is a process stemming from the ALA neuron.

Although alignments of *cam-1* animals were not as smooth as in wild type for a variety of reasons (see Chapter 3), we were nevertheless able to generate a dataset of 16 animals which displayed reasonable alignment using our algorithm. Although one of these animals might have an anterior nerve ring (see Chapter 3), the remainder of the nerve rings were shown not to be anterior, which is in sharp contrast to the prevalence of

the anterior nerve ring phenotype described for this gene in earlier work from the Bargmann lab (Kennerdell et al, 2009). This result likely indicates that the anterior positioning defect which was observed for *cam-1* in larvae is in fact a defect in maintenance of the nerve ring structure once it is formed and not a defect in initial positioning.

Imaging tail spike cell death as it occurs allows for more sensitive observations:

My work on the tail spike cell demonstrates the sequence of wild type tail spike cell death events for the first time, establishing the relative timing of various features of the death and clearance in this complex differentiated cell. I also followed the tail spike cell death in *eff-1* and *ced-5* mutants, which were imaged extensively and timed in the same way as the wild type animals. This imaging contained some surprising results, including a high prevalence of distal process clearance problems in *ced-5* animals and a stronger than expected clearance defect in *eff-1*.

The sudden disappearance of the distal part of the tail spike cell which was observed in my movies, along with the outsized role played by the *eff-1* fusagen in distal clearance, suggest that a novel method of clearance possibly involving cellular fusion may be entailed in eliminating the distal part of the tail spike cell. We speculate that *ced-5* may act in clearance of the distal part of the tail spike cell, not in its character as a regulator of apoptotic clearance, but possibly in a different role, affecting actin dynamics involved in the shrinking of the tail spike cell (Kinchen et al, 2005). Future experiments

gauging whether *ced-5* functions cell autonomously, as would be expected in the case that it is acting as an actin regulator, or non-autonomously, which would be expected if it is required in neighboring cells to aid in clearance, will help determine the role that this gene is playing in clearance of the tail spike cell process.

Future experiments using the SPIM microscope will follow additional candidate genes such as *ced-1* (another regulator of apoptotic clearance), and a weak *ced-3* mutation which has provided results as to the compartmentalization of the nerve ring. Preliminary experiments have not shown a defect for *ced-1* in process clearance, while temperature sensitive *ced-3* seems to have more common defects visible in the developing embryos than when the same animals are observed as larvae.

In general, imaging cell death as it occurs, as opposed to waiting until many hours after the death to begin imaging (which is the only way possible to image tail spike cell death with conventional imaging modalities) seems to be a more sensitive tool for detecting subtle phenotypes and genetic disregulation. In the case of some mutants, as in the discrepancy between larval distal component survival and embryonic distal component survival in *ced-5*, it may be the case that animals find a way to compensate for defects and eventually to execute a normal clearance program. Monitoring the kinetics of the death events as they occur provide a way of identifying defects involving subtler timing issues, and also help to isolate the effect of mutants by ruling out possible effects in some compartments.

Next steps for the SPIM microscope

The SPIM imaging system I built is a basic system of the kind, using no additional optics or systems beyond those required for generating light sheets and tracking them with a piezo in multiple embryos. As discussed in Chapter 2, Our SPIM system was set up with a laser-scanning mode of light sheet creation (e.g. Keller and Stelzer, 2008), as opposed to forming the sheet through a cylindrical lens, which permits us the flexibility to pursue any of several possible resolution enhancing techniques. DSLM permits a structured illumination approach for improved contrast (Keller et al. 2010); this approach can be implemented directly using the AOTF without additional optics. DSLM also permits a single plane illumination confocal microscopy approach (Silvestri, Bria et al. 2012). Perhaps most intriguingly, DSLM can be easily modified to sweep Bessel beams instead of Gaussian beams, which, when used in conjunction with structured illumination, may lead to very large improvements in lateral and axial resolution (Planchon, Gao et al. 2011, Gao, Shao et al. 2012).

As funding becomes available, we would be interested to expand the microscope to include a diSPIM component (Wu et al, 2013); to accomplish this some parts of the microscope body would need to be swapped out (parts of the top block), to permit laser access to the current detection objective and also to permit a camera access to the current excitation objective. Space was left behind the microscope on the optical table to permit addition of the relay lenses and other components necessary to split the beams and carry half the light to the detection objective, with the correct focusing. There is a major cost

associated with upgrading to diSPIM, which is the addition of a second sCMOS camera, which might come to $25,000. The ~5-fold improvement described in axial resolution when going from diSPIM over regular SPIM means this adjustment would be well worth making for some kinds of imaging, when possible; for example, improved depth discrimination would be very helpful for determining the boundaries of cells when they sit directly on top of one another.

DIC is a completely standard imaging modality in *C. elegans* laboratories, and is the routine means by which the overall structure of an animal can be imaged to compare with fluorescent expression in substructures. In my own work, absence of DIC has presented major difficulties in imaging the tail spike cell and presenting it in its cellular context. Although to my knowledge DIC has never been utilized in a SPIM system, it should be possible to introduce it by including a polarized light module impacting the sample through the excitation objective. The approximately 45 degree angle of incidence of the excitation objective to the bottom detection objective is such that a substantial fraction of the light would enter into a 1.3 NA oil objective mounted there (such an objective collects 60 degrees of light from each side of the vertical), and be transmitted to the bottom camera. The low light efficiency of this kind of setup should not be a problem for DIC, although it might be problematic if many slices needed to be taken for reasons of phototoxicity. A DIC crystal would be included in the objective mount, which is typical for many of the objectives in our laboratory. A slot is available to fit an analyzer in place in the bottom light path, where color filters for fluorescent imaging currently sit

(see Appendix A). This would not be a hugely expensive addition (probably totaling a few thousand dollars) and would greatly improve the functionality of the microscope if it could be made to work.

While I was building the microscope, several commercial versions of the single plane illumination technology came into existence. ASI manufactures a diSPIM microscope, with all of the laser optics (the galvanometers, mirrors, and lenses) built into arms of the microscope body. Zeiss, LaVision and a variety of other companies offer their own light sheet implementations, with variations such as progressive scan of a beam waist across a thick sample and single objective implementations. While there is an enormous benefit to using pre-made systems, in that, in theory, they can simply be set up and experiments can begin without further effort, one disadvantage is that the system might not be exactly tuned to one's particular specifications. For example, the light sheet microscope which is now available in the Rockefeller Biological Research Imaging Center uses a setup which cannot be effectively sized down to a *C. elegans* embryo. An additional advantage of building a microscope directly in the lab is that it is much cheaper to do it this way (the SPIM microscope I constructed totaled ~$125,000 as opposed to ~$300,000 -- $500,000 for a commercial system (Alison North, personal communication). A home-built microscope can be altered to suit individual experiments, for example by changing the style of scanning or beam size to suit the speed or size of the sample to be imaged; also, the details of such a system will be intimately understood by the person who built it, thus permitting on-the-fly fixes and optimal operation.

The SPIM system has made it feasible to study tail spike cell death as it occurs, and can produce beautiful, high contrast images of the sublateral neurons as they grow into the nerve ring, which was perhaps a contributing factor in making possible the highly accurate alignments that were described in Chapter 3.

Appendix A: Introduction of IR laser Induction System to SPIM Microscope

Introduction

The common laboratory method of inducing heat shock in *C. elegans* raises the temperature of the entire worm or embryo by placing the whole animal in a heated incubator or water bath. Internal and external temperature will very rapidly equilibrate for such a small organism, so whole animal heat shocks lasting just 5 minutes are possible using this coarse method. Heat shock is routinely used to activate transgenes in the animal, particularly for assessing the temporal requirements of gene activation since heat-shock mediated gene expression can be induced at various points in development (e.g. Yuzyuk et al., 2009), as well as to force hermaphrodites to generate unusual numbers of male progeny. While the researcher may prefer to target only a subset of cells with a heat shock, for instance, to induce genes only in cells of interest, the standard method described above leads to transactivation of heat shock factor (HSF1) (which activates gene transcription) throughout the animal.

Anuipriya Singhal has developed a laser heat-shock induction system in which gene expression is induced by a 1455nm laser (Kamei et al., 2009). This 1455nm wavelength is situated near the excitation maximum for absorption by water in the near-IR region; the choice of this wavelength maximizes heating while minimizing overall

radiation and thus minimizing photodamage. In addition, because of the focusing effect of the laser, Anu's system can be used to activate gene expression in a single cell at the 200 cell stage, while producing very little of the off-target labeling which characterizes heat shock induction efforts carried out with the typical method. Anu is using her system to generate induction of fluorophores in individual neuronal precursors, to compensate for a general lack of availability of highly specific markers in the study of embryonic neurodevelopment in the worm (Georgia Rapti, personal communication). In practice, because of kinetic limitations, Anu is limited to inducing cells ~120 minutes prior to the beginning of morphogenesis, to allow for bright expression of fluorophores at the time of neurite outgrowth. At this developmental stage, induced cells will divide, on average, 2 times, leading to the expression of heat-shock reporters in 4 progeny cells.

Anu and I are in process of setting up a system for bringing Anu's laser induction method to the SPIM microscope platform, by mounting a high NA objective on the bottom imaging axis and so introducing a focused IR beam to the sample. By combining the IR induction and SPIM systems, we hope eventually to be able to identify cells of interest using the lineaging component of the StarryNite program (Bao et al, 2006), activate fluorescence in those cells using the IR laser, and then monitor their subsequent development using the gentle imaging on the SPIM. The ability to activate fluorescence in particular cells will overcome a problem commonly faced, for example, in neural studies in the worm, in which an absence of sufficiently specific markers makes it

difficult not only to identify cells but even to separate them optically as they crowd each other in the image.

Construction of IR laser light path

Introducing an IR laser in the underside imaging pathway involved several steps. First, we needed to split the light coming off of the existing 1455nm laser which Anu used. Our microscopes are situated next to one another on neighboring optical tables, but we decided against the direct approach of using a beamsplitter and redirecting the light from one table to the other with a set of mirrors and relay lenses, because we were concerned that the amplitudes and phases of vibrations of one table would vary from those on the other and thus result in shifts of the laser position or angle relative to the sample. Instead, we chose to split the light and focus it down into a single mode fiberoptic cable and pipe the laser to the other table in this way (single mode cables maintain beam size over a distance without the need for additional optics). The output position at the SPIM optical table is fixed in this way relative to the sample, up to the stability of the collimator and the optical table itself to internal vibrations. By careful tuning we were able to achieve a coupling efficiency which is more than adequate for our needs (~50%); however, the system requires periodic retuning of mirrors (on a time scale of weeks) to maintain good coupling, with small (perhaps thermal) movements of optical components on Anu's table sufficient to move the laser away from the position of maximum coupling to the collimator. The power instability of this system will require

measuring the output power of the laser, preferably at the sample, before every imaging session, which we will accomplish using a Thorlabs power meter and photodiode power sensor (ThorLabs, S122C) secured to a coverslip and mounted on the microscope stage.

The light path on my optical table after it leaves the collimator is shown in Figure A.1. The mirror closest to the collimator (marked 1 in the diagram) is approximately conjugate to the plane of the sample while the next mirror in the light path (marked 2) is approximately conjugate to the back focal plane of the objective (i.e., angular movements of the mirror produce positional tracking of the beam at the sample) facilitating the alignment of the system. The mirror marked 4 sits rectilinearly with respect to the 500mm tube lens in position 3 and the entry port on the microscope, and redirects the laser light straight into the microscope. In practice, given the severe constraints imposed by having a laser entry port not much larger than the beam (~15mm), we usually only move the mirrors that are closest to the microscope (positions 2 and 4). To obtain a large positional movement the position 4 mirror is moved and angular corrections instituted with the mirror in position 2.

We introduced a longpass dichroic (Q495lp, Chroma Technology) in the light path in the microscope body (Figure A.2), to redirect incoming laser light up towards the objective. On its way to the objective the light bounces off of an internal mirror before reaching the underside objective, which focuses it down onto the sample. The dichroic allows for GFP fluorescence imaging simultaneously with IR induction, allowing us to visualize nuclear markers for use in targeting specific cells.

Figure A.1: Diagram of IR light path on SPIM optical table

The IR laser (1455nm) passes through a collimator and is expanded 10 times by a pair of lenses acting as a beam expander (marked BE) to ~15 mm diameter before passing into the microscope entry port. **A:** Front view of microscope. **B:** Breakout of IR light path on optical table with corresponding light path overlay. **C:** Diagram of IR light path on optical table. **D:** Legend for C.

A

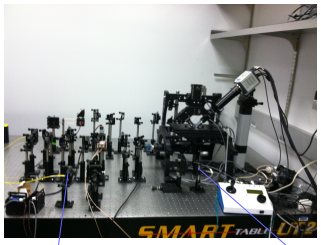

B

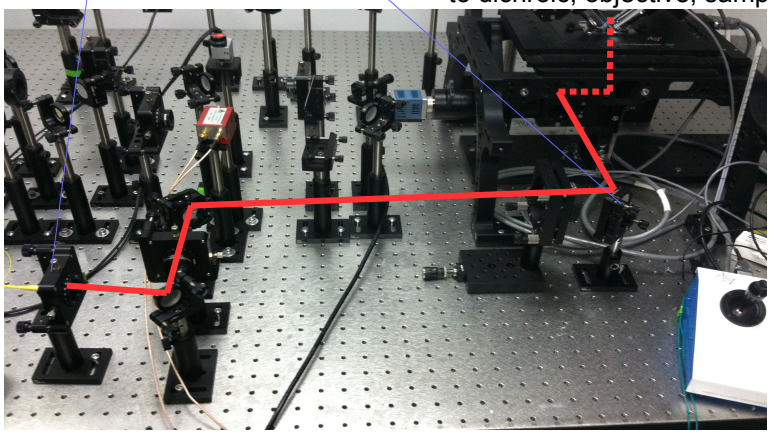

C

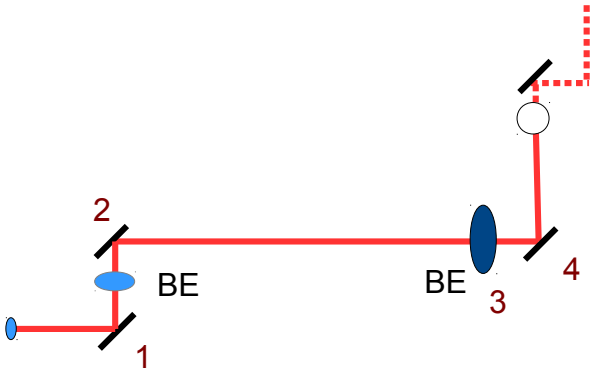

D

collimator lens, f = 5mm

lens, f = 50mm

lens, f = 500mm

microscope entry port

plane mirror

IR laser

Figure A.2: Diagram of IR and widefield light path in SPIM microscope body

The IR laser (1455nm) is redirected by a dichroic to the microscope objective (Olympus, 40x 1.3 NA) where it is focused on a sample. Back reflections of the IR beam from the coverslip, redirected to the PCO camera, are used to determine the IR laser position. Additionally, the microscope is set up to do widefield imaging using the bottom light path with illumination provided by the SPIM excitation objective. **A:** Front view of microscope. **B:** Breakout of light path within the microscope, showing excitation and emission pathways as well as back reflections. **C:** Diagram of light path on optical table. **D:** Legend for C.

A

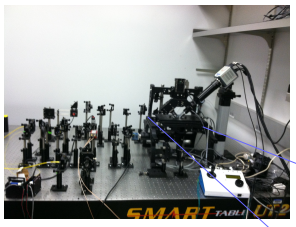

B

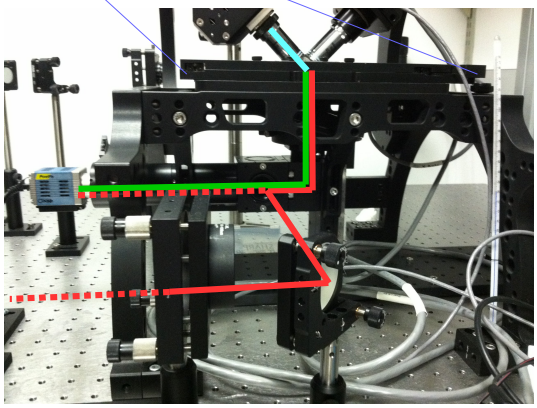

C

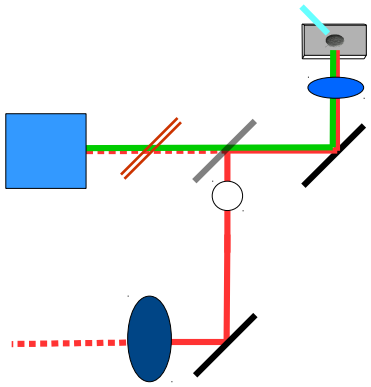

D

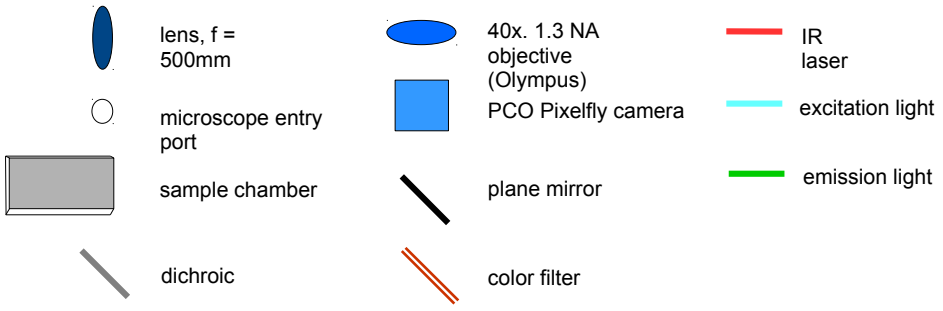
lens, f = 500mm
microscope entry port
sample chamber
dichroic
40x. 1.3 NA objective (Olympus)
PCO Pixelfly camera
plane mirror
color filter
IR laser
excitation light
emission light

Alignment of IR laser

The strategy for alignment of a beam to a particular nucleus is to get the nucleus in focus in the underside objective light path by conducting fluorescent imaging, while keeping the IR laser aligned to the bottom optical axis (i.e., with the beam coming in straight). The IR beam and the nuclear fluorescent image will be focused at different distances by the lenses involved (lens focal distance is somewhat wavelength-dependent); however, the required Z offset will be only several micrometers, is fixed, and can be applied without further calculation every time if it can once be determined. For this to work, the beam must be coming straight in to the sample; otherwise offsets in multiple dimensions are required, adding complexity.

To determine the X-Y position of the beam at the sample, and to straighten the beam, we made heavy use of a method previously used by Anu on her microscope, observing the reflections of the beam off of the coverslip surface. We manipulated the table mirrors and shifted the position of the underside tube lens as needed to alter direction of laser entry into the system until the spot was situated in roughly the center of the imaging frame. Then, we further manipulated the lenses until the diffraction pattern off of the coverslip could be seen to be symmetrical with movement of the objective in and out in Z. The observed diffraction pattern is not stable between experiments, varying most likely with the angle of coverslip placement in the holder; this limits our capacity to

identify beam angular errors to the precision with which we can set up the coverslip to be perfectly flat.

Widefield Imaging from Underside Objective

For the induction experiments, cells of interest are identified based on nuclear GFP markers which label a large subset of cells (e.g., the *unc-130*::GFP marker which was used extensively in Chapter 3). (Eventually, StarryNite lineaging may be used to define the cells of interest.) In order to maintain light efficiency, the embryo will be imaged using SPIM microscopy from the top axes, and then the coordinates of the appropriate cell will be fed to the bottom axis for IR induction. This setup requires that coordinates of a nucleus are transformed from the top to the bottom axis. To calculate this transformation, corresponding points must be identified in images from both the SPIM imaging objective and the underside IR induction objective. We therefore developed a widefield strategy to image from the underside objective to go along with the SPIM imaging.

This imaging involves using the light sheet-volume from the top light path as though it were widefield excitation illumination, illuminating the entire sample to collect one slice's worth of fluorescence from the bottom objective. As with a normal widefield microscope, to gather a new slice's worth of information, the underside objective is moved to a new Z position, while the illumination remains fixed. While this kind of widefield imaging may damage embryos, our idea is to primarily use the imaging only on

test embryos for alignment, and subsequently apply these transformations to embryos used for induction, without the need for further imaging at the bottom objective. To make this widefield modality work, the operation of the bottom camera / microscope objective had to be synchronized to the light sheet production from the top axes, with one exposure taken per light-sheet volume generated.

Synchronization of underside light imaging to SPIM system

The underside imaging uses a several generations old PCO pixelfly CCD, bought on Ebay for $200, which has much of the functionality of a camera worth around 40 times as much. (It replaced a commercial Canon camera which I had originally mounted there, which was not sensitive enough for fluorescent imaging.) Because the Pixelfly camera needed to be operated from a legacy PCI board (not PCIe), and PCI slots have not been standard on computer motherboards for years, we connected the camera to an old Dell Inspiron PC which we had in the lab. The native PCO software, as well as the built-in Micromanager (Edelstein et al., 2014) control options are limited in their flexibility, so I wrote a control script for the camera in the Beanshell language (closely related to Javascript) which can be run out of the Micromanager console.

In order to use the PCO camera for widefield fluorescent imaging as intended, the acquisition timing of the camera had to be synchronized to the light sheet production which was determined by the separate set of software (Labview) operating on the SuperMicro workstation. While the PCO Pixelfly board has several pins from which the

state of the camera can nominally be read, facilitating synchronization with other electronic devices, none of these pins were operational on the board we were shipped. I therefore set up a system for software synchronization, which was simply done by having the SuperMicro computer remotely monitor the Dell computer for files being written and the Dell computer wait for a certain file to be written to disk before beginning acquisition with the PCO. Triggering of individual frames is accomplished using the (functional) TTL input trigger on the camera, working off the DAQ card (which is controlled from the SuperMicro computer). This juryrigged system for synchronization produces some missed frames as a result of triggers occurring during image acquisition, so all images are checked for two things before proceeding to acquire the next slice; that they not be blank, and that they not be identical to the previous image, which are the usual outputs of the PCO camera when acquisition is mis-triggered or times out. This system, while resulting in sometimes as many as 20-30 additional acquisitions over 100 slices, is effective in taking clean, functional widefield stacks.

Sample finding was found to be vastly more difficult with the much smaller image frame of the PCO camera than with the large sensor of the Canon, so I replaced the 200mm bottom-side tube lens that came with the microscope with a 100mm tube lens we had on hand, with which the nominally 10x Olympus objective had only an effective 5.5x magnification. This made sample finding again straightforward. Although smaller magnification lenses might have been used instead of reducing the tube length, the working distances of these small magnification lenses (roughly tube length /

magnification, or around 50mm for a 4x lens) is so enormous that they cannot be successfully mounted on the existing microscope body.

The nominally 40x Olympus objective which we used for fluorescent imaging and inductions had an effective magnification of 22x after replacement of the tube lens, somewhat reducing resolution when the correct magnification for matching the diffraction limit to the PCO pixel size of 6.45μm (the Nyquist limit, (Chen et al., 2000) is 33x**.** Nevertheless, imaging quality was sufficient for segmentation and registration (see below).

Alignment between top and bottom axes

The light efficient SPIM imaging on the top axis can be used to provide coordinates for induction to the bottom axis.

To facilitate alignments between top and bottom axes – in other words, to determine a rigid transformation carrying the top rectilinear coordinate system of camera X, Y, P axes into the X, Y, Z axes of the stage and underside objective system – it was found to be convenient to image 3 dimensional samples in both cameras for alignment. While one possibility is to mount fluorescent beads in an agarose gel, perhaps using a point set registration method after guessing the correct rotation, I chose instead to use an alignment system with which I was already quite familiar and which can be simply mounted on a coverslip along with other samples. I imaged fluorescing *C. elegans* embryos using both the top and bottom axes, and, using the same system with which I

had previously calculated transformations between embryos, calculated instead the alignment parameters which would bring the same embryo into registration from two different views. The transformation generated by conducting this alignment on one embryo can be subsequently used to transform between views for any other embryo, such that the IR laser could be targeted to particular nuclei identified from SPIM imaging without taking a harmful widefield stack. This system still requires work before it will be complete; in particular, calculating correct Z positions in the widefield system with its stretched out point spread functions is complicated, and may require additional tools such as centroid measurements of beads along with the imaging of embryos. A sample of this alignment is provided in Figure A.3.

Figure A.3: Method for calculating the transformation parameters between top and bottom light paths

A: The same embryo is imaged in top and bottom light paths, the SPIM light path and the underside widefield imaging light path that was constructed for this project. The embryo is aligned to itself (i.e., the two views are registered) using the alignment algorithm of Chapter 3. The transformation T required to map the embryo onto itself is recorded. **B:** The transformation T recorded in A is used to align views for a different embryo. Imaging from both views is done only to test that the transformation is working correctly and is not necessary for alignment.

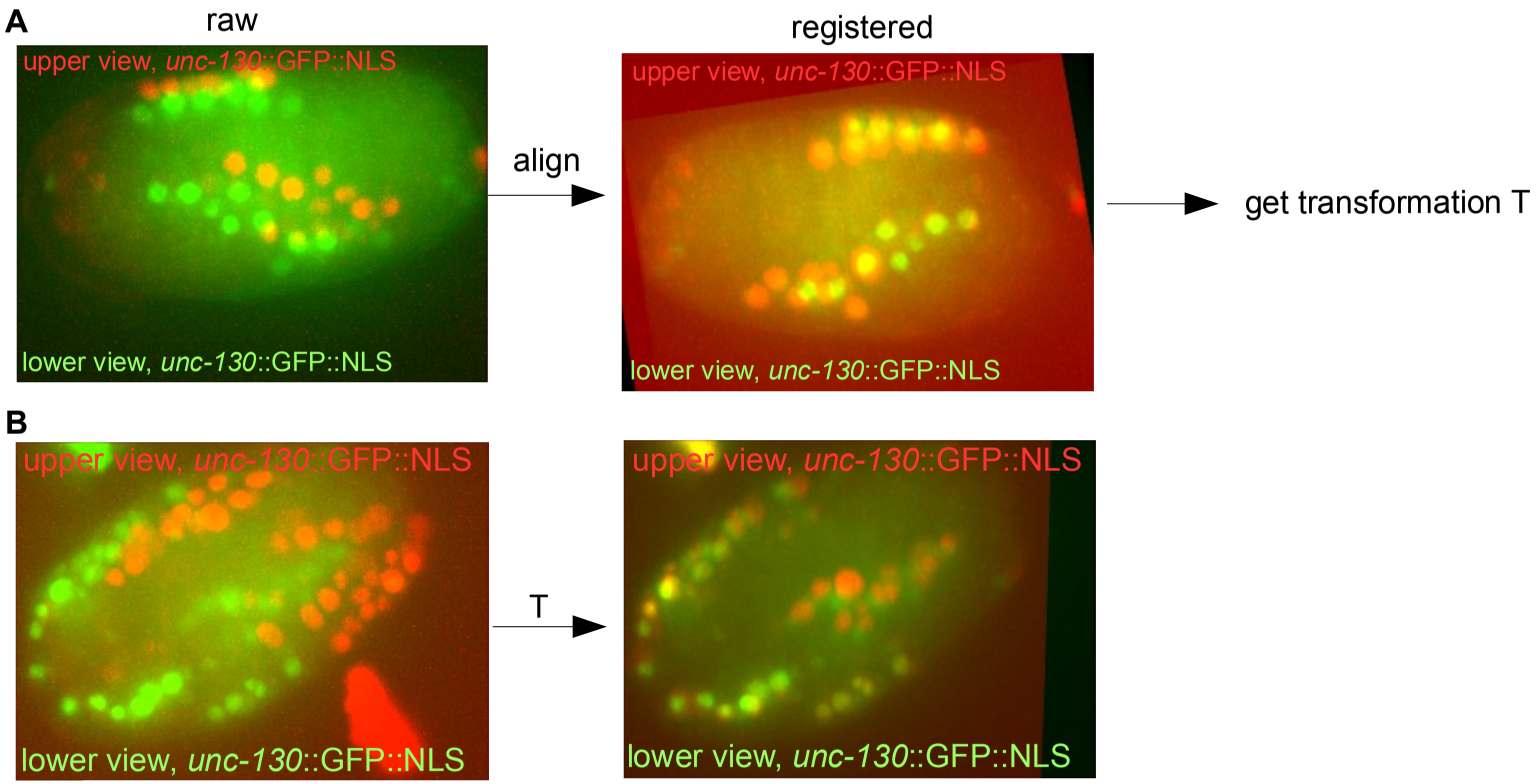
A
raw
upper view, unc-130::GFP::NLS
lower view, unc-130::GFP::NLS
align
registered
upper view, unc-130::GFP::NLS
lower view, unc-130::GFP::NLS
get transformation T
B
upper view, unc-130::GFP::NLS
lower view, unc-130::GFP::NLS
T
upper view, unc-130::GFP::NLS
lower view, unc-130::GFP::NLS

Initial results

While the system has not been completed, it is beginning to bear fruit with localized inductions in particular cells of interest (Figure A.4).

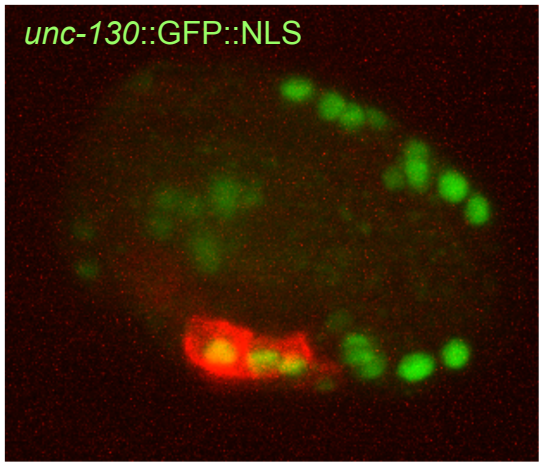

Figure A.4: Sample induction of mCherry expression by heat shock in *unc-130*-labeled cells

Individual nuclei in the RW11444 strain (see methods) are identified using the widefield imaging modality on the bottom light path which is described above, and targeted for induction. A successful localized heat induction is shown in A.4. More work will be required to calibrate and align the system to prevent wide off-target labeling which is observed in most cases.

Appendix B: SPIM troubleshooting guide

The basic methods by which the microscope is aligned for everyday experiments were described in the Chapter 2 under "Typical microscope operation." Here I outline solutions for problems which may arise occasionally.

If the laser is not flat, not centered, or the light sheet is not flat in the detection objective –this can be observed by a non-uniformity in illumination across the sample – then either adjust the angle of the piezo using the three screws at the back, or adjust the angle of the beam using the mirror conjugate to the sample. Often one has to do both; for example, if the beam is not roughly centered in the camera, the easiest way to center it is by angling the piezo. This will then change the angle of the beam as viewed by the detection objective, potentially keeping the light sheet from being flat under the camera; simply adjust the mirror on the table to match.

The top block of the microscope may come out of alignment with the bottom objective; this will essentially never be a problem for use with the 10x objective but could easily be an issue with the 40x. To move the top block as a whole, there are two thumbscrews situated on the pillar on which the objectives are mounted; after moving the microscope into a position in which the beam can be viewed in the bottom camera, use these two thumbscrews to push the top block until the beam is centered in the bottom camera. The top and bottom are now roughly aligned. (Exact alignment of top and bottom is essentially impossible with this system, because the thumbscrews are not

especially responsive (they push a lot of mass); and drift of the components would undo exact alignment even if a user somehow managed it.)

When securing the coverslip into the sample chamber, don't screw the screws down too tightly or the coverslip will crack. However, not screwing them down far enough will result in leakage of water out from under the O ring. It takes some practice to determine just how forceful to be. One other thing to note here is to always wipe dry the O ring as well as the position on the coverslip where it will sit before use, or a tight seal will not be made and water will slowly leak out over the course of an experiment (eventually preventing the microscope from functioning and finally killing the samples as they dry out).

The bounds of travel of the microscope stage may need to be reset; this may occur for example if the top block has been moved relative to the bottom, or as can sometimes occur when an ASI firmware problem results in the stage moving past its defined limits, or if the microscope objectives have been bumped and pushed into new positions. In order to fix this, first align the microscope so that the beam can be clearly viewed in the detection objective, using the Hamamatsu software. Then, open the program "ASI console"; attempt to travel to the maximum allowed distances in X or Y using the ASI controller (not moving too fast) while keeping an eye on the beam; the button next to the description of the X or Y position will light up in blue when the end of the allowable range is reached. Shift click the button. Then, continue moving the stage in this direction (very slowly, using the slow movement option on the controller) until you see the beam

moving in the camera. This will occur from pressure on either the detection objective or the excitation objective. At this point, backtrack in the direction from which you came; set the limit 250-300μm shy of the point at which movement of the beam was noticed, by clicking the limit button. Alternatively, in attempting to move the stage to its limit you may discover the beam shifting as you move, before reaching the limit that has been set in the ASI software; if that happens, backtrack 250-300μm from this position and fix the new limit there. Repeat for all four limits of the stage.

One common problem that can occur with the microscope is that the excitation objective or detection objective can be bumped significantly, for example, if a user lowers the top block (F axis) too much, pushing the objectives against a coverslip, or if the stage has traveled too far in X or Y. This will be observed by an inability to view the beam in the camera or by a shift in the position of the beam in the underside objective. Since the distance of the objectives out from the objective holders remains roughly fixed, while only the angle of the objectives is altered, this is quick to fix. The solution is to first observe in the underside objective whether the position of the excitation beam has moved away from its usual spot; if so, simply push the excitation objective with your finger to bring the beam back into roughly the correct angle. At this point you should be able to see the beam in the detection objective, but if not, you can use the three screws behind the piezo to angle the detection objective until the beam becomes visible. Adjust the screws behind the detection objective as well as the mirror on the table conjugate to the sample plane (which angles the incoming laser light) until the beam appears flat in the

camera. Alternatively, if the excitation objective appears not to have moved, then the detection objective must have (if the beam has shifted or is otherwise not visible); simply adjust the detection objective using the three screws until the beam comes into good focus.

If the position of the beam at its center position in the P axis is not roughly in the middle of the piezo range, which can happen if one or both objectives are bumped, then the position of the piezo can be adjusted by turning the three screws in synchrony to push the piezo as a whole along its axis. (Each of the three screws tips or tilts the piezo, leaving a redundant degree of freedom; the three together provide translation.)

When placing or removing the sample holder, always raise the F-axis to the top of its range of motion before proceeding. This will make it less likely that you brush the objectives with your hands (possibly necessitating realignment) as you manipulate the chamber. Nevertheless, be advised that brushing the objectives (from the side) will definitely happen eventually, necessitating realignment as described above. I always use bare hands for manipulating the sample chamber, because there is not much room to maneuver and finer control can be achieved without gloves. There is not much risk of brushing ones hands or fingers against the lenses because of the angle at which they sit, but nevertheless, avoid this.

The periscope is one of the weak points of the microscope; it is highly unstable using just the native Thorlabs components and an additional system for stabilizing it was never developed. The mirror mounts are so poorly attached to the post that simply

dusting the mirrors with a can of compressed air can be sufficient to alter mirror position, sufficient to require realignment. In other words, do not touch the periscope under normal circumstances. Under abnormal circumstances, those mirrors may need to be adjusted (in case of some large movement of or change to the microscope), but they are very difficult to control, hysteretic, and useless for fine adjustments; get the beam entering the microscope very roughly in the right position using the periscope mirrors, and then use the other controls available to refine it. Always use the fine controls on the periscope mirrors if you can (which are already rough), not the rough ones (which are too rough for almost any purpose).

Try to avoid cleaning the water dipping objectives if possible, since brushing the objectives with your hands will inevitably alter the alignment of the microscope. If you have to clean them, first try simply bathing them in ethanol and then water using the sample chamber and see if that solves the problem. Otherwise, very gently wipe the objectives with a "PEC-PAD" doused in ethanol. Try not to apply any pressure to the objectives from the side.

If you need to access the under-side optics, then the entire stage insert (surrounding the sample chamber) can be popped out simply by pulling up on it. To reinsert, line it up carefully on the grooves away from the spring, push down, and push it back up against the spring until you hear a click and the insert appears flat in the stage. This is not easy to do and will almost always take multiple tries, even once you get the

hang of it. If the insert does not appear flat, or has not clicked, then it has not been correctly inserted and will not be stable.

Several issues can cause the Labview program to crash, requiring it to be rebooted. The computer sometimes loses contact with one of the galvanometers, in what may be a driver issue; this is observed when the beam doesn't sweep in the correct direction, instead running at 45 degrees to the direction in which it ought to go. (The angle of the beam sweep can easily be seen by observing scatter off the top mirror of the periscope.) In all cases, restarting Labview resolves the issue.

Another problem can occur with the USB 3.0 card on the computer; if components which use the USB 3.0 ports (such as the AOTF) are shut off while the Labview program is still running, then the USB 3.0 port (which is used as a "pseudo-COM" port, and addressed by COM-n, e.g. COM-6, in Labview) may cease to be recognized. This can be solved by switching the plug to another USB 3.0 port, observing in Windows Device Manager which COM port number has just become active, and then setting the relevant COM port number in the Labview main module (under AOTF COM port, in the input block out of sight below and to the right of the main input block); or alternatively, this can be solved just by restarting the computer with the current connectivity.

The AOTF may sometimes refuse to receive commands from the computer. I think this only happens if serial commands are written too quickly to the device, which should never happen under normal operation. Nevertheless, if it does happen, this

problem is usually resolved by rebooting the AOTF, and / or the computer, but if that doesn't work, then the AOTF remote control should be connected and the AOTF operated once using the control. For example, just press 1 to flip the 488 laser on or off. Then the AOTF will again take input from the computer. If you have unplugged the USB cable from the computer in order to connect the remote control, make sure you replug it into the same port or you will have to adjust which COM port is used for the AOTF in Labview as described above.

The Labview Main Module program will show an error at start up if it cannot contact the AOTF or the ASI controller. However, it does not check for camera access. Before starting an imaging session it's a good idea to verify that the computer is in contact with the camera by opening the Hamamatsu Live software. If the camera is recognized its name should appear in the upper left of the screen and live imaging should be permitted. On the other hand, always be sure to close Hamamatsu Live before actually running the main scan program, since inability to communicate with the Hamamatsu camera will cause a crash.

There are occasional memory errors that can occur in using the Labview program, particularly when switching between numbers of colors in experiments (i.e., red and green imaging to just green imaging); these errors will manifest as a warning popup describing "attempt to access a deleted reference." This will require rebooting the Labview software and possibly turning the camera on and off again.

When the camera is not recognized by the computer, which has occasionally occurred for unclear reasons, flipping the camera on and off may not solve the problem. Try rebooting the computer. Occasionally even this doesn't work, but some combination of turning camera on and off and rebooting eventually has always gotten the camera recognized. Maybe this is not so much a problem now as it was with earlier versions of the camera drivers.

The following components should be turned off at the end of each imaging session: the camera, the lasers, the ASI controller, and the AOTF. Failure to do this may shorten their lifespans. I usually leave the galvanometer controller running, but perhaps it's better to turn this off as well.

The entire microscope body may occasionally need to be taken apart; the last time this occurred was when the piezo failed and had to be replaced in August 2014. This is not as terrible as it sounds, but there are many screws that need to be removed / replaced and some care is required. A set of **6** screws holds the two halves of the top block to the pillar; remove these while keeping a firm grip on the bottom of the top block because it will of course fall suddenly when the last screw is extracted. An additional pair of screws holds the two halves of the top block together. To remove the piezo from its holder, there is a set of 4 screws on springs that should be removed. The detection objective is currently situated at one end of its range (screwed up next to the piezo) so there is no concern here about finding the correct position when reattaching it. The excitation objective should not need to be moved; just be especially gentle when handling that half.

When placing the microscope body up against the pillar, the back must be quite flat relative to the table / main body of the microscope, or one objective will hit the coverslip when the top block / F-axis is lowered before the correct position for focusing on the coverslip is reached. You have to angle the top block hard counterclockwise (push hard) while quickly screwing it down in order to get it flat, since it naturally is misaligned / wants to bend the wrong way. This could take multiple tries to get right. It will be clear that the top block is not flat if the beam appears to shift suddenly in the camera on lowering the F-axis, before getting to point when the beam waist crosses the coverslip.

The stage can also be taken apart; I have had to do this before, for instance to access the tube lens on the bottom imaging axis and to swap in a turret for the underside light path. The various connectors attaching the stage to the controller will need to be removed before the stage can be taken apart, and then reattached in the right places; if memory serves the X and Y connectors have the same number of pins and can accidentally be swapped, which will cause the stage axes to be switched. Simply note which one goes where before removing / reattaching.

While this may seem like a long list, I have tried to cover the full range of issues that can occur on a regular or even quite irregular basis, for which a solution can easily be described in advance. Obviously, an answer to every question cannot be provided; although the components on the table are stable (except, as noted above, the periscope), even stable components could conceivably be damaged by an inexperienced user, or might need to be adjusted if large changes are made in other parts of the microscope.

In general, the key to these alignments is to move as few parts as possible, slowly. When using the microscope be gentle, and careful, especially around the objectives. Regular alignments of the piezo and the mirror conjugate to the sample plane will be required because of the instability of the microscope objectives; the rest of the components should never need to be adjusted except under unforeseen circumstances, or if modifications are made to the system.

Bibliography

Abbe (1882). The Relation of Aperture and Power in the Microscope (continued).*. Journal of the Royal Microscopical Society *2*, 460–473.

Abraham, M.C., Lu, Y., and Shaham, S. (2007). A Morphologically Conserved Nonapoptotic Program Promotes Linker Cell Death in Caenorhabditis elegans. Developmental Cell *12*, 73–86.

Ahrens, M.B., Orger, M.B., Robson, D.N., Li, J.M., and Keller, P.J. (2013). Whole-brain functional imaging at cellular resolution using light-sheet microscopy. Nat Meth *10*, 413–420.

Alda, J. Laser and Gaussian Beam Propagation and Transformation.

Axelrod, D. (2013). Evanescent Excitation and Emission in Fluorescence Microscopy. Biophys J *104*, 1401–1409.

Bao, Z., Murray, J.I., Boyle, T., Ooi, S.L., Sandel, M.J., and Waterston, R.H. (2006). Automated cell lineage tracing in Caenorhabditis elegans. PNAS *103*, 2707–2712.

Bao, Z., Zhao, Z., Boyle, T.J., Murray, J.I., and Waterston, R.H. (2008). Control of Cell Cycle Timing during C. elegans Embryogenesis. Dev Biol *318*, 65–72.

Besl, P.J., and McKay, H.D. (1992). A method for registration of 3-D shapes. IEEE Transactions on Pattern Analysis and Machine Intelligence *14*, 239–256.

Betzig, E., Patterson, G.H., Sougrat, R., Lindwasser, O.W., Olenych, S., Bonifacino, J.S., Davidson, M.W., Lippincott-Schwartz, J., and Hess, H.F. (2006). Imaging intracellular fluorescent proteins at nanometer resolution. Science *313*, 1642–1645.

Bookstein, F.L. (1989). Principal warps: thin-plate splines and the decomposition of deformations. IEEE Transactions on Pattern Analysis and Machine Intelligence *11*, 567–585.

Born, M., Wolf, E., Bhatia, A.B., Gabor, D., Stokes, A.R., Taylor, A.M., Wayman, P.A., and Wilcock, W.L. (1999). Principles of Optics: Electromagnetic Theory of Propagation, Interference and Diffraction of Light (Cambridge: Cambridge University Press).

Brenner, S. (1974). The genetics of Caenorhabditis elegans. Genetics *77*, 71–94.

Brown, L.G. (1992). A Survey of Image Registration Techniques. ACM Comput. Surv. *24*, 325–376.

Broxton, M., Grosenick, L., Yang, S., Cohen, N., Andalman, A., Deisseroth, K., and Levoy, M. (2013). Wave optics theory and 3-D deconvolution for the light field microscope. Opt. Express, OE *21*, 25418–25439.

Buchin, M.P. (2011). ICCD, EMCCD, and sCMOS compete in low-light imaging. Laser Focus World, viewed 2 June 2016, <http://www.laserfocusworld.com/articles/print/volume-47/issue-7/features/low-light-imaging-iccd-emccd-and-scmos-compete-in-low-light-imaging.html>.

Burden, R., and Faires, J. (2004). Numerical Analysis (Belmont: Brooks/Cole).

Chalfie, M., Tu, Y., Euskirchen, G., Ward, W.W., and Prasher, D.C. (1994). Green fluorescent protein as a marker for gene expression. Science *263*, 802–805.

Chen, B.-C., Legant, W.R., Wang, K., Shao, L., Milkie, D.E., Davidson, M.W., Janetopoulos, C., Wu, X.S., Hammer, J.A., Liu, Z., et al. (2014). Lattice Light Sheet Microscopy: Imaging Molecules to Embryos at High Spatiotemporal Resolution. Science *346*, 1257998.

Chen, T., Catrysse, P.B., El Gamal, A., and Wandell, B.A. (2000). How small should pixel size be? pp. 451–459.

Chiorazzi, M., Rui, L., Yang, Y., Ceribelli, M., Tishbi, N., Maurer, C.W., Ranuncolo, S.M., Zhao, H., Xu, W., Chan, W.-C.C., et al. (2013). Related F-box proteins control cell death in Caenorhabditis elegans and human lymphoma. Proc. Natl. Acad. Sci. U.S.A. *110*, 3943–3948.

Christensen, R.P., Bokinsky, A., Santella, A., Wu, Y., Marquina-Solis, J., Guo, M., Kovacevic, I., Kumar, A., Winter, P.W., Tashakkori, N., et al. (2015). Untwisting the Caenorhabditis elegans embryo. Elife *4*.

Chui, H., and Rangarajan, A. (2000). A feature registration framework using mixture models. In IEEE Workshop on Mathematical Methods in Biomedical Image Analysis, 2000. Proceedings, pp. 190–197.

Conradt, B., and Horvitz, H.R. (1998). The C. elegans protein EGL-1 is required for programmed cell death and interacts with the Bcl-2-like protein CED-9. Cell *93*, 519–529.

Davidovits, P. (1969). Scanning Laser Microscope. Nature *223*, 831.

Davidovits, P., and Egger, M.D. (1971). Scanning laser microscope for biological investigations. Appl Opt *10*, 1615–1619.

Deppe, U., Schierenberg, E., Cole, T., Krieg, C., Schmitt, D., Yoder, B., and von Ehrenstein, G. (1978). Cell lineages of the embryo of the nematode Caenorhabditis elegans. Proc Natl Acad Sci U S A *75*, 376–380.

Durnin, J. (1987). Exact solutions for nondiffracting beams. I. The scalar theory. J. Opt. Soc. Am. A, JOSAA *4*, 651–654.

Durnin, J., Miceli, J.J., and Eberly, J.H. (1987). Diffraction-free beams. Phys. Rev. Lett. *58*, 1499–1501.

Edelstein, A.D., Tsuchida, M.A., Amodaj, N., Pinkard, H., Vale, R.D., and Stuurman, N. (2014). Advanced methods of microscope control using μManager software. J Biol Methods *1*.

Edgar, L.G., and Goldstein, B. (2012). Culture and Manipulation of Embryonic Cells. Methods Cell Biol. *107*, 151–175.

Ellis, R.E., Jacobson, D.M., and Horvitz, H.R. (1991). Genes required for the engulfment of cell corpses during programmed cell death in Caenorhabditis elegans. Genetics *129*, 79–94.

Forrester, W.C., Dell, M., Perens, E., and Garriga, G. (1999). A C. elegans Ror receptor tyrosine kinase regulates cell motility and asymmetric cell division. Nature *400*, 881–885.

Fossum, E.R. (1997). CMOS image sensors: electronic camera-on-a-chip. IEEE Transactions on Electron Devices *44*, 1689–1698.

Fry, A.L., Laboy, J.T., and Norman, K.R. (2014). VAV-1 acts in a single interneuron to inhibit motor circuit activity in Caenorhabditis elegans. Nat Commun *5*, 5579.

Gao, L., Shao, L., Higgins, C.D., Poulton, J.S., Peifer, M., Davidson, M.W., Wu, X., Goldstein, B., and Betzig, E. (2012). Noninvasive imaging beyond the diffraction limit of 3D dynamics in thickly fluorescent specimens. Cell *151*, 1370–1385.

Giurumescu, C.A., Kang, S., Planchon, T.A., Betzig, E., Bloomekatz, J., Yelon, D., Cosman, P., and Chisholm, A.D. (2012). Quantitative semi-automated analysis of morphogenesis with single-cell resolution in complex embryos. Development *139*, 4271–4279.

Gold, S., Rangarajan, A., Lu, C., and Mjolsness, E. (1997). New Algorithms for 2D and 3D Point Matching: Pose Estimation and Correspondence. Pattern Recognition *31*, 957–964.

Gönczy, P., and Rose, L.S. (2005). Asymmetric cell division and axis formation in the embryo. WormBook 1–20.

Goodman, J.W. (2005). Introduction to Fourier Optics (Englewood, Colo: Roberts & Co).

Gramkow, C. (2001). On Averaging Rotations. Int. J. Comput. Vision *42*, 7–16.

Gregor, T., Wieschaus, E.F., McGregor, A.P., Bialek, W., and Tank, D.W. (2007). Stability and nuclear dynamics of the bicoid morphogen gradient. Cell *130*, 141–152.

Gustafsson, M.G. (1999). Extended resolution fluorescence microscopy. Curr. Opin. Struct. Biol. *9*, 627–634.

Gustafsson, M.G. (2000). Surpassing the lateral resolution limit by a factor of two using structured illumination microscopy. J. Microsc. *198*, 82–87.

Gustafsson, M.G.L. (2005). Nonlinear structured-illumination microscopy: Wide-field fluorescence imaging with theoretically unlimited resolution. PNAS *102*, 13081–13086.

Gustafsson, M.G., Agard, D.A., and Sedat, J.W. (1999). I5M: 3D widefield light microscopy with better than 100 nm axial resolution. J Microsc *195*, 10–16.

Hamahashi, S., Onami, S., and Kitano, H. (2005). Detection of nuclei in 4D Nomarski DIC microscope images of early Caenorhabditis elegans embryos using local image entropy and object tracking. BMC Bioinformatics *6*, 125.

Harfe, B.D., and Fire, A. (1998). Muscle and nerve-specific regulation of a novel NK-2 class homeodomain factor in Caenorhabditis elegans. Development *125*, 421–429.

Harterink, M., Kim, D. hyun, Middelkoop, T.C., Doan, T.D., Oudenaarden, A. van, and Korswagen, H.C. (2011). Neuroblast migration along the anteroposterior axis of C. elegans is controlled by opposing gradients of Wnts and a secreted Frizzled-related protein. Development *138*, 2915–2924.

Hecht, E. (2016). Optics (Boston: Pearson).

Heiman, M.G., and Shaham, S. (2009). DEX-1 and DYF-7 Establish Sensory Dendrite Length by Anchoring Dendritic Tips during Cell Migration. Cell *137*, 344–355.

Hell, S., and Stelzer, E.H.K. (1992). Properties of a 4Pi confocal fluorescence microscope. J. Opt. Soc. Am. A, JOSAA *9*, 2159–2166.

Hell, S.W., and Wichmann, J. (1994). Breaking the diffraction resolution limit by stimulated emission: stimulated-emission-depletion fluorescence microscopy. Opt. Lett., OL *19*, 780–782.

Hell, S.W., Lindek, S., Cremer, C., and Stelzer, E.H.K. (1994). Confocal microscopy with an increased detection aperture: type-B 4Pi confocal microscopy. Optics Letters *19*, 222.

Hill, A.J., Mansfield, R., Lopez, J.M.N.G., Raizen, D.M., and Van Buskirk, C. (2014). Cellular stress induces a protective sleep-like state in C. elegans. Curr. Biol. *24*, 2399–2405.

Hird, S.N., and White, J.G. (1993). Cortical and cytoplasmic flow polarity in early embryonic cells of Caenorhabditis elegans. J. Cell Biol. *121*, 1343–1355.

Ho, T.K. (1995). Random decision forests. In , Proceedings of the Third International Conference on Document Analysis and Recognition, 1995, pp. 278–282 vol.1.

Hoebe, R.A., Van Oven, C.H., Gadella, T.W.J., Dhonukshe, P.B., Van Noorden, C.J.F., and Manders, E.M.M. (2007). Controlled light-exposure microscopy reduces photobleaching and phototoxicity in fluorescence live-cell imaging. Nat Biotech *25*, 249–253.

Horn, B.K.P. (1987). Closed-form solution of absolute orientation using unit quaternions. J. Opt. Soc. Am. A, JOSAA *4*, 629–642.

Horvitz, H.R. (1999). Genetic control of programmed cell death in the nematode Caenorhabditis elegans. Cancer Res. *59*, 1701s–1706s.

Huisken, J., and Stainier, D.Y.R. (2009). Selective plane illumination microscopy techniques in developmental biology. Development *136*, 1963–1975.

Huisken, J., Swoger, J., Bene, F.D., Wittbrodt, J., and Stelzer, E.H.K. (2004). Optical Sectioning Deep Inside Live Embryos by Selective Plane Illumination Microscopy. Science *305*, 1007–1009.

Jin, Y. (2005). Synaptogenesis. WormBook.

Juskaitis, R., R., Wilson, T., Neil, M. a. A., and Kozubek, M. (1996). Efficient real-time confocal microscopy with white light sources. Nature *383*, 804–806.

Kamei, Y., Suzuki, M., Watanabe, K., Fujimori, K., Kawasaki, T., Deguchi, T., Yoneda, Y., Todo, T., Takagi, S., Funatsu, T., et al. (2009). Infrared laser–mediated gene induction in targeted single cells in vivo. Nat Meth *6*, 79–81.

Keller, P.J., Schmidt, A.D., Wittbrodt, J., and Stelzer, E.H.K. (2008). Reconstruction of zebrafish early embryonic development by scanned light sheet microscopy. Science *322*, 1065–1069.

Keller, P.J., Schmidt, A.D., Santella, A., Khairy, K., Bao, Z., Wittbrodt, J., and Stelzer, E.H.K. (2010). Fast, high-contrast imaging of animal development with scanned light sheet–based structured-illumination microscopy. Nature Methods *7*, 637–642.

Kennerdell, J.R. (2008). Genetic and cellular analysis of nerve ring defects in C. elegans. University of California, San Francisco.

Kennerdell, J.R., Fetter, R.D., and Bargmann, C.I. (2009). Wnt-Ror signaling to SIA and SIB neurons directs anterior axon guidance and nerve ring placement in C. elegans. Development *136*, 3801–3810.

Kinchen, J.M., Cabello, J., Klingele, D., Wong, K., Feichtinger, R., Schnabel, H., Schnabel, R., and Hengartner, M.O. (2005). Two pathways converge at CED-10 to mediate actin rearrangement and corpse removal in *C. elegans*. Nature *434*, 93–99.

Kinet, M.J., Malin, J.A., Abraham, M.C., Blum, E.S., Silverman, M.R., Lu, Y., and Shaham, S. (2016). HSF-1 activates the ubiquitin proteasome system to promote non-apoptotic developmental cell death in *C. elegans*. Elife *5*.

Klar, T.A., Jakobs, S., Dyba, M., Egner, A., and Hell, S.W. (2000). Fluorescence microscopy with diffraction resolution barrier broken by stimulated emission. PNAS *97*, 8206–8210.

Lavagnino, Z., Cella Zanacchi, F., Ronzitti, E., and Diaspro, A. (2013). Two-photon excitation selective plane illumination microscopy (2PE-SPIM) of highly scattering samples: characterization and application. Optics Express *21*, 5998.

Leonhardt, U. (2009). Perfect imaging without negative refraction. New J. Phys. *11*, 93040.

Levoy, M., Ng, R., Adams, A., Footer, M., and Horowitz, M. (2006). Light Field Microscopy. In ACM SIGGRAPH 2006 Papers, (New York, NY, USA: ACM), pp. 924–934.

Lindek, S., and Stelzer, E.H. (1994). Confocal theta microscopy and 4Pi-confocal theta microscopy. pp. 188–194.

Luo, B., and Hancock, E.R. (2003). A unified framework for alignment and correspondence. Comput. Vis. Image Underst. *92*, 26–55.

Maurer, C.W., Chiorazzi, M., and Shaham, S. (2007). Timing of the onset of a developmental cell death is controlled by transcriptional induction of the *C. elegans* ced-3 caspase-encoding gene. Development *134*, 1357–1368.

Minsky, M. (1961). Microscopy apparatus.

Minsky, M. (1988). Memoir on inventing the confocal scanning microscope. Scanning *10*, 128–138.

Mohler, W.A., Shemer, G., del Campo, J.J., Valansi, C., Opoku-Serebuoh, E., Scranton, V., Assaf, N., White, J.G., and Podbilewicz, B. (2002). The type I membrane protein EFF-1 is essential for developmental cell fusion. Dev. Cell *2*, 355–362.

Murphy, D.B. (2001). Fundamentals of Light Microscopy and Electronic Imaging (New York: Wiley-Liss).

Murray, J.I., Bao, Z., Boyle, T.J., and Waterston, R.H. (2006). The lineaging of fluorescently-labeled Caenorhabditis elegans embryos with StarryNite and AceTree. Nat Protoc *1*, 1468–1476.

Myronenko, A., and Song, X. (2010). Point Set Registration: Coherent Point Drift. IEEE Transactions on Pattern Analysis and Machine Intelligence *32*, 2262–2275.

Myung, I.J. (2003). Tutorial on maximum likelihood estimation. Journal of Mathematical Psychology *47*, 90–100.

Neumann, B., Coakley, S., Giordano-Santini, R., Linton, C., Lee, E.S., Nakagawa, A., Xue, D., and Hilliard, M.A. (2015). EFF-1-mediated regenerative axonal fusion requires components of the apoptotic pathway. Nature *517*, 219–222.

Oikonomou, G., and Shaham, S. (2011). The glia of Caenorhabditis elegans. Glia *59*, 1253–1263.

Oliveira, F.P.M., and Tavares, J.M.R.S. (2014). Medical image registration: a review. Comput Methods Biomech Biomed Engin *17*, 73–93.

Ooi, S.L., Priess, J.R., and Henikoff, S. (2006). Histone H3.3 variant dynamics in the germline of Caenorhabditis elegans. PLoS Genet. *2*, e97.

Oren-Suissa, M., Hall, D.H., Treinin, M., Shemer, G., and Podbilewicz, B. (2010). The fusogen EFF-1 controls sculpting of mechanosensory dendrites. Science *328*, 1285–1288.

Owraghi, M., Broitman-Maduro, G., Luu, T., Roberson, H., and Maduro, M.F. (2010). Roles of the Wnt effector POP-1/TCF in the C. elegans endomesoderm specification gene network. Dev Biol *340*, 209–221.

Pan, C.-L., Howell, J.E., Clark, S.G., Hilliard, M., Cordes, S., Bargmann, C.I., and Garriga, G. (2006). Multiple Wnts and frizzled receptors regulate anteriorly directed cell and growth cone migrations in Caenorhabditis elegans. Dev. Cell *10*, 367–377.

Peng, H., Chung, P., Long, F., Qu, L., Jenett, A., Seeds, A.M., Myers, E.W., and Simpson, J.H. (2011). BrainAligner: 3D registration atlases of Drosophila brains. Nat Meth *8*, 493–498.

Podbilewicz, B., Leikina, E., Sapir, A., Valansi, C., Suissa, M., Shemer, G., and Chernomordik, L.V. (2006). The C. elegans developmental fusogen EFF-1 mediates homotypic fusion in heterologous cells and in vivo. Dev. Cell *11*, 471–481.

Prevedel, R., Yoon, Y.-G., Hoffmann, M., Pak, N., Wetzstein, G., Kato, S., Schrödel, T., Raskar, R., Zimmer, M., Boyden, E.S., et al. (2014). Simultaneous whole-animal 3D imaging of neuronal activity using light-field microscopy. Nat Meth *11*, 727–730.

Pujol, N., Torregrossa, P., Ewbank, J.J., and Brunet, J.F. (2000). The homeodomain protein CePHOX2/CEH-17 controls antero-posterior axonal growth in C. elegans. Development *127*, 3361–3371.

Rego, E.H., Shao, L., Macklin, J.J., Winoto, L., Johansson, G.A., Kamps-Hughes, N., Davidson, M.W., and Gustafsson, M.G.L. (2012). Nonlinear structured-illumination microscopy with a photoswitchable protein reveals cellular structures at 50-nm resolution. PNAS *109*, E135–E143.

Richards, J.L., Zacharias, A.L., Walton, T., Burdick, J.T., and Murray, J.I. (2013). A quantitative model of normal Caenorhabditis elegans embryogenesis and its disruption after stress. Dev. Biol. *374*, 12–23.

Richardson, W.H. (1972). Bayesian-Based Iterative Method of Image Restoration*. J. Opt. Soc. Am., JOSA *62*, 55–59.

Rust, M.J., Bates, M., and Zhuang, X. (2006). Sub-diffraction-limit imaging by stochastic optical reconstruction microscopy (STORM). Nat Meth *3*, 793–796.

Santella, A., Du, Z., Nowotschin, S., Hadjantonakis, A.-K., and Bao, Z. (2010). A hybrid blob-slice model for accurate and efficient detection of fluorescence labeled nuclei in 3D. BMC Bioinformatics *11*, 1–13.

Santella, A., Catena, R., Kovacevic, I., Shah, P., Yu, Z., Marquina-Solis, J., Kumar, A., Wu, Y., Schaff, J., Colón-Ramos, D., et al. (2015). WormGUIDES: an interactive single cell developmental atlas and tool for collaborative multidimensional data exploration. BMC Bioinformatics *16*, 1–9.

Schindelin, J., Arganda-Carreras, I., Frise, E., Kaynig, V., Longair, M., Pietzsch, T., Preibisch, S., Rueden, C., Saalfeld, S., Schmid, B., et al. (2012). Fiji: an open-source platform for biological-image analysis. Nat Meth *9*, 676–682.

Schnabel, R., Hutter, H., Moerman, D., and Schnabel, H. (1997). Assessing normal embryogenesis in Caenorhabditis elegans using a 4D microscope: variability of development and regional specification. Dev. Biol. *184*, 234–265.

Schnabel, R., Bischoff, M., Hintze, A., Schulz, A.-K., Hejnol, A., Meinhardt, H., and Hutter, H. (2006). Global cell sorting in the C. elegans embryo defines a new mechanism for pattern formation. Dev. Biol. *294*, 418–431.

Schwarz, E.M., Kato, M., and Sternberg, P.W. (2012). Functional transcriptomics of a migrating cell in Caenorhabditis elegans. PNAS *109*, 16246–16251.

Shao, L., Kner, P., Rego, E.H., and Gustafsson, M.G.L. (2011). Super-resolution 3D microscopy of live whole cells using structured illumination. Nat Meth *8*, 1044–1046.

Siedentopf, H., and Zsigmondy, R. (1902). Uber Sichtbarmachung und Größenbestimmung ultramikoskopischer Teilchen, mit besonderer Anwendung auf Goldrubingläser. Ann. Phys. *315*, 1–39.

Silvestri, L., Bria, A., Sacconi, L., Iannello, G., and Pavone, F.S. (2012). Confocal light sheet microscopy: micron-scale neuroanatomy of the entire mouse brain. Opt. Express, OE *20*, 20582–20598.

Sommer, C., Straehle, C., Köthe, U., and Hamprecht, F.A. (2011). Ilastik: Interactive learning and segmentation toolkit. In 2011 IEEE International Symposium on Biomedical Imaging: From Nano to Macro, pp. 230–233.

Stein, K.K., and Golden, A. (2015). The *C. elegans* eggshell. WormBook 1–35.

Sulston, J.E., and Horvitz, H.R. (1977). Post-embryonic cell lineages of the nematode, Caenorhabditis elegans. Dev. Biol. *56*, 110–156.

Sulston, J.E., Schierenberg, E., White, J.G., and Thomson, J.N. (1983). The embryonic cell lineage of the nematode Caenorhabditis elegans. Dev. Biol. *100*, 64–119.

Swedlow, J.R., and Platani, M. (2002). Live cell imaging using wide-field microscopy and deconvolution. Cell Struct. Funct. *27*, 335–341.

Thomas, C., DeVries, P., Hardin, J., and White, J. (1996). Four-Dimensional Imaging: Computer Visualization of 3D Movements in Living Specimens. Science *273*, 603–607.

Thompson, R.E., Larson, D.R., and Webb, W.W. (2002). Precise nanometer localization analysis for individual fluorescent probes. Biophys J *82*, 2775–2783.

Tinevez, J.-Y., Dragavon, J., Baba-Aissa, L., Roux, P., Perret, E., Canivet, A., Galy, V., and Shorte, S. (2012). A quantitative method for measuring phototoxicity of a live cell imaging microscope. Meth. Enzymol. *506*, 291–309.

Tomer, R., Khairy, K., Amat, F., and Keller, P.J. (2012). Quantitative high-speed imaging of entire developing embryos with simultaneous multiview light-sheet microscopy. Nature Methods *9*, 755–763.

Toomre, D., and Pawley, J.B. (2006). Disk-Scanning Confocal Microscopy. In Handbook Of Biological Confocal Microscopy, J.B. Pawley, ed. (Springer US), pp. 221–238.

Van Aelst, S., and Rousseeuw, P. (2009). Minimum volume ellipsoid. WIREs Comp Stat *1*, 71–82.

Wang, R. (2014). Sharpening and edge detection, viewed 2 June 2016, <http://fourier.eng.hmc.edu/e161/lectures/gradient/gradient.html>.

Webb, D.J., and Brown, C.M. (2013). Epi-fluorescence microscopy. Methods Mol. Biol. *931*, 29–59.

Weisstein, E.W. (n.d.). Convex Hull. MathWorld, viewed 2 June 2016, <http://mathworld.wolfram.com/ConvexHull.html>.

Weisstein, E.W. (n.d.). Affine Transformation. MathWorld, viewed 2 June 2016. <http://mathworld.wolfram.com/AffineTransformation.html>.

White, J.G., Southgate, E., Thomson, J.N., and Brenner, S. (1986). The Structure of the Nervous System of the Nematode Caenorhabditis elegans. Philosophical Transactions of

the Royal Society of London B: Biological Sciences *314*, 1–340.

Wu, Y.C., and Horvitz, H.R. (1998). C. elegans phagocytosis and cell-migration protein CED-5 is similar to human DOCK180. Nature *392*, 501–504.

Wu, Y., Ghitani, A., Christensen, R., Santella, A., Du, Z., Rondeau, G., Bao, Z., Colón-Ramos, D., and Shroff, H. (2011). Inverted selective plane illumination microscopy (iSPIM) enables coupled cell identity lineaging and neurodevelopmental imaging in Caenorhabditis elegans. PNAS *108*, 17708–17713.

Wu, Y., Wawrzusin, P., Senseney, J., Fischer, R.S., Christensen, R., Santella, A., York, A.G., Winter, P.W., Waterman, C.M., Bao, Z., et al. (2013). Spatially isotropic four-dimensional imaging with dual-view plane illumination microscopy. Nat Biotechnol *31*, 1032–1038.

York, A.G., Chandris, P., Nogare, D.D., Head, J., Wawrzusin, P., Fischer, R.S., Chitnis, A., and Shroff, H. (2013). Instant super-resolution imaging in live cells and embryos via analog image processing. Nat Meth *10*, 1122–1126.

Yoshimura, S., Murray, J.I., Lu, Y., Waterston, R.H., and Shaham, S. (2008). mls-2 and vab-3 Control glia development, hlh-17/Olig expression and glia-dependent neurite extension in C. elegans. Development *135*, 2263–2275.

Yuzyuk, T., Fakhouri, T.H.I., Kiefer, J., and Mango, S.E. (2009). The polycomb complex protein mes-2/E(z) promotes the transition from developmental plasticity to differentiation in C. elegans embryos. Dev. Cell *16*, 699–710.

Zallen, J.A., Kirch, S.A., and Bargmann, C.I. (1999). Genes required for axon pathfinding and extension in the C. elegans nerve ring. Development *126*, 3679–3692.

Zhang, X., and Liu, Z. (2008). Superlenses to overcome the diffraction limit. Nat Mater *7*, 435–441.

Zitová, B., and Flusser, J. (2003). Image registration methods: a survey. Image and Vision Computing *21*, 977–1000.